Observations of large-scale solar flows

Dissertation

zur Erlangung des mathematisch-naturwissenschaftlichen Doktorgrades

"Doctor rerum naturalium"

der Georg-August-Universität Göttingen

im Promotionsstudiengang Physik

der Georg-August University School of Science (GAUSS)

vorgelegt von

Bastian Proxauf

aus Freistadt, Österreich

Göttingen, 2020

Betreuungsausschuss

Prof. Dr. Laurent Gizon
Max-Planck-Institut für Sonnensystemforschung und
Institut für Astrophysik, Georg-August-Universität Göttingen, Göttingen, Deutschland

Prof. Dr. Andreas Tilgner
Institut für Geophysik, Georg-August-Universität Göttingen, Göttingen, Deutschland

Dr. Björn Löptien
Max-Planck-Institut für Sonnensystemforschung, Göttingen, Deutschland

Mitglieder der Prüfungskommision

Referent: Prof. Dr. Laurent Gizon
Max-Planck-Institut für Sonnensystemforschung und
Institut für Astrophysik, Georg-August-Universität Göttingen, Göttingen, Deutschland

Korreferent: Prof. Dr. Andreas Tilgner
Institut für Geophysik, Georg-August-Universität Göttingen, Göttingen, Deutschland

Weitere Mitglieder der Prüfungskommission:

Prof. Dr. Ulrich Christensen
Max-Planck-Institut für Sonnensystemforschung, Göttingen, Deutschland

Prof. Dr. Stefan Dreizler
Institut für Astrophysik, Georg-August-Universität Göttingen, Göttingen, Deutschland

Prof. Dr. Wolfram Kollatschny
Institut für Astrophysik, Georg-August-Universität Göttingen, Göttingen, Deutschland

PD Dr. Olga Shishkina
Max-Planck-Institut für Dynamik und Selbstorganisation, Göttingen, Deutschland

Tag der mündlichen Prüfung: 10.06.2020

Printed in Germany

Cover figure: Large-scale flows on the solar surface as derived by tracking the motion of small convection cells (granules) on observations from the Helioseismic and Magnetic Imager instrument aboard the Solar Dynamics Observatory spacecraft. The flows have been averaged over roughly 27 days (one solar rotation). The flow velocities are given by the arrows and are shown as a function of latitude (covering ±65°) and longitude (covering 360°). Additionally, the flow vorticity (a measure for local twists in the velocity field) is shown by the color image, with blue and red indicating a clockwise/counter-clockwise flow curvature.

Contents

List of Figures

List of Tables

Summary

The aim of this thesis is to observationally characterize various large-scale solar flows, including the recently detected solar Rossby waves (waves of radial vorticity), large-scale convection, and flows around active regions. These large-scale flows likely interact with the solar differential rotation and, through a dynamo process, with the solar magnetic field.

To study these flows I use several years of observations from the Helioseismic and Magnetic Imager (HMI) aboard the Solar Dynamics Observatory (SDO). These data are processed using two complementary techniques to obtain horizontal flows on the solar surface and in the solar interior: local correlation tracking, which is limited to the solar surface, and ring-diagram analysis, which is able to probe the near-surface layers in the solar interior (the observational depth limit is roughly 16 Mm) at a lower temporal and spatial resolution.

First, I study the latitudinal and radial dependence of solar equatorial Rossby waves. For this, the radial vorticity is computed from the horizontal flows and a spectral analysis is applied via a spherical harmonics transform in latitude and longitude and a Fourier transform in time. In the top 9 Mm below the surface, the radial dependence of the vorticity eigenfunctions is consistent with a variation of the form r^{m-1}, expected from models, where r is the radial coordinate and m is the longitudinal wavenumber. However, systematic errors in the ring-diagram analysis prevent me from constraining the radial eigenfunctions deeper in the solar interior. The latitudinal dependence of the mode eigenfunctions is determined via a correlation analysis between the equator and other latitudes, and via a singular value decomposition. The real part of the eigenfunctions decreases away from the equator and switches sign at absolute latitudes between 20 and 30°, in agreement with previous results. The imaginary part of the eigenfunctions has a small, but nonzero, amplitude at all latitudes, which may be indicative of attenuation.

Second, using the horizontal flow maps, I study the energy spectrum of large-scale convection in the context of existing results inferred by time-distance helioseismology and simulations. These results had revealed a huge discrepancy for the velocity of large-scale convection in the solar interior (root-mean-square values of roughly 1 and 100 m s^{-1}, respectively). This disagreement, the convective conundrum, is crucial with regard to current models of solar convection. Several issues are found in the existing analysis, such as different conventions for spherical harmonics transforms, missing multiplicative factors, and inconsistent comparisons. The correction of these issues reduces the discrepancy between energy spectra of convection from time-distance helioseismology and simulations, but does not eliminate it entirely. Additionally, new, consistent results from local correlation tracking and ring-diagram analysis are presented, which are closer to the results derived from time-distance helioseismology than those from simulations.

Zusammenfassung

Das Ziel dieser Thesis ist es, mithilfe von Beobachtungen verschiedene großskalige Strömungen zu charakterisieren, insbesondere die vor kurzem entdeckten solaren Rossby-Wellen (Wellen der radialen Vortizität), großskalige Konvektion, und Strömungen um aktive Regionen. Diese großskaligen Strömungen wechselwirken wahrscheinlich mit der differenziellen Sonnenrotation und, über einen Dynamo-Prozess, mit dem Sonnenmagnetfeld.

Um diese Strömungen zu erforschen, verwende ich mehrjährige Beobachtungen des Helioseismic and Magnetic Imager (HMI) an Bord des Solar Dynamics Observatory (SDO). Diese Daten werden mit zwei sich ergänzenden Methoden zur Messung von Strömungen auf der Sonnenoberfläche und im Sonneninneren verarbeitet: Lokalem Korrelationstracking, welches auf die Sonnenoberfläche beschränkt ist, und Ring-Diagramm-Analyse, mit welcher die oberflächennahen Schichten im Sonneninneren (das Tiefenlimit liegt bei circa 16 Mm) mit niedrigerer zeitlicher und räumlicher Auflösung erforscht werden können.

Zunächst erforsche ich die latitudinale und radiale Abhängigkeit von solaren äquatorialen Rossby-Wellen. Dazu wird die radiale Vortizität aus den horizontalen Strömungen berechnet und eine Spektralanalyse über eine sphärische harmonische Transformation in der Latitude und Longitude und eine Fourier-Transformation in der Zeit durchgeführt. In den oberen 9 Mm unterhalb der Oberfläche ist die radiale Abhängigkeit der Vortizitätseigenfunktionen konsistent mit einer von Modellen erwarteten Änderung der Form r^{m-1}, wobei r die radiale Koordinate und m die longitudinale Wellenzahl ist. Allerdings können die radialen Eigenfunktionen tiefer im Sonneninneren aufgrund von systematischen Fehlern in der Ring-Diagramm-Analyse nicht zuverlässig bestimmt werden. Die Latitudenabhängigkeit der Eigenfunktionen der Moden wird über eine Korrelations-Analyse zwischen dem Äquator und anderen Latituden, und über eine Singulärwertzerlegung bestimmt. Der Realteil der Eigenfunktionen nimmt vom Äquator weg ab und ändert sein Vorzeichen bei absoluten Latituden zwischen 20 und 30°. Dies stimmt mit vorherigen Ergebnissen überein. Der Imaginärteil der Eigenfunktionen besitzt eine kleine Amplitude ungleich Null bei allen Latituden, was eventuell auf einen Dämpfungsprozess deutet.

Anschließend erforsche ich mithilfe von Karten der horizontalen Strömungen das Energiespektrum von großskaliger Konvektion im Kontext vorhandener Ergebnisse, die durch Zeit-Distanz-Helioseismologie und Simulationen erhalten wurden. Diese Ergebnisse hatten eine riesige Diskrepanz für die Geschwindigkeit von großskaliger Konvektion im Sonneninneren offenbart (quadratische Mittelwerte von circa 1 beziehungsweise 100 m s^{-1}). Diese Diskrepanz, das konvektive Dilemma, ist von essenzieller Bedeutung in Bezug auf aktuelle Modelle der Sonnenkonvektion. In der vorhandenen Analyse wurden einige Probleme gefunden, beispielsweise unterschiedliche Konventionen für

sphärische harmonische Transformationen, fehlende multiplikative Faktoren, und inkonsistente Vergleiche. Das Beheben dieser Probleme reduziert die Diskrepanz zwischen den Energiespektren der Konvektion von Zeit-Distanz-Helioseismologie und Simulationen, entfernt sie allerdings nicht vollständig. Zusätzlich werden neue, konsistente Ergebnisse von lokalem Korrelationstracking und Ring-Diagramm-Analyse präsentiert, welche näher an den Ergebnissen der Zeit-Distanz-Helioseismologie als jenen der Simulationen liegen.

1 Introduction

1.1 The dynamic Sun

While the Sun may appear as a static star to the human eye, it is in fact highly dynamic and variable. For example, very soon after the advent of the first telescopes, around 1610, Galileo Galilei observed dark spots on the solar surface moving across the visible disk. It soon became clear that this motion is due to a rotation of the Sun and Galilei was able to calculate the rotation rate of these sunspots. Only a few years later, in 1630, Christoph Scheiner noticed that the sunspots rotate slower at higher latitudes and faster close to the equator and thus introduced the concept of differential rotation to the solar community, i.e. the rotation rate decreases with latitude. Based on his own measurements of the mean synodic sunspot rotation period of 27.2753 days, in 1863, Richard Carrington invented an ordering system of Carrington rotations (CRs), which is still in use nowadays.

Almost at the same time, in 1843, Samuel Heinrich Schwabe observed that the number of sunspots visible on the Sun varies with a period of roughly 10 years (Schwabe 1844). These sunspot or solar cycles actually have an average period of rather 11 years and they are the most easily visible manifestation of solar variability (Fig. 1.1, top panel). 65 years later, George Ellery Hale discovered from the splitting of spectral lines due to the Zeeman effect that the sunspots are intimately linked to the solar magnetic field (Hale 1908). Hale also noticed that sunspots at any given latitude are typically bipolar, with the two polarities of the sunspots being opposite between opposite hemispheres and between successive cycles (Hale's law), while Alfred Harrison Joy found that the leading polarity is typically closer to the equator than the trailing one, with an angle increasing with latitude (Joy's law, Hale et al. 1919). Despite these huge successes, at that time observations of the Sun were unfortunately always limited to the solar surface.

This changed in 1962, with further evidence for solar variability, when Robert Leighton observed that the Sun oscillates with periods predominantly around 5 min, or equivalently frequencies around 3 mHz (Leighton et al. 1962). This discovery formed the basis of helioseismology, the study of the Sun using waves. Similar to seismology on Earth, the waves carry information about the matter they traverse and their frequency is shifted

---

Disclaimer: Several figures in this introduction originate from existing publications and have been reproduced with permission. Figures 1.1, 1.2, 1.3 and 1.7 (top right panel) have been reproduced under the *Creative Commons CC BY license 4.0* (see *https://creativecommons.org/licenses/by/4.0/legalcode*). Figures 1.4, 1.5 (right panel), 1.9, 1.10 and 1.11 have been reproduced under licenses provided by the respective journals via *RightsLink*. Figures 1.6, 1.7 (top left panel) and 1.8 have been reproduced under reproduction rights granted for educational/academic purposes. Figures 1.5 (left panel) and 1.7 (bottom panel) have been reproduced under reproduction rights granted by the American Astronomical Society and IOP Publishing, with the consent of the authors of the respective publications.
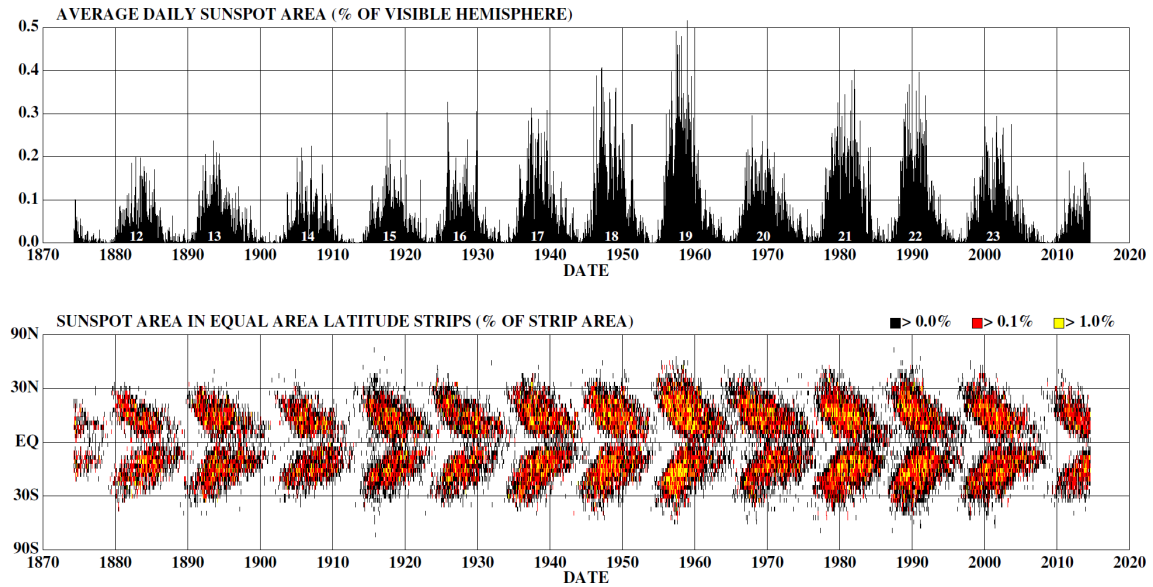
Figure 1.1: The sunspot cycle. Top: Fractional sunspot area of the visible solar disk versus time. Bottom: The solar butterfly diagram. Fractional sunspot area in equal area latitude strips versus time and latitude. From Hathaway (2015), with permission.

along the wave path. The characterization of the waves and the analysis of oscillation power spectra enabled us to look into the solar interior and thus increased our knowledge about the Sun dramatically.

We now know the interior rotation profile for a significant part of Sun (Fig. 1.2), in particular that the differential rotation rate increases with depth close to the surface (in the near-surface shear layer) and that the rotation becomes uniform around $0.7\,R_\odot$ (at the so-called tachocline), see e.g. Howe et al. (2000) and the reviews by Thompson et al. (2003) and Howe (2009). Additionally we know that there is a $\sim 10\,\mathrm{m\,s^{-1}}$ poleward belt flow, the meridional flow (Hathaway 1996). The sunspot area and the magnetic field as a function of time and latitude (Fig. 1.1, bottom panel, and Fig. 1.3), the so-called sunspot and magnetic butterfly diagrams, are routinely recorded nowadays. Both the rotation and the meridional flow vary along with the solar cycle in the form of bands of faster- and slower-than-average velocities (Fig. 1.4), called torsional oscillations (Howard and Labonte 1980) and residual meridional flow (Snodgrass and Dailey 1996, Beck et al. 2002), respectively. This indicates that there is a link between flows and magnetic activity. Helioseismology also allows us to define standard solar reference models such as Model S (Christensen-Dalsgaard et al. 1996) as well as to determine such fundamental parameters as the age of the Sun.

Finally and maybe most importantly, our knowledge about the energy transport in the Sun has improved significantly thanks to helioseismology, through interior density and sound speed profiles. These results enabled us to locate the base of the solar convection zone at roughly $0.7\,R_\odot$, close to the tachocline (Christensen-Dalsgaard et al. 1991). Below this region, energy generated by nuclear hydrogen fusion in the solar core is carried by photons, while above convection (plasma motions carrying heat) dominates the energy transport. At the same time we think that the majority of magnetic flux originates at the base of the convection zone and moves toward the surface in the form of flux tubes. There
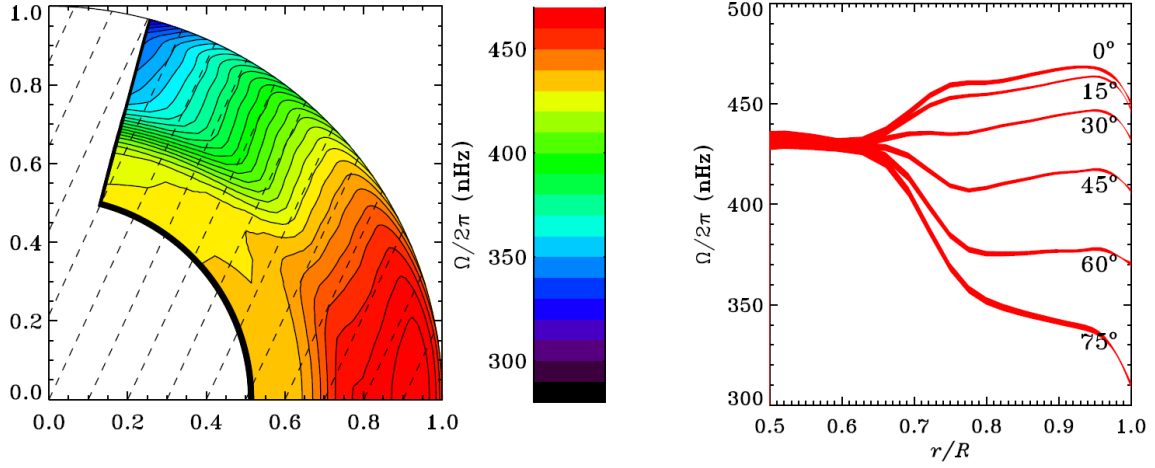
Figure 1.2: The solar differential rotation. Left: Contours of the rotation rate in a meridional plane (the solar rotation axis is pointing upwards). The dashed lines indicate a 25° angle from the rotation axis. Right: Rotation rate versus radius, for different latitudes. From Howe (2009), with permission.
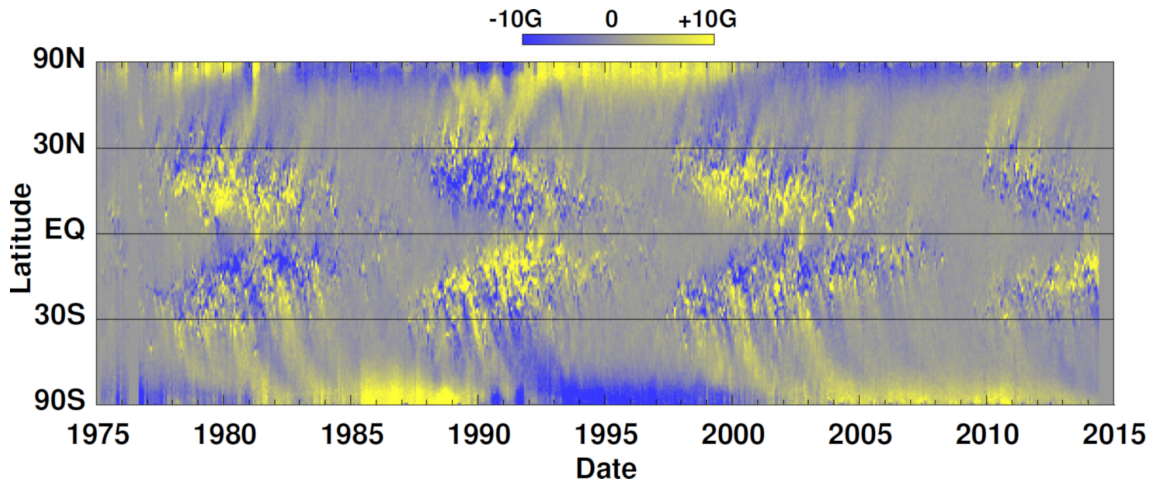
Figure 1.3: The solar magnetic butterfly diagram. Radial magnetic field, averaged over longitude, versus time and latitude. The image also visualizes Hale's law and Joy's law (see text). From Hathaway (2015), with permission.
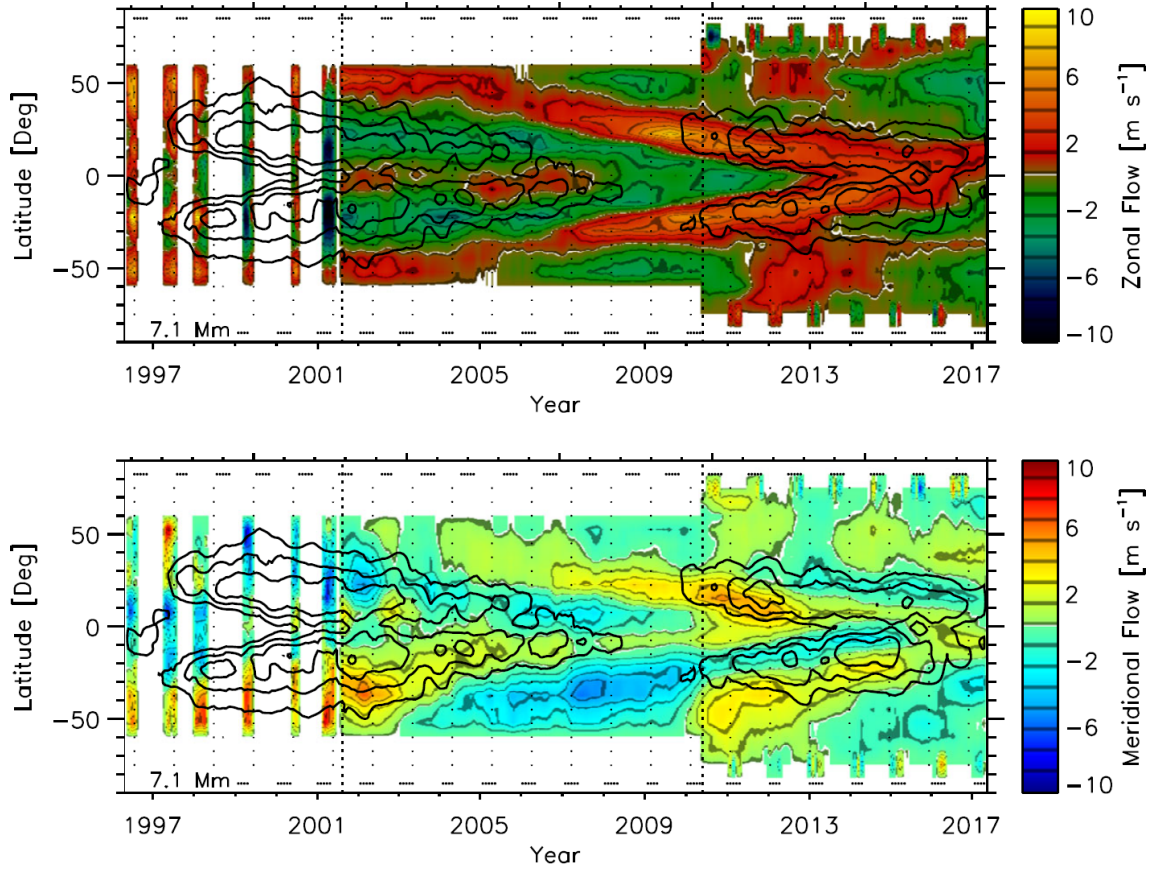
Figure 1.4: Top: Torsional oscillations, i.e. zonal flows as a function of time and latitude after subtraction of the time-independent component and averaged over longitude. Bottom: Residual meridional flow, i.e. the analogue for the meridional flows. Positive velocities indicate prograde and northward motions, respectively. The images combine data at a depth of 7.1 Mm from three different instruments, with different observation periods (vertical dashed lines). The solid black lines show magnetic field contours (5, 10, 20 and 40 G), smoothed over five solar rotations. From Komm et al. (2018), with permission.

it appears in the form of patches of high magnetic field (active regions) and their intensity counterparts, sunspots (which appear dark as they are cooler than their surroundings due to the magnetic field inhibiting the convection), see Parker (1955) and Cheung et al. (2010).

The deep connection between the solar activity and flows then naturally raises the question as to how the magnetic field and the differential rotation are maintained via a solar dynamo process and also how large-scale flows come into play there. For a review on large-scale dynamics in the convection zone, we refer the reader to Miesch (2005). Apart from the rotation and the meridional circulation, such large-scale flows include for example convective motions, flows around active regions and a new, recently observed type of waves known as Rossby waves. As this thesis is indeed about observations of large-scale flows in the solar interior, in the following sections we want to give further details on each of them.

1.2 Flows in and on the Sun

1.2.1 Rossby waves

Rossby waves were first described in detail by Rossby (1939) and Rossby (1940). They can exist on rotating fluid bodies and are a type of inertial waves. As such their restoring force is the Coriolis force. In particular, most relevant for the existence of Rossby waves is that the strength of the Coriolis force, quantified by the Coriolis parameter $f = 2\Omega \sin \lambda$ (with Ω the angular rotation rate related to a rotation vector $\mathbf{\Omega} = \Omega \hat{z}$), depends on the latitude λ. Let us briefly see why this causes an oscillatory motion. **Here, we describe the Rossby waves in the framework of the** shallow-water-approximation**, i.e. we consider a fluid whose horizontal length scale vastly exceeds its vertical length scale. The vertical flow velocity is considered to be small compared to the horizontal flow velocity. The flow is assumed to be incompressible, i.e. the fluid should be divergence-free, and only one depth layer (the surface) is taken into account.**

Assume that we have a small fluid parcel that rotates with the body. We assume that the parcel initially does not have any relative vorticity, i.e. $\zeta_r = \nabla \times \mathbf{u} = \mathbf{0}$ (for any velocity $\mathbf{u}$). However, the rotation itself causes a planetary vorticity $\zeta_p = 2\mathbf{\Omega}$. Under the assumption that all motions occur only horizontally on the surface of the body, the relevant contribution to ζ_p is essentially the locally vertical (radial) component $f\hat{r}$. Therefore when the parcel is perturbed and displaced in latitude (say locally northward), this results in a change of the planetary vorticity ζ_p. However, because the potential vorticity, closely related to the absolute vorticity $\zeta_a = \zeta_r + \zeta_p$, must be conserved, this then induces a relative vorticity that is in the opposite direction. In this way the change of the Coriolis force with latitude provides a restoring force, causing the wave motions of the Rossby waves.

From theory, we know that Rossby waves obey a simple relation between frequency ω and wavenumber (azimuthal order m, angular degree ℓ). Their dispersion relation is

$$\omega = -\frac{2\Omega m}{\ell(\ell + 1)}. \tag{1.1}$$

The minus sign shows that the phase speed of the Rossby waves is negative and that these waves thus propagate in the retrograde direction. The above dispersion relation can be derived from the equation of motion (momentum equation), including the Coriolis term, but it requires three assumptions. First, the fluid body is assumed to rotate uniformly, i.e. Ω is constant. The second assumption is that the flows are restricted to the surface of the sphere and purely horizontal, i.e. there are no radial motions. Finally, it is assumed that the horizontal divergence of the flows is zero, i.e. there are no sources or sinks of the flows. This implies that the horizontal velocities are purely vortical and can be written as the curl of a stream function $\psi(\lambda, \varphi)$ that depends on latitude λ and longitude φ and which points radially away from the surface. Theory suggests that the flow field associated with single Rossby wave modes (Fig. 1.5, left panel) is given by spherical harmonics (Saio 1982). If $\psi(\lambda, \varphi)$ is proportional to sectoral ($\ell = m$) spherical harmonics (we will see in Sect. 2.4.3.3 that the $\ell = m$ component is the dominant contribution in horizontal Rossby wave eigenfunctions of the radial vorticity), the prograde flow $u_x = \frac{\partial \psi}{\partial \lambda}$ is anti-symmetric in latitude and the northward flow $u_y = \frac{1}{\cos \lambda} \frac{\partial \psi}{\partial \varphi}$ is symmetric. These symmetries can also be seen in the left panel of Fig. 1.5.
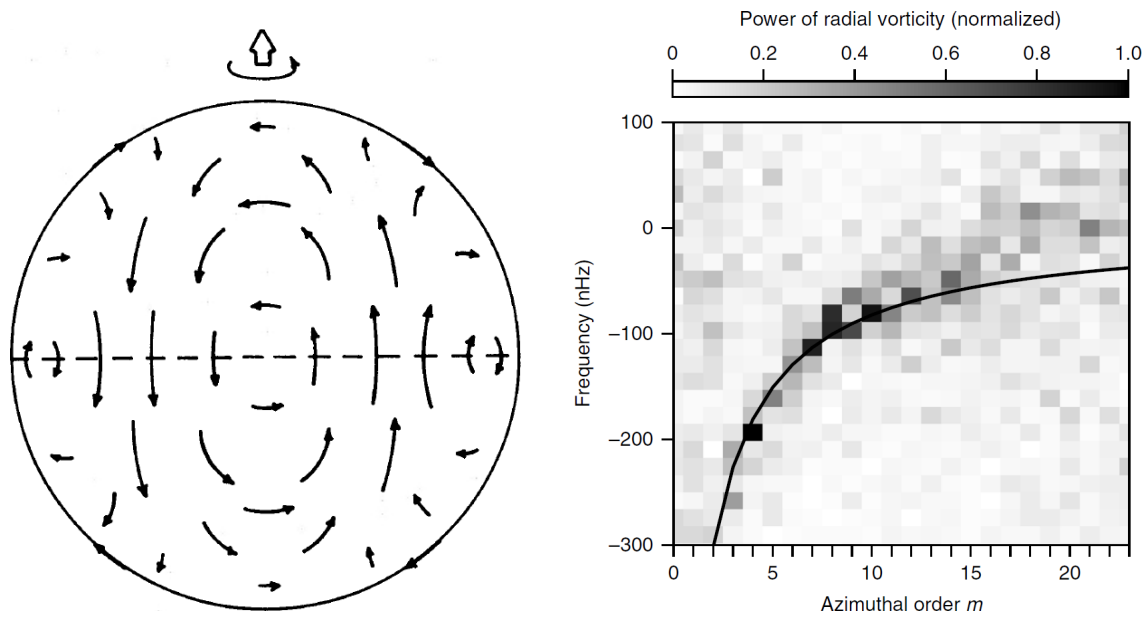
Figure 1.5: Left: Schematic flow field for the Rossby mode with $\ell = m = 3$. Rossby waves are retrograde-propagating vortex patterns. From Saio (1982), ©AAS. Reproduced with permission. Right: Power spectrum of solar Rossby waves. The power of the radial vorticity is shown as a function of frequency and azimuthal order in the co-rotating reference frame. The solid black line indicates the simple theoretical dispersion relation for the sectoral ($\ell = m$) case (see text). Rossby wave modes are detected for $m \geq 3$. From Löptien et al. (2018), with permission.

Rossby waves were first discovered on Earth, where they appear in the atmosphere, but also in the ocean (Chelton and Schlax 1996). The atmospheric Rossby waves are connected to large-scale meanders observed in the jet stream and to the transport of cold air from the poles toward the equator and of hot air from the tropics toward the poles (e.g. Holton 2004). The oceanic Rossby waves are important for the propagation of ocean-climate signals, such as the El Niño phenomenon (Lachlan-Cope and Connolley 2006). On Earth, Rossby waves thus play a key role in shaping the weather and climate.

However, while the theoretical existence of Rossby waves on the Sun was already postulated roughly 40 years ago (Papaloizou and Pringle 1978), the observational history of solar Rossby waves was for a long time marked by ambiguous detection claims (Kuhn et al. 2000, Williams et al. 2007, Sturrock et al. 2015, McIntosh et al. 2017). Only very recently, Löptien et al. (2018) provided convincing observational evidence for solar Rossby waves (including an identification via the dispersion relation). Löptien et al. (2018) used flow measurements obtained from local correlation tracking (Sect. 1.5.1) to study the radial vorticity field on the Sun and they detected a large-scale (azimuthal order $m \leq 15$) oscillatory pattern near the equator, with lifetimes of several months. The observed dispersion relation of these waves is consistent with the textbook equation (Eq. 1.1) for the case of sectoral waves, i.e. $\omega = -2\Omega/(m + 1)$, where $\Omega/2\pi = 453.1$ nHz is the equatorial rotation rate of the Sun (Fig. 1.5, right panel). Löptien et al. (2018) also showed that the eigenfunctions of solar Rossby waves are not the purely sectoral spherical harmonics expected from early theories (Fig. 1.5, left panel).

Liang et al. (2019) later confirmed the Rossby wave detection of Löptien et al. (2018) via time-distance helioseismology (TD, Duvall et al. 1993). Time-distance helioseismology is a widely used method of local helioseismology (Sect. 1.5.2). The basic idea is that, in the presence of a flow, waves travelling between two points on the solar surface propagate faster in the direction of the flow than against it. This directional asymmetry can be measured in the form of travel-time differences which can be converted into flow velocities by solving an inverse problem. Via different measurement geometries, flows in the prograde or the northward direction and even the horizontal divergence and the radial vorticity can thus be retrieved. Further information about time-distance helioseismology can be found for example in Gizon and Birch (2005). The Rossby wave confirmation by Liang et al. (2019) is crucial since it relies on an independent method and thus shows that the results obtained by Löptien et al. (2018) are robust. Hanasoge and Mandal (2019) and Mandal and Hanasoge (2020) also detected and characterized Rossby modes with odd m via yet another method called normal-mode coupling. Another Rossby wave confirmation was provided by Hanson et al. (2020) via ring-diagram analysis.

It has been suggested that Rossby waves could help in maintaining the solar differential rotation (Ward 1965) or zonal jets on Jupiter (Liu and Schneider 2011). However, purely sectoral Rossby waves do not transport angular momentum. Gilman (1969) and Wolff and Hickey (1987) proposed that the magnetic field could be modulated by Rossby waves. It might also be interesting to study the possible interactions between convection and the Rossby waves, (e.g. Vallis and Maltrud 1993). While much of this is currently not much more than speculation, for sure the discovery of solar Rossby waves opens a new way to probe the solar interior. Similar to other, well-known types of waves commonly used in helioseismology, mode frequencies and eigenfunctions can be measured for Rossby waves. This might allow us to test the validity of existing Rossby wave theories and to study the effects of differential rotation and potentially the magnetic field on this type of waves.

1.2.2 Convective flows

As briefly mentioned before, the transfer of energy generated via hydrogen fusion inside the Sun relies on two different physical processes. In the inner 70 % of the solar radius radiative transfer (i.e. via photons) is the dominant transport mechanism while in the outer 30 % convection (i.e. bulk plasma motions) carries the energy outwards (Fig. 1.6). Most interestingly, the convection and the related flows occur in a cell-like form on distinct spatial scales. This has led to a categorization into granules, supergranules and giant cells.

Granulation (Fig. 1.7, top left panel) is the smallest scale of convection and was first observed by Herschel (1801). The term refers to the grainy patterns seen on intensity images of the Sun. Granules are visible as small bright cells with a diameter of roughly 1-2 Mm (Rieutord et al. 2010), or equivalently an angular degree of $\ell \sim 2000\text{-}4000$. These cells are relatively shallow and separated by dark narrow lanes, the intergranular network. Granules have a vertical extent of roughly 300 km or less (Nordlund et al. 2009). They have short lifetimes of $\sim$ 10 min. The flows on this scale have velocities typically around 1-3 km s^{-1} as seen in simulations (Stein and Nordlund 1998, Nordlund et al. 2009) and observations (Oba et al. 2017), although in rare cases granules can also reach very high
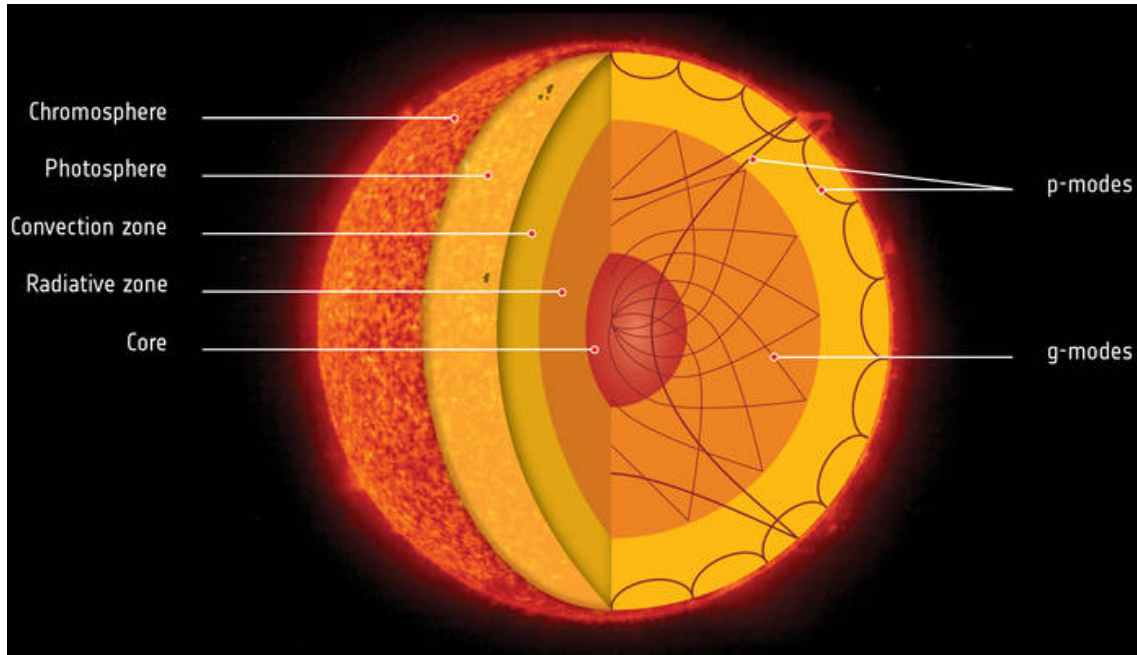
Figure 1.6: Interior solar structure. The energy is transported outwards from the solar core through radiation in the inner and through convection in the outer layer, until it reaches the visible surface, the photosphere. By using solar oscillations that pass through the optically thick matter below the photosphere, probing different regions, we can study the solar interior (see text). From *https://www.esa.int/Science_Exploration/Space_Science/ Gravity_waves_detected_in_Sun_s_interior_reveal_rapidly_rotating_core*, courtesy of ESA/NASA, with permission.

velocities up to $\sim 10\,\mathrm{km\,s^{-1}}$. Plasma moves upwards until it reaches the surface, where it diverges horizontally and is radiatively cooled. In this process, the ionized hydrogen captures free electrons and releases ionization energy in the form of photons. The still partially ionized plasma then concentrates in cooler downflow lanes, sinks into the solar interior and is heated and ionized anew. Granulation is well reproduced by simulations, see e.g. the review by Nordlund et al. (2009).

Supergranulation (Fig. 1.7, top right panel) occurs on a larger spatial scale around angular degree $\ell \sim 120$ (Hathaway et al. 2000). This means that supergranules have typical length scales on the order of 30 Mm. Their discovery is attributed to Hart (1954). Unlike granules, this convective scale is best observed in the line-of-sight (LOS) velocity, i.e. in Dopplergrams, where the supergranulation can be seen as a pattern covering the whole visible solar disk. Supergranules also evolve on much longer timescales than granules, with typical lifetimes of 1-2 days. Their flows have amplitudes of approximately $300\,\mathrm{m\,s^{-1}}$ in the horizontal direction and are much weaker in the vertical direction (Rincon and Rieutord 2018). The flows can be easily observed in maps of the horizontal divergence. There is a wide variety of open questions concerning the Sun's supergranulation, as described in the review by Rincon and Rieutord (2018). Contrary to granulation, which is relatively well understood and successfully reproduced in simulations, the origin of the supergranulation is not clear yet. Although thermal convection is the most likely explanation of its existence, we do not yet understand why supergranulation stands out as

a distinct scale of convection. Also, it is currently unknown how deep exactly the super-granules extend into the convection zone. Supergranules are known to rotate faster than their surroundings and Gizon et al. (2003) suggested that this apparent super-rotation is linked to a wave-like character of this convective scale. Further evidence for this was given by Schou (2003) and Langfellner et al. (2018).

Giant cells (Fig. 1.7, bottom panel) are the largest scale of convection, with horizontal extents of $200\,\mathrm{Mm}$ ($\ell \sim 20$) or more (e.g. Miesch et al. 2008). Typical velocity scales for the largest cells should be $100\,\mathrm{m\,s^{-1}}$ or less. Although scientists hypothesized on the theoretical existence of giant cells not long after the supergranulation pattern had been detected (Simon and Weiss 1968), this scale of convection continues to remain elusive even nowadays: Although they clearly appear in simulations (Miesch et al. 2008), unfortunately convincing observations for giant cells are sparse at this moment. While Hathaway et al. (2013) claim to have detected evidence for giant convection cells at high latitudes (around $\pm 60°$) in flow maps, it is currently unclear whether the observed large-scale features are indeed of convective origin. The authors report lifetimes of at least a few months, in line with theoretical expectations. Giant cells are likely strongly affected by the solar differential rotation, possibly being sheared by it. Likewise they could potentially play an important role in angular momentum transport from the higher latitudes to the equator and could thus help in maintaining the latitudinal rotation gradient (Hathaway et al. 2013).

While the convective energy spectrum at large angular degrees (small spatial scales) and close to the surface is comparatively well understood, the dynamics are much less clear deeper in the convection zone and at large spatial scales. Below, we want to briefly introduce several existing results. These results will be re-evaluated in Chap. 3.

Hanasoge et al. (2010) and subsequently Hanasoge et al. (2012) have employed time-distance helioseismology to obtain horizontal flows. They applied a spectral analysis on their obtained horizontal flows to estimate the strength of the convection at $0.96\,\mathrm{R_\odot}$, up to $\ell \sim 60$ (Fig. 3.1, Original HDS2012). The measured root-mean-square (rms) velocities (on the order of $1\,\mathrm{m\,s^{-1}}$) and the energy were roughly two and four orders of magnitude smaller, respectively, than those reported from previous simulations by Miesch et al. (2008) with the Anelastic Spherical Harmonics code (ASH, Clune et al. 1999, Brun et al. 2004) at $0.98\,\mathrm{R_\odot}$ (Fig. 3.3, ASH). The ASH code simulates the entire convection zone in a spherical geometry at low resolution/low ℓ.

If the Hanasoge et al. (2012) measurements were true, this would have serious consequences for the solar angular momentum transport. It would also imply that current models of convection such as the mixing length theory (convective parcels travel over a certain mixing length, keeping their identity, and then release their energy and dissolve into their surroundings, see Prandtl 1925 and Böhm-Vitense 1958) and modern simulations, e.g. with the ASH code, fail to accurately describe the physics occurring inside the Sun. Evidently the consequence would be no less than the need to completely rethink our picture of convection (Gizon and Birch 2012). This is also referred to as the convective conundrum.

Gizon and Birch (2012) showed another, independent, simulation result at $0.98\,\mathrm{R_\odot}$, inferred using the stagger code (Fig. 3.3, stagger) from Stein and Nordlund (2006). Stagger simulates layers close to the surface at high resolution/high ℓ. Additionally, Gizon and Birch (2012) presented an energy spectrum (Fig. 3.1, Original R2012) from Roudier et al. (2012), who used granulation tracking (Sect. 1.5.1) to derive horizontal velocities
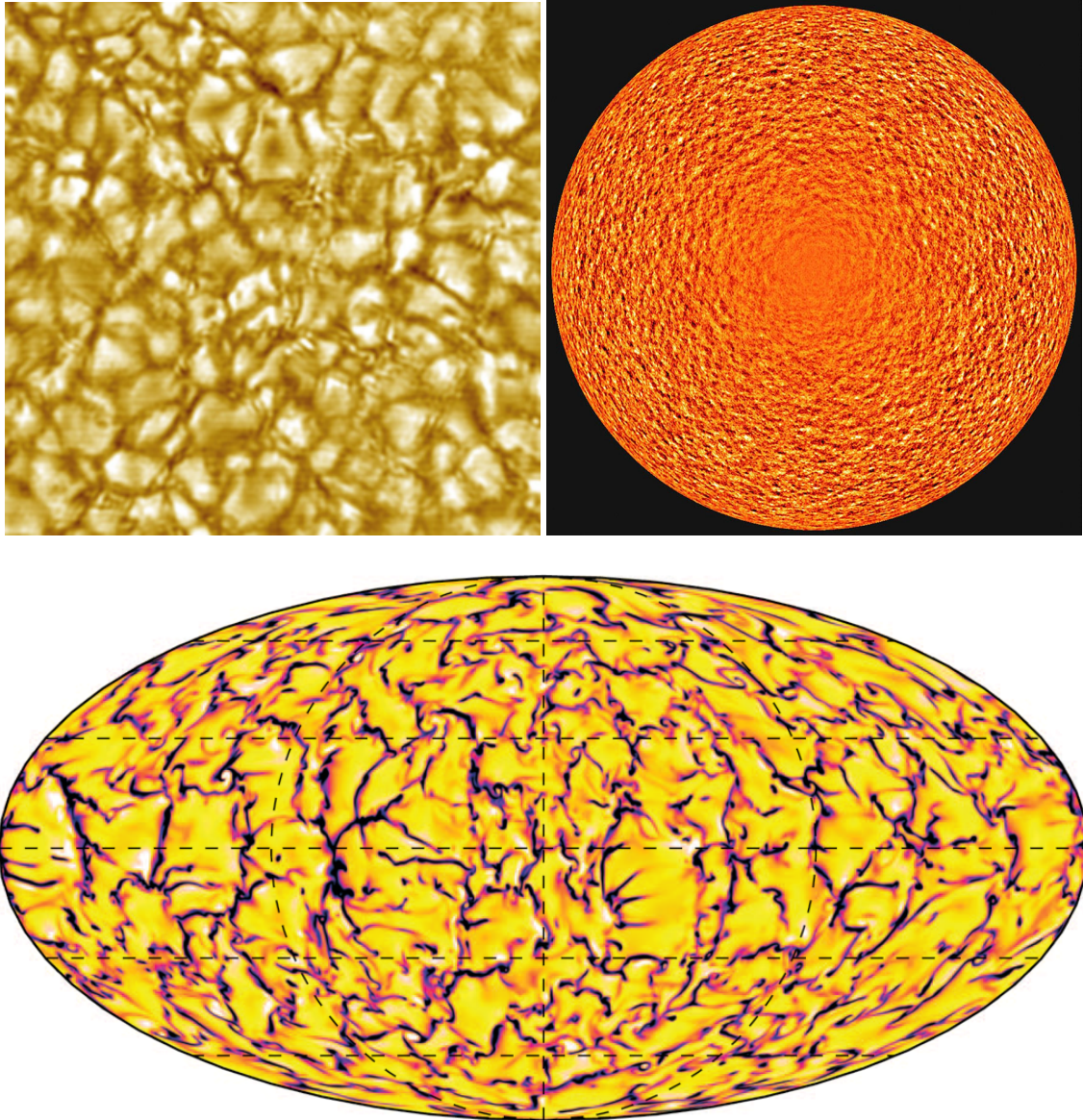
Figure 1.7: Convective scales of the Sun. Top left: Granulation appears as a small-scale cell-like structure in solar intensity images. From *https://apod.nasa.gov/apod/ap051106. html*, courtesy of NOAO/AURA/NSF, with permission. Top right: Supergranulation as seen in Dopplergrams of the full solar disk. The pattern is more prominent close to the limb as supergranular flows are mostly horizontal. From Rincon and Rieutord (2018), with permission. Bottom: Giant cells as seen in a radial velocity image from simulations of the Sun. The observational evidence for giant cells is still sparse. From Miesch et al. (2008), ©AAS. Reproduced with permission.

on the solar surface at intermediate ℓ. The stagger and the Roudier et al. (2012) results were inconsistent with the ASH simulation. A lower theoretical bound from Miesch et al. (2012), also presented by Gizon and Birch (2012), was above the Hanasoge et al. (2012) estimates.

Greer et al. (2015) investigated the energy spectrum of large-scale convection at $0.96\,R_\odot$ (Fig. 3.1, Original GHFT2015) using a particular type of ring-diagram analysis (Sect. 1.5.2). The resulting energy spectrum was again mostly consistent with the ASH results.

Finally, Hanasoge et al. (2016) summarized the existing results and showed another estimate of the large-scale convective energy from Hathaway et al. (2013), where the authors used supergranulation tracking (similar to granulation tracking, Sect. 1.5.1) to obtain the horizontal velocities. This estimate was larger than that from Hanasoge et al. (2012) by roughly one order of magnitude.

1.2.3 Flows around active regions

We have already established that there is a close connection between large-scale flows and the solar magnetic field. It thus comes as no surprise that there are also large-scale flows surrounding active regions, where the magnetic flux is particularly large. These flows around active regions have been first observed on the solar surface by Gizon et al. (2001). The authors found that the flows are spatially extended and flow amplitudes were measured to be around $50\,\mathrm{m\,s}^{-1}$. Moreover, the flows were converging into the active region, but the authors also detected outflows (called moat flows) at further distances from the sunspots (beyond the so-called penumbra).

Several papers confirmed these flows and investigated their properties independently with a different helioseismology method (Haber et al. 2004, Hindman et al. 2004, 2009). These papers demonstrated that at larger depths there seem to be outflows from active regions rather than inflows. The authors also found smaller flow amplitudes of roughly 20-$30\,\mathrm{m\,s}^{-1}$. The flows could be observed up to $10°$ from the active region center.

As active regions can greatly vary in size, shape and lifetime, a solid statistical sample is crucial for studies of the flow patterns in their vicinity. Löptien et al. (2017) confirmed the presence of active region inflows with local correlation tracking (Sect. 1.5.1). By averaging flow maps for many active regions, they found that the inflow is not symmetric, but rather converges toward the trailing polarity.

Finally, Braun (2019) used a large sample of active regions and divided it into several bins of magnetic flux. They confirmed the prevalent inflows to the trailing polarity and demonstrated that they are not strongly dependent on the magnetic field strength. Braun (2019) also observed a retrograde flow at the poleward side of the active regions (and weaker on the equatorward side), which had not been found in previous studies, and discussed how much the active region flows may contribute to time-varying larger-scale flows such as torsional oscillations or the residual meridional flow.

The dynamics of active regions is a topic of active research, because flows around active regions are thought to interact with, for example, the meridional flow. The latter is a key ingredient in flux transport models (Jouve and Brun 2007), where the poleward transport of magnetic flux plays a crucial role in the polarity reversal of the polar magnetic field, which itself is of importance for solar cycle predictions. The inflows might counteract the diffusion of the magnetic field in active regions by convection and thus could help

in keeping the magnetic flux concentrated (De Rosa and Schrijver 2006, Martin-Belda and Cameron 2016). Feedback mechanisms associated with active region flows could potentially also modulate the amplitude of the solar cycle (Cameron and Schüssler 2012). We refer the reader to Charbonneau (2010) for a review of various dynamo models.

1.3 Motivation for the thesis

The previous sections have shown the importance of various large-scale flows for our understanding of solar dynamics: The interplay of Rossby waves, convective flows and flows around active regions, in connection with differential rotation and meridional circulation, but also the magnetic field, has far-reaching consequences for basic solar physics models. This thesis therefore focuses on observations of large-scale solar flows.

While Löptien et al. (2018) and Liang et al. (2019) successfully detected and identified solar Rossby waves and measured the wave frequencies, the question of how Rossby modes behave as a function of latitude and depth was only briefly addressed. However, it is crucial to understand the dependence of the waves on these spatial coordinates. A solid characterization of the mode sensitivity will allow us to understand which latitudes and depths can be probed with Rossby modes and, potentially serving as a test bed for different Rossby wave theories, may give us valuable information on mode physics in general. We therefore want to study the latitude and depth dependence of the Rossby waves.

As mentioned, the disagreement between various results regarding the strength of deep, large-scale convective flows, the convective conundrum, fundamentally puts our current view of solar turbulence in question. This motivates our study of deep, large-scale convection, where we show that the analysis that led to these former results contains various errors. While we will see that these errors are not the main cause of the discrepancy, the corrected curves presented by us together with new results will help build a solid foundation for future investigations.

1.4 Data used in the thesis

In this thesis, we use data from the Solar Dynamics Observatory (SDO, Pesnell et al. 2012). SDO is a satellite which has been launched into a geosynchronous orbit (following the Earth's rotation) in February 2010. It collects data since April 2010 via three instruments. Among these are the Atmospheric Imaging Assembly (AIA) and the Extreme Ultraviolet Variability Experiment (EVE). The data in this thesis, however, are from the Helioseismic and Magnetic Imager (HMI, Schou et al. 2012, Scherrer et al. 2012).

This instrument observes the full visible disk of the Sun with a high temporal cadence of 45 or 720 s and a high spatial resolution of 4096×4096 pixels. It was designed to study both solar oscillations and the solar magnetic field, both on the surface and in the interior. To this extent HMI obtains various kinds of raw data, which are then pre-processed and made publicly available in the form of different data products.

These include for example images of the vector magnetic field and of the line-of-sight magnetic field (magnetograms), but also intensity images of the Sun, obtained in the continuum around the Fe I 6173 Å line, and Dopplergrams, which give the velocity in the
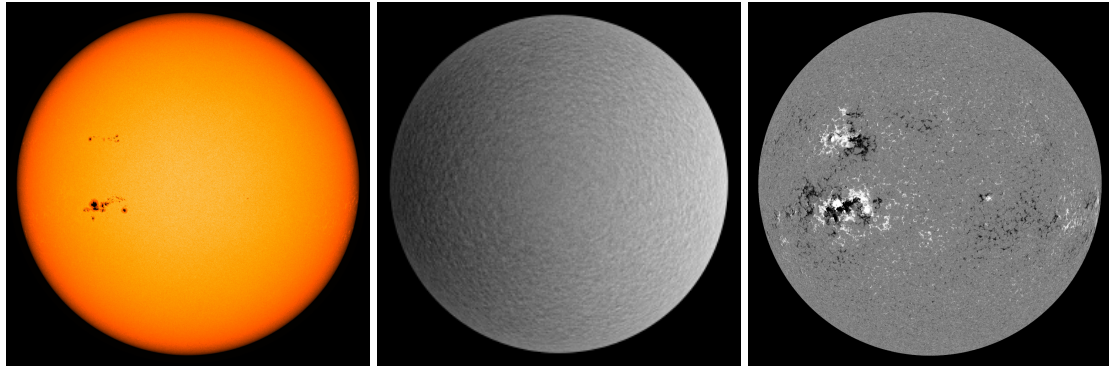
Figure 1.8: Basic HMI data products. Left: Continuum intensity on February 1, 2014. Several sunspots are clearly visible. Middle: Line-of-sight velocity on September 30, 2019. Black and white indicate plasma moving toward and away from the observer, respectively. Right: Line-of-sight magnetic field on February 1, 2014. Black and white indicate magnetic field lines pointing away from and toward the observer, respectively. Active regions (with high absolute field strengths) can be associated with the sunspots in the intensity image. From HMI quick-look data (*http://jsoc.stanford.edu/data/hmi/ images/latest/*), courtesy of NASA/SDO and the HMI science team, with permission.

line-of-sight direction as measured from the wavelength shift of that Fe I line due to the Doppler effect (Fig. 1.8).

1.5 Processing methods used in the thesis

While the aforementioned data are without doubt useful for various kinds of analysis, they often are not immediately usable for the study of solar flows, which typically requires knowledge about the horizontal velocities on the solar surface and in the solar interior. The basic question that this section wants to address is thus "How can we infer horizontal velocities from the basic HMI data products?". As we will see, there are multiple ways to obtain these velocities, such as local helioseismology. There are however also methods independent from local helioseismology such as local correlation tracking. Both local helioseismology and local correlation tracking are used for the analysis presented in this thesis. The following sections thus intend to illustrate these techniques in some detail.

1.5.1 Local correlation tracking

Local correlation tracking (LCT) is was first used in the solar context by November and Simon (1988), who also coined the name of this technique. However, the basic principle behind this analysis method dates back further, since it was used in image processing for other fields before. Essentially it relies on tracking the motion of features and thus retrieving the related velocities.

Suppose, for example, that we have a flow on the solar surface. Granules, the small convection cells visible in intensitygrams, that are embedded in this flow field, will then be advected. Consequently, if we take two intensity images at slightly different time steps, the positions of the granules will change (Fig. 1.9). By measuring this change in position

Figure 1.9: Local correlation tracking (granulation tracking). At a time step t, a small window (red shaded oval) containing several granules (outlined by solid black lines) is selected on an intensity image of the Sun. At a later time step $t+\Delta t$, the granules inside the window (dark red filled areas) have moved outside the window due to their proper motion. By following the granule motion via measuring the pixel shift between the two images, horizontal flows can be determined. From Hanasoge et al. (2016), with permission.

and dividing it by the known time difference between the two images, it is then possible to infer the horizontal velocity of the underlying flow field.

An important caveat is that the time difference between the two images should be short compared to the lifetime of granules, since otherwise the evolution of the granules, for example changes in granule shape, may lead to a misdetermination of velocities. The typical granule lifetime of roughly 10 min thus inherently limits the time lag between the intensitygrams to a few minutes or less. Also, since granules are very shallow, local correlation tracking is only sensitive to flows at the solar surface. Due to the usage of the granules as tracers of the flow the method is often referred to as granulation tracking. However, supergranulation tracking is possible as well, most easily using Dopplergrams, where the supergranules are best visible. Naturally, owing to the longer lifetime and the bigger spatial scale of supergranules (roughly 1-2 days and 30 Mm), these features allow longer time lags between the input images, but with a worse spatial resolution.

In practice, a number of different implementations of granulation tracking exists. Among them are the coherent structure tracking (CST, Rieutord et al. 2007) and the Fourier local correlation tracking (FLCT, Fisher and Welsch 2008, Welsch et al. 2004). The conceptual difference between the two algorithms is that FLCT, contrary to CST, also accounts for the intergranular lanes. We refer the reader to Tremblay et al. (2018) for a detailed comparison between these and other implementations of granulation tracking.

One of the two flow velocity datasets we will use in this thesis is based on the FLCT code. The code schematically works as follows: The code requires two input images as a function of pixel coordinates x and y. For each individual reference pixel in either of the two images, sub-images are created by multiplying the corresponding image with a 2D Gaussian function (separable in x and y), that drops with the distance from the reference pixels. This naturally decreases the weight of pixels far away from the reference. A crucial parameter for this windowing operation is σ, the standard deviation of the 2D Gaussian function, which sets the typical length scale of the structures for which the code will determine the pixel shifts. Too large windows will smear out the resulting velocities, such that spatial resolution is lost, while too small windows will lead to high noise. Once the sub-images have been created, the FLCT code computes the cross-covariance of all combinations of sub-images as a function of pixel shifts δx and δy. This cross-covariance

is computed via Fourier transforms. The pixel shifts for which the sub-images match best are then obtained by finding the maximum of a quadratic Taylor expansion to the absolute of the cross-covariance function. The output 2D pixel shift for each pixel is then converted to a 2D velocity vector through division by the time lag δt between the two input images. For further details, we refer the reader to Fisher and Welsch (2008).

Löptien et al. (2017) have used the FLCT code to obtain maps of the horizontal velocity to study flows around active regions. For this they applied the FLCT code to pairs of continuum intensity images observed by HMI between May 19, 2010 and March 31, 2016. The two images in each pair are separated by $\delta t = 45$ s (thus much less than the granule lifetime) and the pairs are separated by 30 min for computational reasons. The parameter σ was chosen to be 6 pixels, which for HMI corresponds to roughly 2 Mm at disk center and thus roughly granule scales. Due to the presence of systematic effects in the output velocity maps, such as the shrinking-Sun effect (Lisle et al. 2004, Löptien et al. 2016), the data were then expanded into Zernike polynomials, an orthogonal basis on the 2D disk. Temporal frequencies of one year and one day (and harmonics up to the Nyquist frequency), which are related to the orbit of the SDO satellite, as well as the zero frequency were then removed via Fourier filtering of the Zernike coefficient time series. The filtered output velocities were converted from the CCD coordinate grid to heliographic coordinates. Finally the mtrack module was used to track the data at the sidereal Carrington rate of 456.0 nHz (roughly 25.38 days) and to map them onto a plate carrée (equirectangular) grid with a spatial sampling of 0.4°. The output data series of surface velocities as a function of time, latitude and longitude was also used by Löptien et al. (2018) to study Rossby waves.

1.5.2 Local helioseismology: ring-diagram analysis

Local helioseismology (see e.g. the review by Gizon and Birch 2005) makes use of waves that are stochastically excited by convection. These waves can be observed in a power spectrum, where they appear as distinct ridges (Fig. 1.10). The waves are categorized into pressure/p-modes, which are acoustic waves whose restoring force is pressure, internal gravity/g-modes, which are driven by buoyancy, and fundamental/f-modes (also called surface gravity waves), which are similar to the deep ocean waves observed on Earth. These waves travel through and probe different regions within the solar interior (Fig. 1.6). For example, g-modes are sensitive to the radiative core of the Sun, but they have not yet been convincingly observed, since their amplitude drops strongly with increasing distance from the Sun's core. The f-modes on the other hand probe only a very shallow region near the solar surface, whereas the p-modes are trapped within the convection zone. The ray paths of those waves are reflected at an upper turning point near the solar surface (due to a strong decrease in density) and they become horizontal and then refracted at a lower turning point (due to an increase in sound speed with depth). Additionally their frequency is modified by changes in the sound speed or the density of the matter they traverse, but also due to local flows.

An application of this is the local helioseismology technique of ring-diagram analysis (RDA, Hill 1988), which determines horizontal velocities from distortions of the wave frequencies due to local flows. For this, for each time step, Dopplergrams of, for example, the full disk are split into small patches, which are called tiles. For each of these tiles a
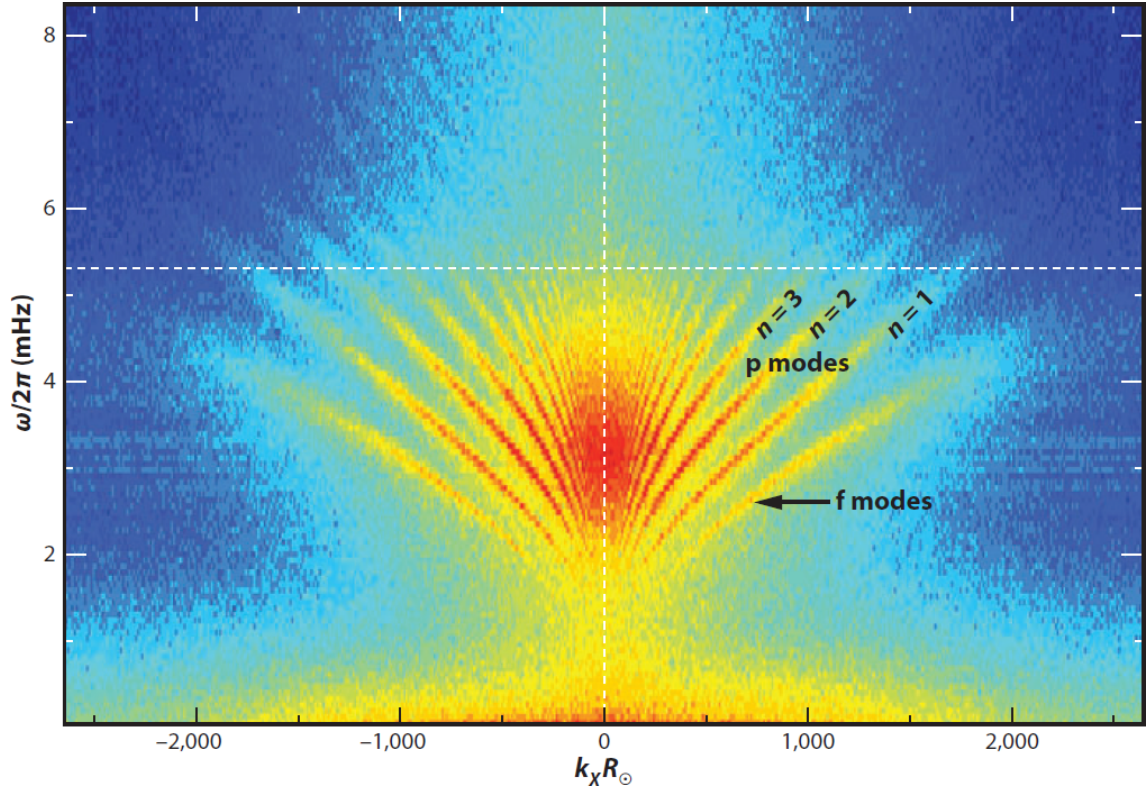
Figure 1.10: Solar power spectrum. Power of Doppler velocity versus frequency and horizontal wavenumber k_x. The power is contained in distinct ridges, which belong to different wave modes (see text). From Gizon et al. (2010), with permission.

local 3D power spectrum is computed, i.e. the power of the LOS velocity as a function of angular frequency ω and two wavenumber directions k_x and k_y. These local power spectra contain the signature of the solar waves: The 2D power as a function of ω and the wavenumber $k = \sqrt{k_x^2 + k_y^2}$ (or an angular cut in the k_x-k_y plane) appears in the form of distinct ridges (Fig. 1.10). The lowest of these ridges corresponds to the f-mode, above which there are the p-modes with an increasing number of radial nodes (ascending radial order n). The 3D power spectrum resembles a trumpet-like structure, for each mode (Fig. 1.11, left panel).

In the absence of flows, this power should be isotropic, since there is no preference for any particular direction. Thus, when viewed at constant ω, we would see concentric circles of power. However, if there is a flow, the Doppler effect will cause the frequency to be increased in the direction of the flow and decreased against it (Fig. 1.11, middle panel). This leads to a tilt of the power rings and therefore in the k_x-k_y plane the circles are deformed into ellipses and additionally their center may be shifted. This explains why the method is called ring-diagram analysis: The distortion of the rings contains information about the flows through which the solar waves propagate. Therefore by fitting the shape of the rings it is possible to get the velocity for each individual mode (at each tile).

In practice, the fitting is often done by keeping the wavenumber k constant and fitting the ridges in the ω-ψ plane, where ψ is the azimuthal angle in the k_x-k_y plane. The rings are basically unwrapped and the distortion caused by the Doppler effect due to a flow
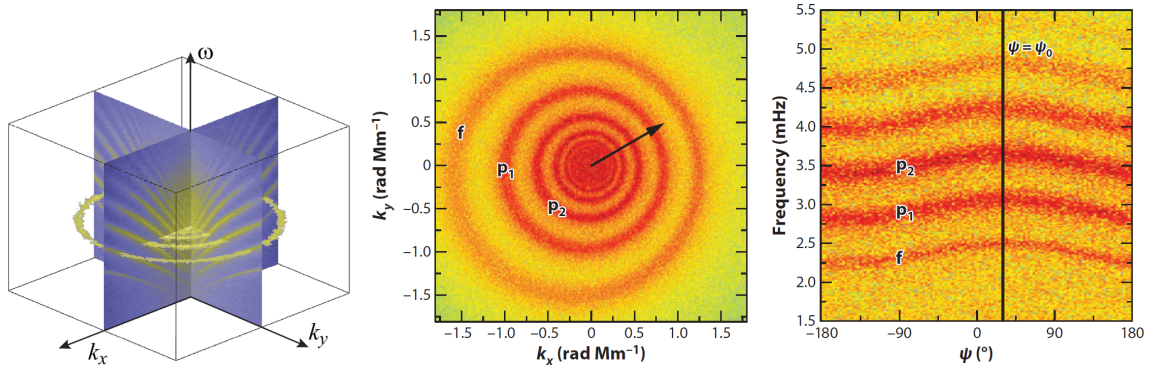
Figure 1.11: Ring-diagram analysis. Left: Power of Doppler velocity versus frequency and horizontal wavenumbers k_x and k_y. The trumpet-like structure is the 3D counterpart of Fig. 1.10. From Kosovichev (2012), with permission. Middle: Cut of 3D power at constant frequency. The power appears in the form of rings. A flow directed along 30° north of the prograde direction (indicated by the arrow) causes a Doppler shift and deforms the rings along that direction. From Gizon et al. (2010), with permission. Right: Cut of 3D power at constant k. The Doppler shift appears as a frequency shift along the direction indicated by the vertical black line. By fitting the individual ridges the horizontal velocities can be determined. From Gizon et al. (2010), with permission.

appears indeed as a change in the frequency (Fig. 1.11, right panel). Once the velocities have been determined for each mode, we can obtain the flows as a function of depth. This last step is referred to as an inversion, of which prominent sub-classes are the regularized least squares (RLS) and the optimally localized averages (OLA, Backus and Gilbert 1968, Pijpers and Thompson 1992) inversion. For this we can make use of the different depth sensitivity of the various modes. The sensitivity of ring-diagram kernels to local flows was studied by Birch et al. (2007). By combining the measurements (the ring fits) in a suitable way, it is possible to construct an averaging kernel, which focuses the sensitivity at a particular target depth, while at the same time it suppresses unwanted side lobes present in individual mode sensitivity kernels. Different combinations of the ring fits therefore allow to obtain the flows as a function of depth.

For HMI data, a ring-diagram pipeline (Bogart et al. 2011a,b) is in use. For this, Dopplergrams are mapped and tracked at the sidereal Carrington rate via the mtrack module, for various tile sizes (5, 15 or 30°). Local power spectra are computed and the ring-fitting is done either via (a) a 6-parameter model (Haber et al. 2000) of a Lorentzian line profile in frequency or (b) a more complex 13-parameter model (Basu et al. 1999), which includes parameters to describe line asymmetry. Contrary to the former ring fits, however, the latter are not inverted. The inversion step for the Haber et al. (2000)-based ring fits is performed via a 1D OLA algorithm (Basu et al. 1999, Basu and Antia 1999). The inverted flow velocities are available for the 15 and 30° tile sizes. For our analysis, we concentrate on the former tile size. The tile centers are separated by 7.5° in latitude and in longitude, with the longitude spacing increasing toward the poles to keep the physical tile area constant. Adjacent tiles overlap by 50 % with each other. The RDA flow velocities are then post-processed before data from RDA and local correlation tracking (Sect. 1.5.1) are commonly analyzed further. More details on this are given in Chap. 2.

31

Apart from the standard HMI ring-diagram data, there is another ring-diagram pipeline by Greer et al. (2014). One of the main differences is that the tiles are very densely spaced, i.e. tile centers are only 0.25° apart. Also, instead of fitting individual modes independently, multiple ridges in the power spectrum are fit together. This is called multi-ridge fitting. Nagashima et al. (2020) have made improvements to and fixed some bugs in the Greer et al. (2014) code and showed that the output ring fits are order-of-magnitude comparable with ring fits from the standard pipeline. Finally, contrary to the Bogart et al. (2011a) pipeline, the Greer et al. (2014) code employs a 3D inversion (including the horizontal dimensions). The effects of this kind of inversion on the output flow velocities are unknown and have not yet been analyzed in the literature.

1.6   Structure of the thesis

In Chap. 2, we investigate the latitudinal and radial dependence of Rossby wave eigenfunctions. The usage of two independent datasets allows us to compare the results for different methods to determine flows close to the surface of the Sun. Subsequently, in Chap. 3, we look at the power spectrum of large-scale deep convection and re-evaluate the large discrepancy between existing results. Finally, Chap. 4 gives a short discussion and extension of the results from the previous chapters and we try to illustrate how our observations might be part of a larger, common context. We will briefly address how Rossby waves appear in different observables and how solar activity may affect the energy spectrum of horizontal flows and we conclude the chapter with a short outlook.

2 Exploring the latitude and depth dependence of solar Rossby waves using ring-diagram analysis

2.1 Abstract

Global-scale equatorial Rossby waves have recently been unambiguously identified on the Sun. Like solar acoustic modes, Rossby waves are probes of the solar interior. We study the latitude and depth dependence of the Rossby wave eigenfunctions. By applying helioseismic ring-diagram analysis and granulation tracking to observations by HMI aboard SDO, we computed maps of the radial vorticity of flows in the upper solar convection zone (down to depths of more than 16 Mm). The horizontal sampling of the ring-diagram maps is approximately 90 Mm ($\sim$ 7.5°) and the temporal sampling is roughly 27 hr. We used a Fourier transform in longitude to separate the different azimuthal orders m in the range $3 \leq m \leq 15$. At each m we obtained the phase and amplitude of the Rossby waves as functions of depth using the helioseismic data. At each m we also measured the latitude dependence of the eigenfunctions by calculating the covariance between the equator and other latitudes. We conducted a study of the horizontal and radial dependences of the radial vorticity eigenfunctions. The horizontal eigenfunctions are complex. As observed previously, the real part peaks at the equator and switches sign near ±30°, thus the eigenfunctions show significant non-sectoral contributions. The imaginary part is smaller than the real part. The phase of the radial eigenfunctions varies by only ±5° over the top 15 Mm. The amplitude of the radial eigenfunctions decreases by about 10 % from the surface down to 8 Mm (the region in which ring-diagram analysis is most reliable, as seen by comparing with the rotation rate measured by global-mode seismology). The radial dependence of the radial vorticity eigenfunctions deduced from ring-diagram analysis is consistent with a power law down to 8 Mm and is unreliable at larger depths. However, the observations provide only weak constraints on the power-law exponents. For the real part, the latitude dependence of the eigenfunctions is consistent with previous work (using granulation tracking). The imaginary part is smaller than the real part but significantly nonzero.

2.2 Introduction

Recently, Löptien et al. (2018, hereafter LGBS18) discovered global-scale Rossby waves in maps of flows on the surface of the Sun. These waves are waves of radial vorticity that may exist in any rotating fluid body. Even though Rossby waves were predicted to exist in stars more than 40 years ago (Papaloizou and Pringle 1978, Saio 1982), solar Rossby waves were difficult to detect because of their small amplitudes ($\sim 1\,\mathrm{m\,s^{-1}}$) and long periods of several months. Solar Rossby waves contain almost as much vorticity as large-scale solar convection. The dispersion relation of solar Rossby waves is close to the standard relation for sectoral modes, $\omega = -2\Omega/(m + 1)$, where Ω is the rotation rate of a rigidly rotating star and m is the azimuthal order (Saio 1982). Rossby waves have a retrograde phase speed and a prograde group speed. In LGBS18, the authors also measured the horizontal eigenfunctions, which peak at the equator.

The detection of solar Rossby waves was confirmed by Liang et al. (2019, hereafter LGBD19) with time-distance helioseismology (Duvall et al. 1993) using data covering more than 20 years, obtained from the Solar and Heliospheric Observatory (SOHO) and from the Solar Dynamics Observatory (SDO; Pesnell et al. 2012). Alshehhi et al. (2019), in an effort to speed up ring-diagram analysis (RDA; Hill 1988) via machine learning, also saw global-scale Rossby waves. Hanasoge and Mandal (2019) and Mandal and Hanasoge (2020) provide another recent Rossby wave confirmation using a different technique of helioseismology known as normal-mode coupling (Woodard 1989, Hanasoge et al. 2017).

Knowledge about the latitude dependence of Rossby wave eigenfunctions is incomplete, as LGBS18 studied only their real parts. In a differentially rotating star, the horizontal eigenfunctions are not necessarily spherical harmonics (and may not even separate in latitude and depth). Also, little is known observationally about the depth dependence of the Rossby waves. It would be well worth distinguishing between the few existing theoretical models of the depth dependence (Provost et al. 1981, Smeyers et al. 1981, Saio 1982, Wolff and Blizard 1986).

In this paper, we explore the latitude dependence of the eigenfunctions, as well as the phase and amplitude of solar Rossby waves as functions of depth from the surface down to more than 16 Mm using helioseismology. We use observations from the Helioseismic and Magnetic Imager (HMI; Schou et al. 2012) on board SDO, processed with RDA. From these we attempt to measure the eigenfunctions of the Rossby waves in the solar interior. For comparison near the surface, we also use data from local correlation tracking of granulation (LCT; November and Simon 1988).

2.3 Data and methods

We used maps of the horizontal velocity, derived from two different techniques applied to SDO/HMI observations. The first dataset consists of LCT (granulation tracking) flow maps at the surface (Löptien et al. 2017) and covers almost six years from May 20, 2010 to March 30, 2016. The second dataset comprises RDA flow maps from the HMI ring-diagram pipeline (Bogart et al. 2011a,b; see also Bogart et al. 2015). For comparisons with LCT, we took a period as close to the LCT period as possible, i.e., May 19, 2010 to March 31, 2016, while for all other results we used a longer period of more than seven

years from May 19, 2010 to December 29, 2017; this corresponds to 102 Carrington rotations (CRs), i.e., CR 2097 - 2198.

2.3.1 Overview of LCT data

The LCT flow maps are obtained from and processed as described in Löptien et al. (2017). They are created by applying the Fourier LCT code (FLCT; Welsch et al. 2004, Fisher and Welsch 2008) to track the solar granulation in pairs of consecutive HMI intensity images. The image pairs are separated by 30 min. Several known systematic effects such as the shrinking-Sun effect (Lisle et al. 2004, Löptien et al. 2016) and effects related to the SDO orbit are present in the LCT maps. Therefore the maps are decomposed into Zernike polynomials, a basis of 2D orthogonal functions on the unit disk, and the time series of the coefficient amplitudes for the lowest few Zernike polynomials are filtered to remove frequencies of one day and one year (associated with the SDO orbit) as well as all harmonics up to the Nyquist frequency. The zero frequency is also removed. The filtered maps are then tracked at the sidereal Carrington rate and remapped onto an equi-spaced longitude-latitude grid with a step size of $0.4°$ in both directions.

2.3.2 Overview of ring-diagram data

The ring-diagram pipeline (Bogart et al. 2011a,b) takes HMI Dopplergrams as input and remaps them onto tiles spanning $182 \times 182\,\mathrm{Mm}$ (i.e., $15°$ each in latitude λ and longitude φ at the equator). The tiles overlap each other by roughly $50\,\%$ in each direction such that the tile borders fall onto the centers of adjacent tiles. Both the latitude and longitude sampling are half the tile size. The latitude grid is linear and includes the equator, while the longitude grid is also linear, but is latitude-dependent. Each tile is tracked for 1728 min (28.8 hr) at the sidereal Carrington rate. The temporal grid spacing is, on average, 1/24 of the synodic Carrington rotation period of 27.2753 days.

In the pipeline, for each tile a 3D local power spectrum is computed from the tracked Dopplergrams. The velocity fit parameters $U_{x,n\ell}$ (prograde) and $U_{y,n\ell}$ (northward) are extracted via a ring-fit algorithm (Haber et al. 2000) for different solar oscillation modes, which are indexed by their radial order n and angular degree ℓ. The flow velocities u_x and u_y are inferred for various target depths via a 1D optimally localized averages (OLA) inversion. The inversion results for the six-parameter fits of the $15°$ tiles sample a range of target depths from $0.97\,\mathrm{R}_\odot$ to $1\,\mathrm{R}_\odot$ (step size $0.001\,\mathrm{R}_\odot$), corresponding to a nonlinear grid of measurement depths (median of the ring-diagram averaging kernels) from $0.976\,\mathrm{R}_\odot$ to $1\,\mathrm{R}_\odot$. In this paper, the term depth always refers to measurement depth and not to target depth.

The inversion results are stored in the Joint Science Operations Center (JSOC) data series hmi.V_rdvflows_fd15_frame. However, up to inversion module rdvinv v.0.91, the inversion results depended on the input tile processing order due to an array initialization bug. This caused significantly lower velocity uncertainties for tiles near latitude $7.5°$ and Stonyhurst longitude $37.5°$, even when averaged over seven years, but also slightly affected the velocities. At the same disk locations the bug caused a correlation of u_x with the B_0 angle. Since rdvinv v.0.92 is officially only applied since March 2018, we re-inverted the entire dataset ourselves for the analysis shown in this work.

Apart from the array initialization bug, we found several other issues with the default HMI ring-diagram pipeline that have not yet been solved. Among these are under-regularization in the inversion for some individual tiles, leading to relatively narrow averaging kernels and anomalously high noise. Finally, the number of ring fits used for the inversion depends strongly on disk position. This may lead to systematic effects and additional noise.

The ring-diagram velocities u_x reported at a certain measurement depth r at the equator for an angular rotation rate $\Omega(r)$ are equal to $\Omega(r)R_\odot$ instead of the local velocity $\Omega(r)r$. Since we are interested in the latter, we multiplied u_x by $r/R_\odot$. By analogy, we also applied this factor to u_y and to all other latitudes. Additionally, the inversion does not account for the quantity $\beta_{n\ell}$, defined, for example, in Eq. 3.357 of Aerts et al. (2010). The quantity $\beta_{n\ell}$ is related to the effect of the Coriolis force on the mode frequency splitting. For uniform rotation in particular, at fixed m, $\beta_{n\ell}$ completely describes the effect of the rotation on the mode frequency splitting. Both issues are described in more detail in App. 2.6.1.

2.3.3 Post-processing of ring-diagram data

The ring-diagram data are organized in CRs, which undergo several processing steps, including the removal of systematic effects, an interpolation in longitude, an interpolation in time, and the removal of limb data.

Several systematic effects are present in the ring-diagram velocities, such as center-to-limb effects that depend on the disk position of the tile (Baldner and Schou 2012, Zhao et al. 2012). There are time-independent effects and systematics with a one-year period, which are probably related to the B_0 angle. To remove the systematics, we fit the time series at each position on the disk (in Stonyhurst coordinates) with sinusoids

$$
\begin{aligned}
u_x(t) &= a_x \sin(2\pi t/(1\text{ yr})) + b_x \cos(2\pi t/(1\text{ yr})) + c_x, \\
u_y(t) &= a_y \sin(2\pi t/(1\text{ yr})) + b_y \cos(2\pi t/(1\text{ yr})) + c_y,
\end{aligned}
\tag{2.1}
$$

and subtract the fits from the flow velocities. We used all available CRs to determine the fit parameters.

Because of the specific tile coordinate selection used by the ring-diagram pipeline (Bogart et al. 2011a), which seeks to optimally cover the visible disk, tile centers at different latitudes have Stonyhurst longitudes that are offset by multiples of 2.5° from each other. To obtain a latitude-independent longitude grid, we interpolated the flow maps in Stonyhurst longitude using splines (App. 2.6.2).

We also interpolated the ring-diagram flows in time similarly with splines to fill missing time steps due to instrumental issues (only 12 out of 2448 time steps), which cause a too low observational duty cycle ($\leq 70\,\%$). We interpolated the data in the Carrington reference frame so as to use always roughly the same physical locations on the Sun. This mixes different systematics, which are primarily dependent on disk position, but we should already have removed the dominant contributions at this stage. We interpolated every missing time step from roughly the same number of data points (all available time steps within the corresponding disk passage) using splines (App. 2.6.2).

The output uncertainties from the ring-diagram pipeline increase strongly toward the limb, in particular beyond an angular great-circle distance of roughly 65° to the crossing

of the central meridian with the equator ($\lambda = 0°, \varphi = 0°$). We thus only used ring-diagram data within 65° of ($\lambda = 0°, \varphi = 0°$).

2.3.4 From velocity maps to power spectra of radial vorticity

From this stage onward ring-diagram and LCT data are processed similarly. The processing steps include a shift to the equatorial rotation rate $\nu_{eq} = \Omega_{eq}/2\pi = 453.1\,\text{nHz}$, the subtraction of the longitude mean, the calculation of the radial vorticity, a spherical harmonic transform (SHT), and a Fourier transform of the SHT coefficient time series.

The flow maps are shifted from the tracking rate (sidereal Carrington rate) to the surface sidereal equatorial rotation rate of 453.1 nHz, an average of zonal flows inferred from global-mode analysis of SDO/HMI observations (Larson and Schou 2018). We shifted the LCT data in Fourier space via a time-dependent phase factor, applying the same convention for the Fourier transform as LGBS18. The ring-diagram data are first apodized by a raised cosine in angular great-circle distance to the point ($\lambda = 0°, \varphi = 0°$) to suppress near-limb data and are shifted via spline-interpolation (App. 2.6.2).

We next subtracted the longitude mean from the data to remove any remaining large-scale flows. Differential rotation and meridional circulation should have already been subtracted in the RDA or LCT post-processing, but any possible longitude-independent flows still in the data are removed in this step.

Subsequently, we calculated the radial vorticity (via second-order central finite differences) as follows:

$$\zeta(t, r, \lambda, \varphi) = -\frac{1}{r\cos\lambda}\frac{\partial(u_x(t, r, \lambda, \varphi)\cos\lambda)}{\partial\lambda} + \frac{1}{r\cos\lambda}\frac{\partial u_y(t, r, \lambda, \varphi)}{\partial\varphi}, \qquad (2.2)$$

where r is the measurement depth. We decomposed the resulting maps into spherical harmonics and performed a temporal Fourier transform of the spherical harmonic coefficients. Last, we calculated the power and the phase (where the phase range is the half-open interval $(-180°, 180°]$). The sign convention is such that waves with positive m and negative frequency ν have a retrograde phase speed.

If not stated otherwise, the terms power spectrum or Fourier transform used in this paper always refer to the power spectrum or Fourier transform of the radial vorticity. Similarly, we discuss eigenfunctions of radial vorticity. These eigenfunctions are not spherical harmonics, however (LGBS18). In particular, while the modes can be meaningfully indexed by m, the angular degree ℓ is not observable. Throughout the paper ℓ thus only refers to the projection of the Rossby wave modes onto the corresponding spherical harmonic and not to the Rossby wave eigenfunction itself. We also use the terms latitudinal and radial eigenfunctions, which assumes separability in the r and λ coordinates. This assumption is addressed in more detail in Sect. 2.5.

2.4 Results

2.4.1 Radial vorticity maps

Figure 2.1 shows example vorticity maps from LCT surface flows and from RDA flows near the surface, at intermediate, and at large depths (0.7, 9.9, and 16.5 Mm), averaged
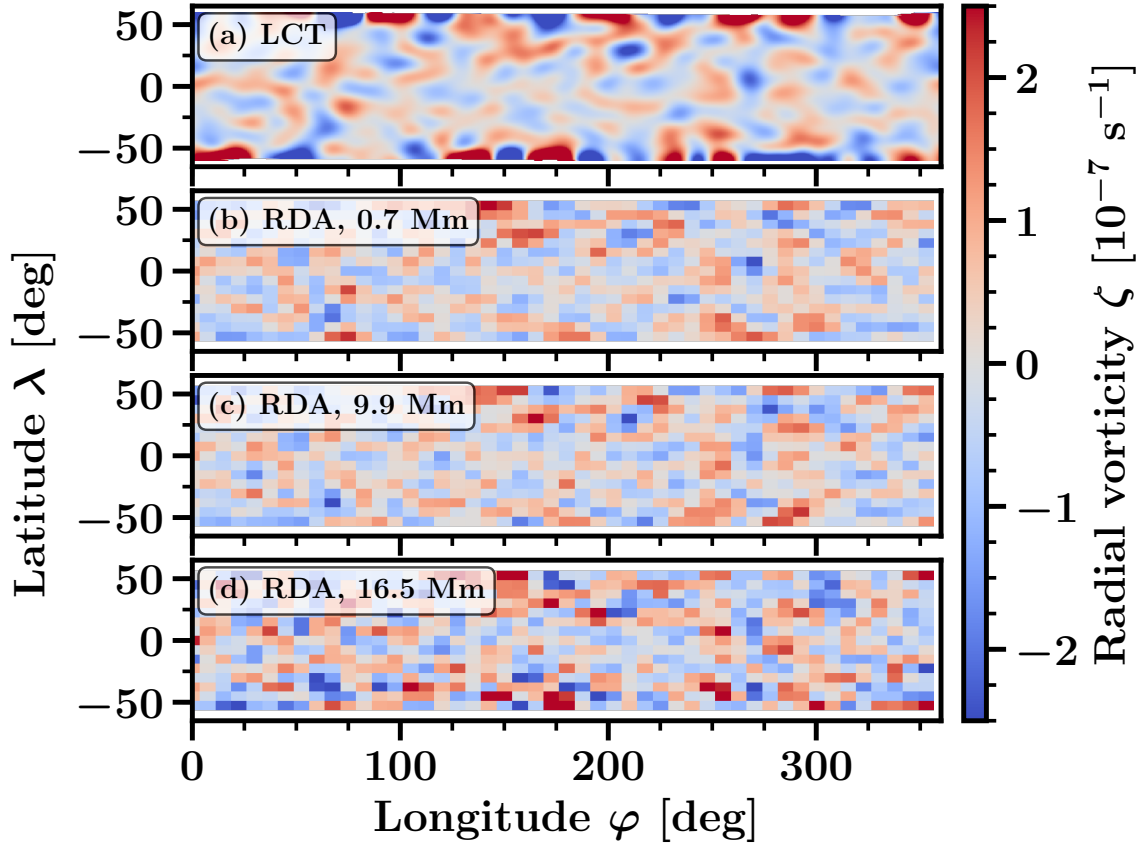
Figure 2.1: Radial vorticity maps from LCT at the surface and from RDA at depths 0.7, 9.9, and 16.5 Mm. The radial vorticity is averaged over one rotation (from May 20, 2010 to June 16, 2010). The LCT map is smoothed in latitude and longitude with a Gaussian filter ($\sigma = 6°$) to filter out small-scale convection.

over the first rotation in the dataset (May 20, 2010 to June 16, 2010). The LCT data have a much better horizontal resolution than the ring-diagram data and thus pick up small-scale convective contributions. To be able to compare LCT with RDA, we thus smooth the LCT vorticity with 1D Gaussian filters of width $\sigma = 6°$ both in latitude and longitude.

We do not expect perfect agreement of the two methods because of their different sensitivities to horizontal scales and to different depths. Nonetheless, the LCT map shows similar features as the near-surface (0.7 Mm) ring-diagram map. While large absolute radial vorticities are visible at high latitudes (beyond ±50°) in the LCT but not in the ring-diagram data, the vorticities near the equator agree. As a test, we interpolate the LCT data to the RDA grid using a 2D bicubic spline. The correlation coefficient between the interpolated LCT and the ring-diagram maps decreases with the latitude width of the strip of pixels considered and there is a steep decrease beyond ±45°. The correlation is 0.92 when including only equatorial pixels, 0.79 for pixels within ±45°, and 0.59 for all pixels, i.e., within ±52.5°. The noise increases strongly with depth (see lower panels of Fig. 2.1), but the main vorticity features are still visible.
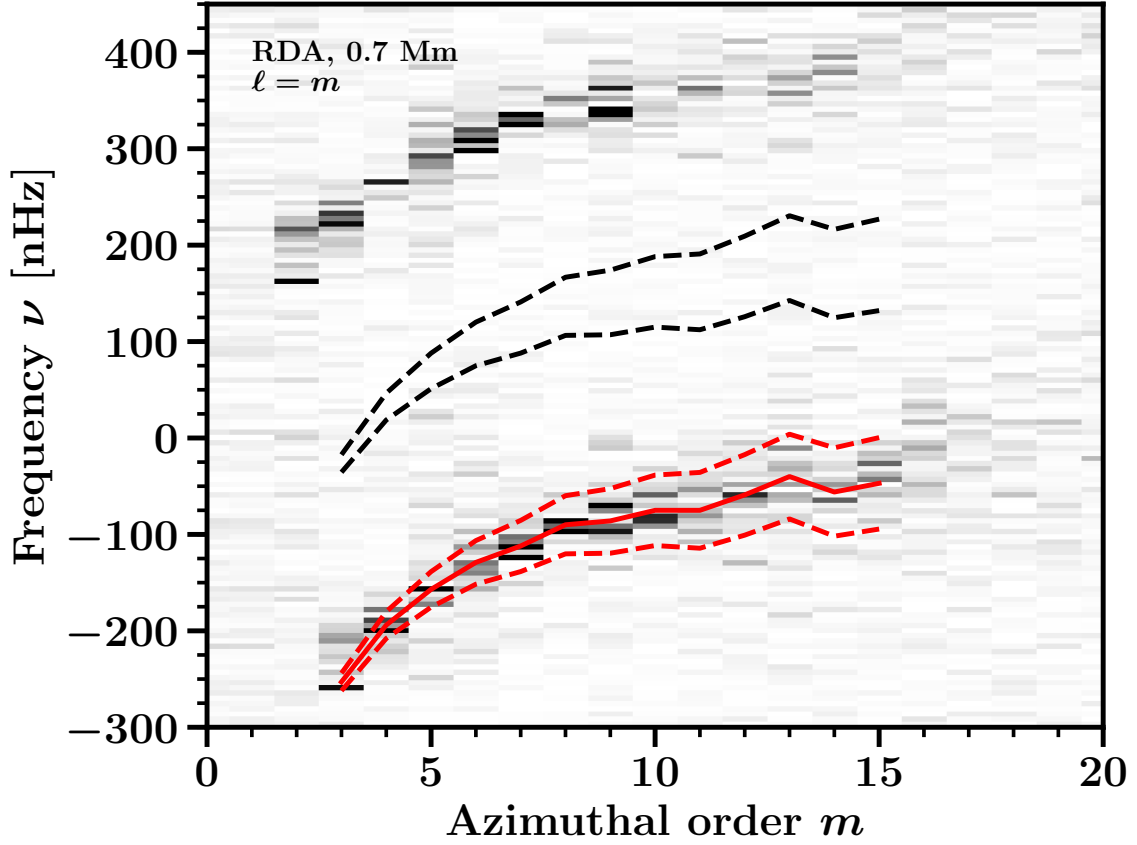
Figure 2.2: Sectoral power spectrum ($\ell = m$) of the radial vorticity for RDA data at depth 0.7 Mm. The solid red line indicates the Rossby wave frequencies from LGBD19 for $m = 3$ and from LGBS18 for $m \geq 4$. Frequency intervals for the Rossby wave region and the background region are indicated by the red and black dashed lines, respectively. The ridge of power at positive frequencies is due to the first side lobe of the window function. For better visibility of the Rossby waves at low m, the power is normalized at each m by the frequency average over $[-300, 100]$ nHz. The color scale is truncated at 50 % of the maximum value (black).

2.4.2 Power spectra of radial vorticity

Figure 2.2 shows the Rossby wave power of the $\ell = m$ component for the ring-diagram data near the surface (0.7 Mm) versus frequency and azimuthal order m (LGBS18 detected only the sectoral component of the Rossby waves). We divide the power, at each m, by the frequency average over $[-300, 100]$ nHz near the surface (0.7 Mm). The visible power ridge corresponds to the Rossby wave signal. The mode frequency increases with m roughly according to the textbook dispersion relation for sectoral waves, $\omega = -2\Omega_{\mathrm{eq}}/(m + 1)$, as seen earlier by LGBS18.

Besides the Rossby wave signal there are other ridges, that, at fixed $\Delta m = m - m'$, are shifted from the Rossby waves by roughly $\Delta m \left(\nu_{\mathrm{eq}} - 1/(1\,\mathrm{yr})\right)$, where $\nu_{\mathrm{eq}} - 1/(1\,\mathrm{yr}) \sim 421.4\,\mathrm{nHz}$. The main contribution to these side lobes comes from a temporal window function, which is introduced by solar rotation and not by time gaps; the time coverage is very good (see Sect. 2.3). This leads to side lobes of wave power from modes at m'

to modes at m. We only show the side lobes for $\Delta m = +1$, but we typically observe the side lobes above the noise between $\Delta m = -2$ and $\Delta m = +3$. In LGBD19, the authors use 21 years of time-distance data from a combined sample of observations from the Michelson Doppler Imager (MDI) on board SOHO and from SDO/HMI and they discuss the window function in detail.

Figure 2.3 shows the power versus frequency for different azimuthal orders m. We divide the power, at each m, by the frequency average of the $\ell = m = 8$ mode over $[-300, 100]$ nHz near the surface (0.7 Mm). The power decreases from 0.7 to 9.9 Mm, then increases toward 16.5 Mm, but the depth dependence is modest ($\leq 20\%$). We also see that the wave power decreases with m faster for RDA than for LCT owing to the different sensitivity kernels, as found by LGBS18. The $\ell = m = 3$ signal has a multi-peak structure and is thus difficult to measure. We do not observe Rossby waves for $\ell = m \leq 2$; the dash-dotted blue lines for $\ell = m = 1$ and $\ell = m = 2$ indicate the expected mode frequencies from the textbook dispersion relation.

The wave power side lobes due to the window function explain why the $\ell = m = 6$ side lobe in Fig. 2.2 even exceeds the main signal: the adjacent $\ell = m = 7$ mode has a higher relative power (see Fig. 2.3). Systematic effects that are fixed in the Stonyhurst reference frame can be easily misinterpreted as an $\ell = m = 1$ Rossby wave signal (see the LCT curve in Fig. 2.3), as their frequency (the rotation rate) is equal to the $\ell = m = 1$ Rossby wave frequency.

We assume that there is background power contributing to the observed power at the Rossby peak, but measuring its contribution directly at the peak is impossible. Since we are limited by the side lobes, we use a region halfway between the peak and the next side lobe, i.e., shifted from the peak by half the rotation rate. We checked that the shift direction does not matter much, so for the central background frequency, we use the Rossby wave frequencies ν_0^{ref} from LGBD19 and LGBS18 for $m = 3$ and $m \geq 4$, respectively, plus half the rotation frequency ν_{eq}. We use the full widths at half maximum $\gamma^{\mathrm{ref}} = \Gamma^{\mathrm{ref}}/2\pi$ from LGBD19 and LGBS18 for $m = 3$ and $m \geq 4$, respectively, and perform a least-squares second-order polynomial fit in m to obtain a smoothed linewidth γ_{smooth}. We use γ_{smooth} for the width of the peak and background frequency intervals. Thus our peak and background frequency intervals at each m are

$$
\begin{aligned}
\text{peak interval:} \quad & \nu_0^{\mathrm{ref}} & \pm\, \gamma_{\mathrm{smooth}}, \\
\text{background interval:} \quad & (\nu_0^{\mathrm{ref}} + \nu_{\mathrm{eq}}/2) & \pm\, \gamma_{\mathrm{smooth}}.
\end{aligned}
\tag{2.3}
$$

These definitions are used in the analysis of latitudinal eigenfunctions in Sect. 2.4.3.

In Fig. 2.2, we see that the peak interval (dashed red lines) typically captures the main wave power well. The 1D power spectra, however, reveal that the background interval (not shown in Fig. 2.3, but see dashed black lines in Fig. 2.2), however, is potentially contaminated by scattered signal power, for example, for $\ell = m = 5, 6$, and 14. To check how the frequency interval definition affects our results, we performed our analysis for several different peak and background intervals. The results are consistent, thus we adopt Eq. 2.3 for the peak and background intervals.

Unlike LGBS18, we see evidence for non-sectoral components of the Rossby waves. For $\ell = m + 2$ the 2D power spectrum shows, for $6 \leq m \leq 13$, a ridge of power at very similar frequencies to those of the $\ell = m$ Rossby waves seen in Fig. 2.2, apart from a higher relative noise level and side lobes. This is confirmed by the 1D cuts at fixed values
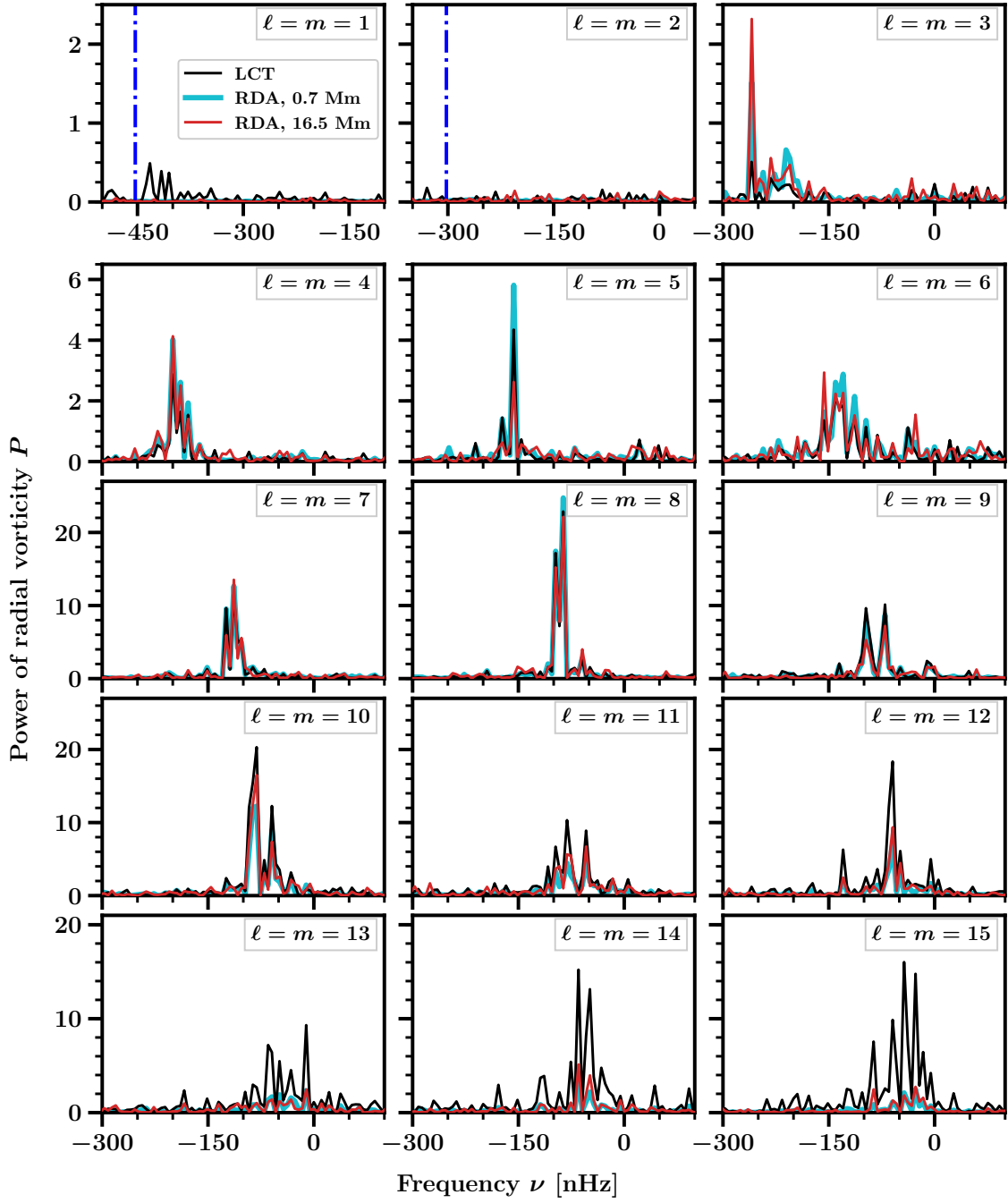
Figure 2.3: Sectoral power spectra ($\ell = m$) showing the Rossby wave power in the LCT data (black line) and the RDA data at depths 0.7 and 16.5 Mm (cyan and red lines). The power is normalized by the average of the $m = 8$ power in the range $[-300, 100]$ nHz. The dash-dotted vertical lines in the $m = 1$ and $m = 2$ panels indicate the frequencies $\omega = -2\Omega_{eq}/(m + 1)$. The frequency axes of the $m = 1$ and $m = 2$ panels are shifted with respect to the other panels.

of m. We do not see structure in the power spectra for $\ell = m + k$ other than for $k = 0$ and $k = 2$. In Sect. 2.4.3.3, we indeed show that the latitudinal eigenfunctions of Rossby waves are not sectoral spherical harmonic functions (in agreement with LGBS18).

2.4.3 Latitudinal eigenfunctions of Rossby waves

To estimate the latitudinal eigenfunctions, we first remove small-scale convection from the LCT maps via smoothing with a 6° Gaussian in latitude. Next we compute the Fourier transform of the radial vorticity maps $\zeta(t, r, \lambda, \varphi)$ from LCT and RDA in time and longitude as follows:

$$\hat{\zeta}_m(\nu, r, \lambda) = \sum_t \sum_\varphi \zeta(t, r, \lambda, \varphi) e^{i(2\pi\nu t - m\varphi)}. \tag{2.4}$$

The variables are discrete and take values at time steps $t_j = jT/N_t$ (integer $0 \le j < N_t$), longitudes $\varphi_k = 2\pi k/N_\varphi$ (integer $0 \le k < N_\varphi$), frequencies $\nu_s = s/T$ (integer s, with $-N_t/2 \le s \le N_t/2 - 1$ for even N_t), and azimuthal orders m (integer, with $-N_\varphi/2 \le m \le N_\varphi/2 - 1$ for even N_φ). In this case, T, N_t, and N_φ are the observation period and the number of data points in time and longitude, respectively. We apply a filter to select the Rossby waves one m at a time, i.e.,

$$\bar{\zeta}_m(\nu, r, \lambda) = \hat{\zeta}_m(\nu, r, \lambda) F_m(\nu). \tag{2.5}$$

The filter $F_m(\nu)$ is equal to one within the Rossby wave ridge and zero elsewhere. Since $\zeta(t, r, \lambda, \varphi)$ is real, the symmetry $\bar{\zeta}_m(\nu, r, \lambda) = \bar{\zeta}^*_{-m}(-\nu, r, \lambda)$ applies. We then transform back to time to obtain

$$\tilde{\zeta}_m(t, r, \lambda) = \frac{1}{N_t} \sum_\nu \bar{\zeta}_m(\nu, r, \lambda) e^{-i2\pi\nu t}. \tag{2.6}$$

In this way we obtain filtered time-latitude vorticity maps for every m. Because there is no symmetry $\bar{\zeta}_m(\nu, r, \lambda) = \bar{\zeta}^*_m(-\nu, r, \lambda)$, the filtered vorticity maps $\tilde{\zeta}_m(t, r, \lambda)$ are in general complex.

LGBS18 do a similar analysis for LCT data, in particular for rotation-averaged maps and filtering within ± 30 nHz around the central mode frequencies. We do the entire latitudinal eigenfunction analysis for LCT and RDA, for full time-resolution maps and maps averaged in time within individual solar rotations, and for a ± 27 nHz (five frequency pixels) and a linewidth filter (Eq. 2.3) around the central mode frequencies. The different time-resolution and filtering cases yield consistent results; we thus show only the outcome for the full time-resolution and linewidth filtering. However, LGBS18 take the real part of the complex $\tilde{\zeta}_m(t, r, \lambda)$. This is equivalent to assuming that the phase of the eigenfunction is independent of latitude. We address the implications of this in Sect. 2.4.3.3 in more detail.

To estimate uncertainties for all results in this paper, we split the data into equal-size time intervals, apply our analysis to each chunk, and calculate the standard deviation over the results (for complex quantities separately for the real and imaginary part). Appendix 2.6.3 gives more details on error estimation and validation. Because of the small number of chunks, low-number statistics are an issue and the reported error bars are relatively uncertain.

For the sake of clarity, for the simple case of a single m Rossby wave with a frequency ν_m and an eigenfunction $C_m(r, \lambda)$, the vorticity field for that mode, $\zeta_m(t, r, \lambda, \varphi)$, would be given by

$$\zeta_m(t, r, \lambda, \varphi) \propto \mathrm{Re}\left(C_m(r, \lambda)e^{i(m\varphi - 2\pi\nu_m t)}\right). \tag{2.7}$$

We apply two different methods to obtain the eigenfunctions $C_m(r, \lambda)$ near the surface, the covariance method (Sect. 2.4.3.1), and the SVD method (Sect. 2.4.3.2). The former is used also by LGBS18.

2.4.3.1 Covariance

We calculate, at each m, the temporal covariance of the vorticity $\tilde{\zeta}$ between the equator near the surface (target depth $R = R_\odot - 0.7\,\mathrm{Mm}$ for RDA) and all other latitudes and depths, normalized by the variance at the equator near the surface

$$C_m(r, \lambda) = \frac{\langle \tilde{\zeta}'_m(t, r, \lambda)\tilde{\zeta}'^*_m(t, r = R, \lambda = 0°)\rangle_t}{\langle |\tilde{\zeta}'_m(t, r = R, \lambda = 0°)|^2\rangle_t}, \tag{2.8}$$

where the angle brackets $\langle\cdot\rangle_t$ denote a temporal average and $\tilde{\zeta}' = \tilde{\zeta} - \langle\tilde{\zeta}\rangle_t$ is the centered vorticity. The function $C_m(r, \lambda)$ is complex-valued since $\tilde{\zeta}_m$ is in general complex. By construction $C_m(r = R, \lambda = 0°)$ is unity. Appendix 2.6.4 shows that C_m can also be obtained by a linear fit to the vorticity. The same covariance can be computed with the LCT data.

2.4.3.2 Singular value decomposition

We present a second, new method to obtain latitudinal eigenfunctions. We want to separate the filtered vorticity at each azimuthal order m and depth r, i.e., a 2D matrix, into a latitude and a time dependence, i.e.,

$$\tilde{\zeta}_m(t, r, \lambda) \propto f_m(t)C_m(r, \lambda). \tag{2.9}$$

Applying a singular value decomposition (SVD), we can decompose the vorticity as

$$\tilde{\zeta}_m(t, r, \lambda) = \sum_{j=0}^{k-1} s_{(r,m),j}U_{(r,m),j}(t)V_{(r,m),j}(\lambda), \tag{2.10}$$

where $s_{(r,m),j}$ is the singular value of index j with left and right singular vectors $U_{(r,m),j}$ and $V_{(r,m),j}$ and k is the minimum between the number of grid points in time and latitude. The square of $s_{(r,m),j}$ measures the variance captured by its singular vectors. By convention the singular values are sorted in descending order, thus the first singular vector contains more variance than any other individual singular vector.

Assuming that there is only one nonzero singular value, $s_{(r,m),0}$, the SVD gives the desired decomposition of the vorticity into one time and one latitude function. **This assumption is valid if there is only one excited mode in our filtered vorticity maps.** Our observations indeed have one clearly dominant singular value: **The first singular value, $s_{(r,m),0}$, is typically two to three times larger than the second singular value, $s_{(r,m),1}$. In addition, by looking at the latitude singular vectors from different time chunks,**

we noticed that the first singular vector, $V_{(r,m),0}$, always had a similar shape, whereas the second singular vector, $V_{(r,m),1}$, had different shapes for different chunks. This is another indication that there is only one significant mode.

Given that the noise at high latitudes increases steeply, we crop our vorticity maps for the SVD to latitudes within $\pm50°$ of the equator. Also, the SVD does not account for the varying noise of the remaining latitudes. To ensure that latitudes with larger uncertainties are given less weight, we filter the original vorticity maps once more in Fourier space for the noise, calculate the temporal standard deviation σ_m of the noise-filtered maps, and compute $\tilde{\zeta}_{nw,m}(t,r,\lambda) = \tilde{\zeta}_m(t,r,\lambda)/\sigma_m(r,\lambda)$. We filter for the noise by taking either all frequencies except for five pixels around the peak or all frequencies within the background interval (see Eq. 2.3). The two different filters give consistent results. At each m, the SVD is performed on the weighted maps $\tilde{\zeta}_{nw,m}$ and the resulting latitude vectors are multiplied by σ_m again to undo the weighting. We apply the weighting only to LCT, since the ring-diagram data are already apodized (see Sect. 2.3). We select the first latitude singular vector near the surface and normalize it by its value at the equator.

2.4.3.3   Results for the latitudinal eigenfunctions

Figures 2.4 and 2.5 show the real and imaginary parts of the horizontal eigenfunctions of Rossby waves versus latitude for different m. The real part is consistent with the findings from LGBS18. The imaginary part, however, was not discussed by LGBS18.

In the current paper, we find that the LCT and the RDA results are mostly consistent for the near-surface layers. Also, almost all m show agreement between the covariance and SVD results. This in particular holds for the modes with the largest amplitudes, i.e., for $7 \leq m \leq 10$. On the other hand, the modes $m = 4$ and to a lesser extent $m = 15$, where Rossby wave measurements become difficult, display larger errors but nonetheless consistent results. The $m = 3$ results for the different techniques disagree and are noisy. The $m = 5$ and $m = 6$ results for the real part differ slightly between the covariance and SVD methods. While the covariance yields a real part of the eigenfunction quite similar to those of other modes, the SVD-based results show maxima around latitudes of ±10-$15°$. Apparently, there the SVD picks up some variance that is uncorrelated with the equator. It is unclear whether it is just noise, or a real signal of a different kind of latitudinal eigenfunctions.

The eigenfunction shape is similar for different modes. The real part decreases away from the equator, flips sign, and approaches zero after going through a local minimum. The imaginary part is much noisier than the real part, as indicated by the error estimates. For most m, it is close to zero and flat near the equator, but reaches minima at high latitudes. The latitude of the minima appears to move toward the equator with increasing m.

As can be seen from, for example, the red curves in Fig. 2.5, the imaginary part appears to be mostly positive for $3 \leq m \leq 6$. For $7 \leq m \leq 9$ the sign of the imaginary part is unclear. For $10 \leq m \leq 15$, the imaginary part is predominantly negative. The presence of an imaginary part induces a phase for the latitudinal eigenfunctions that can be interpreted as a latitude-dependent shift of the sinusoid in longitude. A positive sign of the imaginary part means that the horizontal eigenfunctions at high latitudes are leading in the retrograde direction with respect to the equator. Conversely, a negative sign would indicate that the

44

Figure 2.4: Real part of $C_m(\lambda)$ for different azimuthal orders m and four different methods (see legend in panel $m = 4$). The shaded areas indicate the 1σ error estimates.
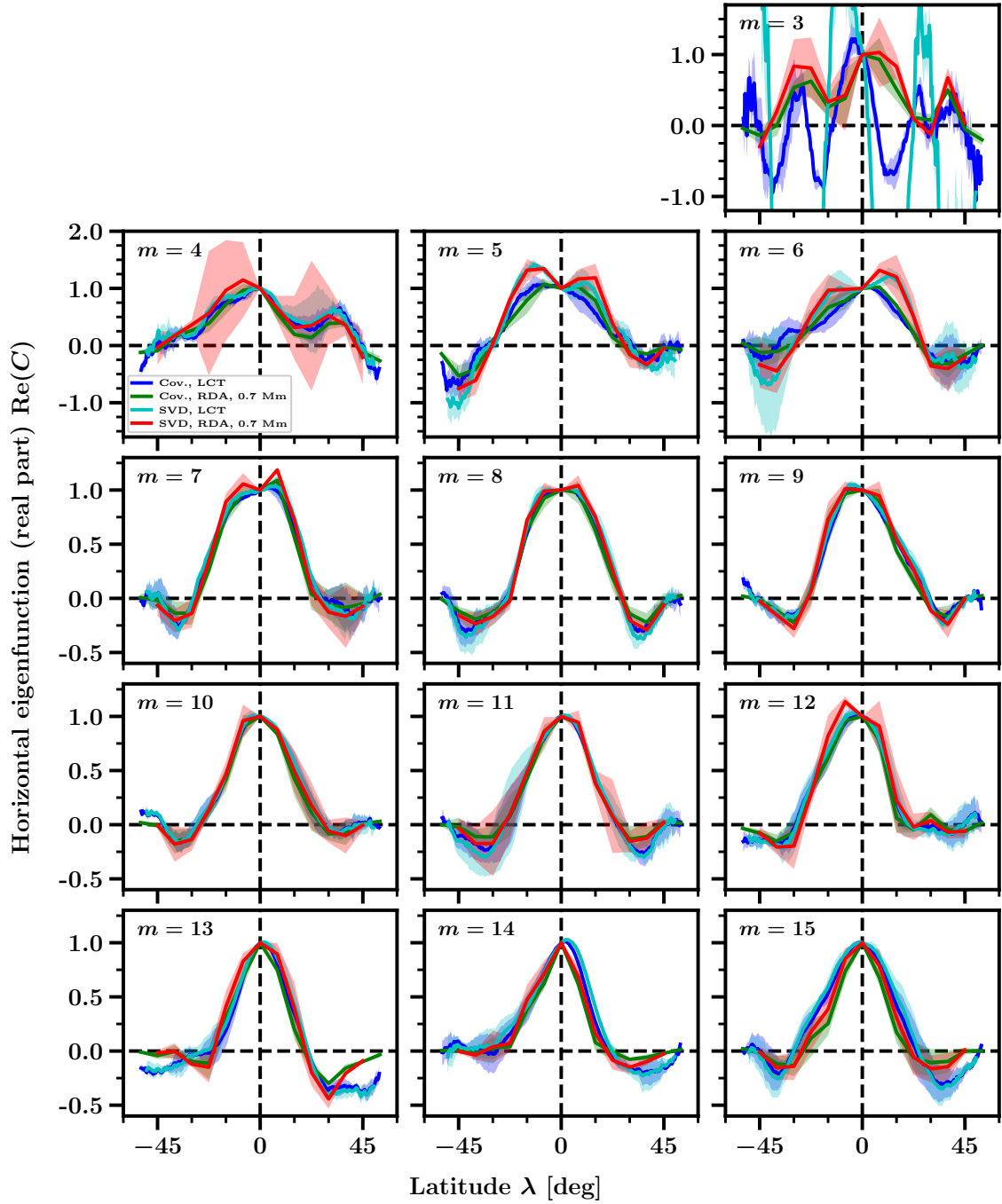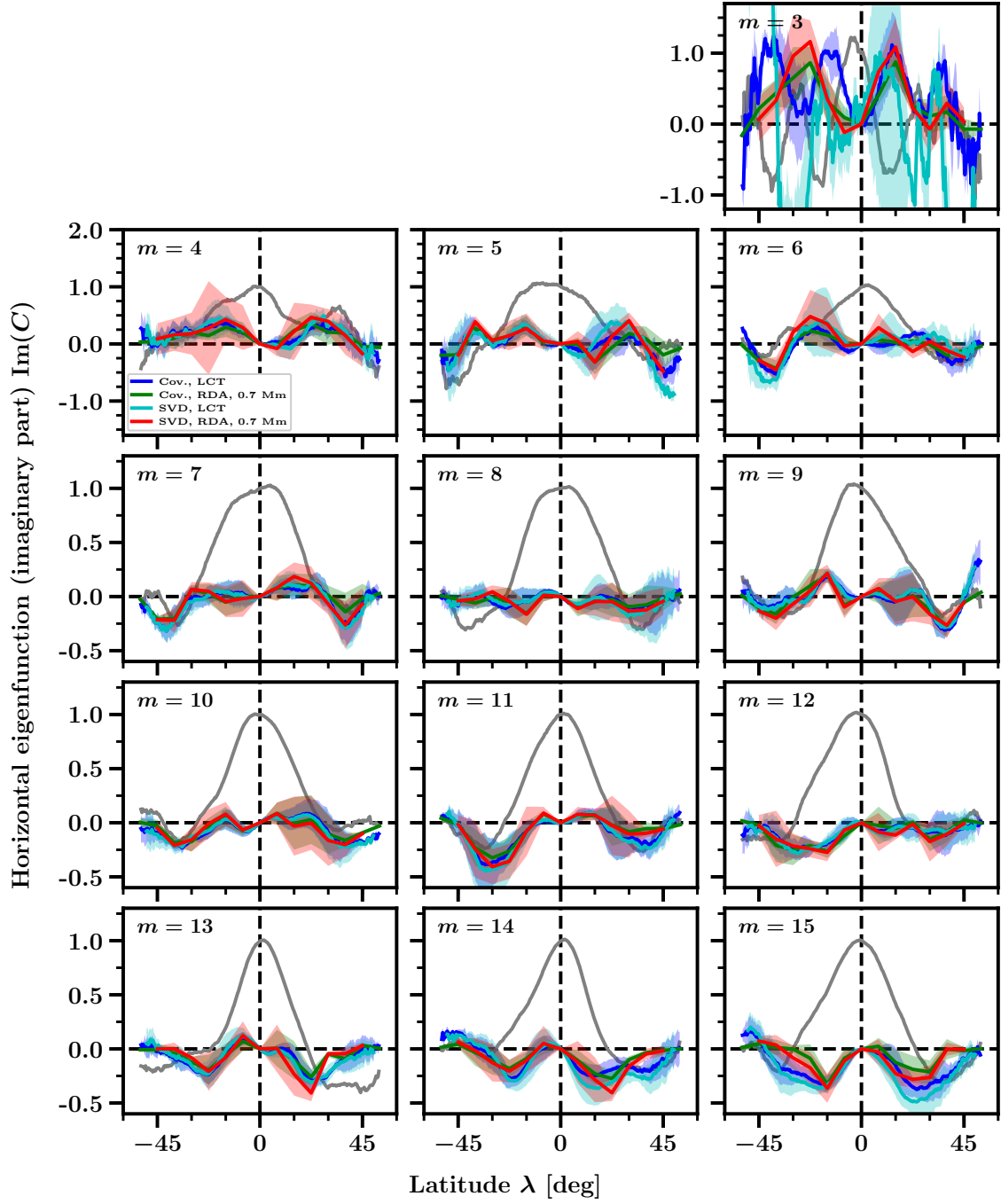
Figure 2.5: Imaginary part of $C_m(\lambda)$ for different azimuthal orders m and four different methods (see legend in panel $m = 4$). The shaded areas indicate the 1σ error estimates. For comparison, the solid gray curves show the real part of C_m for the LCT covariance-based data. The plotting ranges are the same as in Fig. 2.4.
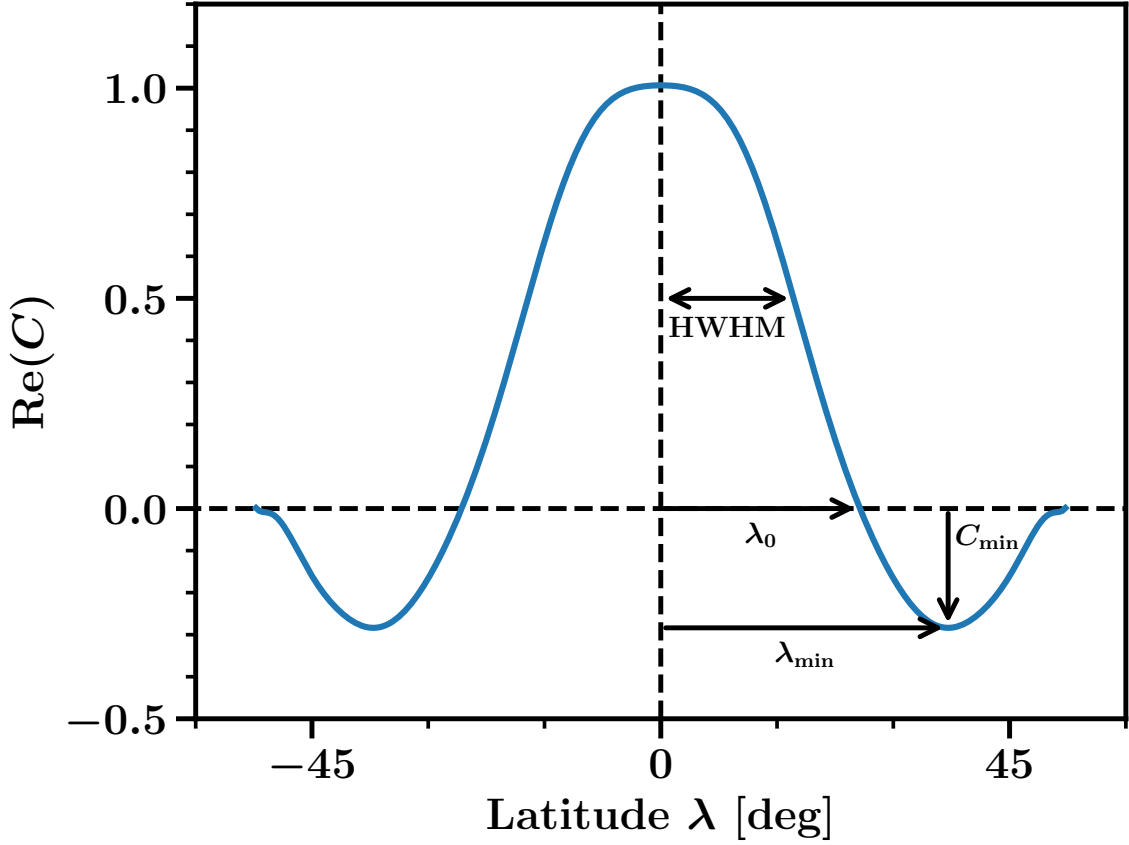
Figure 2.6: Schematic description of the real part of $C_m(\lambda)$ for a given m. The various parameters that describe the curve are the HWHM, the latitude at zero crossing (λ_0), the latitude at minimum (λ_{min}), and the minimum value (C_{min}).

eigenfunctions at high latitudes are trailing with respect to the equator. This may provide important constraints on the theory of latitudinal eigenfunctions of Rossby waves.

Figure 2.4 suggests that the real part of the eigenfunctions is more confined to low latitudes for higher values of m. We study the m-dependence of several characteristic parameters illustrated in Fig. 2.6, i.e., the width at an eigenfunction real part of $\mathrm{Re}(C) = 0.5$ (a half width at half maximum; HWHM), the latitude of the eigenfunction real part sign reversal, λ_0, and the latitude and value of the minimum, λ_{min} and C_{min}, respectively. To reduce the noise level we derive the eigenfunctions from maps symmetrized in latitude before measuring these parameters.

To obtain the latitude widths at $\mathrm{Re}(C) = 0.5$ and $\mathrm{Re}(C) = 0$, we linearly fit the two points closest to these $\mathrm{Re}(C)$ values. The latitude and value of the minimum are obtained by quadratically fitting three points around the minimum derived without fitting. We do this to avoid oscillating RDA results due to the coarse $7.5°$ latitude sampling. For LCT, the effects of fitting the minimum (or not) are minimal. There are no results for $m = 3$ and $m = 4$ because of the poor quality and different shape of the eigenfunctions. We already stated the difficulties in characterizing these modes. As described at the beginning of Sect. 2.4.3 and in App. 2.6.3, to derive uncertainties, we compute the standard deviation over the results for different time chunks, separately for the real and the imaginary part.

Table 2.1 shows how these parameters, measured for the LCT data from the covariance

Table 2.1: Parameters of the real part of $C_m(\lambda)$ for the LCT covariance-based data; see Fig. 2.6. The parameters for $m = 3$ and $m = 4$ are not given owing to the large uncertainties.

m	HWHM [deg]	λ_0 [deg]	$\lambda_{\min}$ [deg]	$C_{\min}$
5	20.7 ± 2.8	31.5 ± 4.0	46.5 ± 3.6	-0.38 ± 0.17
6	16.1 ± 2.8	31.5 ± 2.2	44.0 ± 3.3	-0.24 ± 0.13
7	18.7 ± 0.4	28.7 ± 1.2	37.0 ± 4.2	-0.17 ± 0.07
8	17.1 ± 0.8	25.8 ± 0.2	36.5 ± 1.8	-0.28 ± 0.06
9	16.0 ± 1.3	27.4 ± 1.4	35.2 ± 0.4	-0.17 ± 0.02
10	14.7 ± 1.1	27.8 ± 1.6	34.5 ± 2.1	-0.11 ± 0.06
11	14.3 ± 1.2	24.8 ± 2.3	34.9 ± 2.4	-0.25 ± 0.09
12	13.8 ± 1.4	28.9 ± 1.0	39.6 ± 1.8	-0.14 ± 0.01
13	11.3 ± 2.0	21.1 ± 1.3	47.1 ± 2.2	-0.31 ± 0.02
14	12.0 ± 0.8	24.6 ± 9.0	35.5 ± 5.5	-0.11 ± 0.07
15	14.7 ± 2.0	27.0 ± 3.1	37.7 ± 2.0	-0.26 ± 0.04

method, depend on m. Although not given in the table, we also measure the parameters for the RDA and the SVD results. We thus also discuss the m-dependence for those measurements; this dependence is mostly consistent with that of the LCT covariance-based parameters.

The latitude width at $\text{Re}(C) = 0.5$ indeed decreases with m, quasi-linearly between $m = 7$ and $m = 13$. The slope is roughly $-1°$ per m. The decrease might flatten off at high m, but this could also be caused by noise. We observe slightly different latitude widths between the covariance and SVD eigenfunctions at low m for $\text{Re}(C) = 0.5$, but similar widths at $\text{Re}(C) = 0$. Toward higher m, λ_0 is consistent with a flat profile, until around $m = 13$ the eigenfunction widths become smaller. The latitude of the minimum, $\lambda_{\min}$, shows an m-(in)dependence similar to λ_0. There is a strong discrepancy for $m = 13$ between LCT and RDA, indicating that this mode is not trivial to characterize. This could be caused by noise. To some extent we could already see this in the power spectrum in Fig. 2.3, where the $m = 13$ linewidth is large compared to all other m. The error on $\lambda_{\min}$ might be underestimated here, since as seen in the asymmetric eigenfunctions in Fig. 2.4 the minimum of the LCT data is more poorly defined for $m = 13$ than for other modes. Finally, the value of the minimum, $C_{\min}$, is different between the different analysis methods at $m = 5$ and $m = 6$, as seen before. Otherwise, it is quasi m-independent and has at most a very mild increase with m from $m = 7$ onward, which is likely covered by noise, however.

As mentioned before, the latitudinal eigenfunctions appear to have two nodes (zero crossings) at latitudes $\pm\lambda_0$. This in combination with Fig. 2.2 and the subsequent discussion indicates that the eigenfunctions have significant contributions from $\ell = m$ and $\ell = m + 2$ components. To quantify these contributions, we project the symmetric eigenfunctions $C_m(\lambda)$ onto associated Legendre polynomials $P_\ell^m(\sin \lambda)$, to obtain the coefficients

$$c_{\ell m} = \frac{\pi}{2N_\lambda} \sum_\lambda C_m(r = R, \lambda) P_\ell^m(\sin \lambda) \cos \lambda. \qquad (2.11)$$

The sum goes over all latitudes $\lambda = k\pi/N_\lambda$ (integer $-N_\lambda/2 \leq k < N_\lambda/2$), where N_λ is the number of data points in latitude. The $P_\ell^m(\sin\lambda)$ are normalized such that

$$\pi/N_\lambda \sum_\lambda (P_\ell^m(\sin\lambda))^2 \cos\lambda = 2. \qquad (2.12)$$

The associated Legendre polynomials used in the decomposition are not orthogonal over the limited observed latitude range. However, we do not expect this to be a problem since we see later in this section that the near-sectoral associated Legendre polynomials, whose amplitude is concentrated toward the equator, are the dominant contributions to the latitudinal eigenfunctions. Because of the symmetry of the eigenfunctions, only $c_{\ell m}$ with even $\ell - m \geq 0$ are nonzero. We find that the real and the imaginary parts of the eigenfunctions for almost all m can be approximated well (within 1σ) when using only the contributions from $c_{\ell m}$ for $m \leq \ell \leq m + 6$, except for $m = 3$, which is very noisy. The approximation also does not work well at the high latitudes (beyond $\pm 40°$) for the real part (for some modes) and at the near-equatorial latitudes for the imaginary part (for almost all modes).

Table 2.2 shows the coefficients $c_{\ell m}$ for $m \leq \ell \leq m + 6$ for the LCT covariance-based latitudinal eigenfunctions. As usual the uncertainties are calculated from the standard deviation over the coefficients for different time chunks (App. 2.6.3), separately for the real and the imaginary part. The real part of the eigenfunctions is clearly dominated by the $\ell = m$ component. The contribution from the $\ell = m + 2$ component is significant as well and has a relative strength of 30-50 %. This is consistent with the observations from the 2D and 1D power spectra in Sect. 2.4.2. The real part of the c_{mm} and $c_{m+2,m}$ each depend weakly on m. The real part of several of the coefficients with larger ℓ is insignificant. The imaginary part, on the other hand, has significant, dominant contributions at $\ell = m + 4$ for $m \leq 10$ and at $\ell = m + 2$ for $m \geq 11$, whereas the $\ell = m$ and $\ell = m + 6$ components are often insignificant. The term insignificant refers to an absolute value of $c_{\ell m}$ of less than 1σ. Nonetheless, independent of the estimated error bars, 11 out of 12 modes within $4 \leq m \leq 15$ have the same sign for $c_{m+4,m}$, suggesting that the $\ell = m + 4$ contribution to the real part is significant, despite being within 1σ from zero. A similar argument holds for the imaginary part of the latitude dependence of the Rossby wave eigenfunctions.

For the latitudinal eigenfunctions of Rossby waves there are so far only a few theoretical studies such as Lee and Saio (1997) and Townsend (2003). These studies typically gave either analytic (asymptotic) expressions and/or numeric calculations, but the former expressions do not agree well with the latter calculations for Rossby waves (Townsend 2003). Although both studies indicate that the latitudinal eigenfunctions are not concentrated near the equator, we cannot sensibly compare their findings to our measurements. In particular these models assume a uniform rotation rate. Also these authors used the traditional approximation, i.e., they neglected the horizontal component of the rotation vector. This approximation requires the squared Brunt-Väisälä frequency N^2 to be much higher than both the squared oscillation frequency ω^2 and the squared rotation rate Ω^2. The validity of the traditional approximation thus has to be critically examined within the convection zone of the Sun.

Table 2.2: Coefficients $c_{\ell m}$ for the LCT covariance-based data. Each bracketed pair of numbers refers to the real and imaginary parts of $c_{\ell m}$. The numbers in italics are not significantly different from zero (zero within 1σ).

m	c_{mm}	$c_{m+2,m}$	$c_{m+4,m}$	$c_{m+6,m}$
3	(+0.026, +0.417) ± (0.018, 0.105)	(−0.155, +0.089) ± (0.032, 0.103)	(+0.118, −0.108) ± (0.075, 0.074)	(−0.117, +0.004) ± (0.015, 0.029)
4	(+0.457, +0.136) ± (0.016, 0.060)	(−0.097, +0.061) ± (0.027, 0.017)	(−0.010, −0.066) ± (0.036, 0.030)	(−0.071, +0.019) ± (0.014, 0.026)
5	(+0.478, +0.037) ± (0.031, 0.070)	(−0.263, −0.021) ± (0.086, 0.067)	(−0.059, −0.106) ± (0.052, 0.112)	(+0.041, −0.011) ± (0.045, 0.040)
6	(+0.411, +0.021) ± (0.055, 0.019)	(−0.202, −0.050) ± (0.025, 0.057)	(−0.005, −0.118) ± (0.040, 0.032)	(−0.006, +0.059) ± (0.007, 0.018)
7	(+0.473, +0.026) ± (0.024, 0.028)	(−0.183, −0.055) ± (0.015, 0.024)	(−0.012, −0.073) ± (0.012, 0.023)	(+0.043, +0.018) ± (0.006, 0.012)
8	(+0.441, −0.013) ± (0.015, 0.022)	(−0.231, −0.038) ± (0.021, 0.027)	(−0.047, −0.009) ± (0.031, 0.068)	(+0.038, +0.001) ± (0.017, 0.027)
9	(+0.434, +0.028) ± (0.013, 0.042)	(−0.162, −0.032) ± (0.023, 0.014)	(−0.010, −0.053) ± (0.018, 0.044)	(+0.025, +0.022) ± (0.005, 0.030)
10	(+0.423, +0.008) ± (0.024, 0.012)	(−0.139, −0.057) ± (0.017, 0.041)	(+0.011, −0.076) ± (0.034, 0.028)	(+0.020, −0.013) ± (0.001, 0.010)
11	(+0.400, −0.010) ± (0.027, 0.003)	(−0.173, −0.117) ± (0.049, 0.043)	(−0.043, −0.064) ± (0.027, 0.058)	(+0.002, +0.024) ± (0.018, 0.024)
12	(+0.419, −0.040) ± (0.029, 0.023)	(−0.117, −0.078) ± (0.006, 0.011)	(−0.016, −0.021) ± (0.010, 0.032)	(−0.027, −0.007) ± (0.042, 0.030)
13	(+0.345, −0.016) ± (0.036, 0.023)	(−0.195, −0.112) ± (0.018, 0.020)	(−0.048, −0.028) ± (0.029, 0.011)	(−0.071, +0.026) ± (0.013, 0.023)
14	(+0.380, −0.057) ± (0.026, 0.025)	(−0.128, −0.102) ± (0.038, 0.044)	(−0.007, +0.006) ± (0.027, 0.022)	(−0.019, +0.001) ± (0.015, 0.017)
15	(+0.431, −0.074) ± (0.017, 0.013)	(−0.085, −0.151) ± (0.054, 0.029)	(−0.072, −0.041) ± (0.020, 0.057)	(−0.053, −0.012) ± (0.036, 0.020)

2.4.4 Radial eigenfunctions of Rossby waves

2.4.4.1 Depth-dependent ring-diagram systematics

To study the Rossby wave depth dependence, we must check to which depths RDA is reliable. For this we compare the solar rotation profile from ring-diagram velocities with the results from SDO/HMI global modes from the JSOC data series hmi.V_sht_2drls (Larson and Schou 2018). The global modes have a 72-day time sampling from April 30, 2010 to June 4, 2017, a 1.875° latitude sampling, and a nonlinear depth grid with many more points near the surface than at larger depths. Global modes are expected to give a precise and accurate solar rotation profile. We interpolate the global mode results to the ring-diagram latitude-depth grid via 2D bicubic splines, which is reasonable because the global-mode inversions do not vary on scales of their original grid; we then average the 72-day chunks over time. The chunk scatter of the rotation rate is used to estimate the uncertainty. We divide the ring-diagram data into five intervals of length 480 time steps (20 rotations), average the chunks over time and estimate the error from the scatter, convert the velocities into rotation rates, and add the sidereal Carrington rate to correct for the ring-diagram tracking.

Figure 2.7 shows the equatorial rotation rate versus depth from global modes and ring-diagram velocities, both averaged over longitude and at Stonyhurst longitudes of ±52.5° (the outermost longitudes in our vorticity maps). The global modes yield a smooth profile with extremely small errors. The ring-diagram data show a small offset at small depths, but, more importantly, inconsistency with the global modes at large depths. Of course, it is difficult to judge how well the results should agree because of the different kernels of the datasets and thus different depth (and latitude) sensitivities. The −52.5° longitude curve has a small local maximum around 8 Mm. For longitudes even further east (not shown), the rotation rate has an even stronger excess (a bump) there.

The most worrisome point is the disagreement between different ring-diagram longitudes themselves and also with the longitude average, below roughly 8 Mm (indicated by the left dashed line in Fig. 2.7). Because we averaged the data over more than seven years, any short-lived flows and even longer-lived structures should be filtered away and the longitude gradient from east to west should thus not exist. This points to a deeper problem with the ring fits and the pipeline processing that generated these fits. The presence of systematic effects in HMI ring-diagram data has also been extensively discussed in Komm et al. (2015).

Finally, we note that Fig. 2.7 is affected by an issue related to the ring-diagram inversion, since the inversion does not account for the quantity $\beta_{n\ell}$. A discussion of this issue and a brief check of the magnitude of the effect is given in App. 2.6.1. The latter showed that the main effect is a depth-independent underestimation of the ring-diagram velocities by 1-2 m s^{-1} or equivalently of the rotation rate by less than 0.5 nHz. This does not affect our main conclusions. The small, but significant difference between the rotation rates from global modes and ring diagrams cannot be caused by the $\beta_{n\ell}$ issue (it has the wrong sign), but may possibly instead be due to different averaging kernel widths, systematics, or other unknown effects.
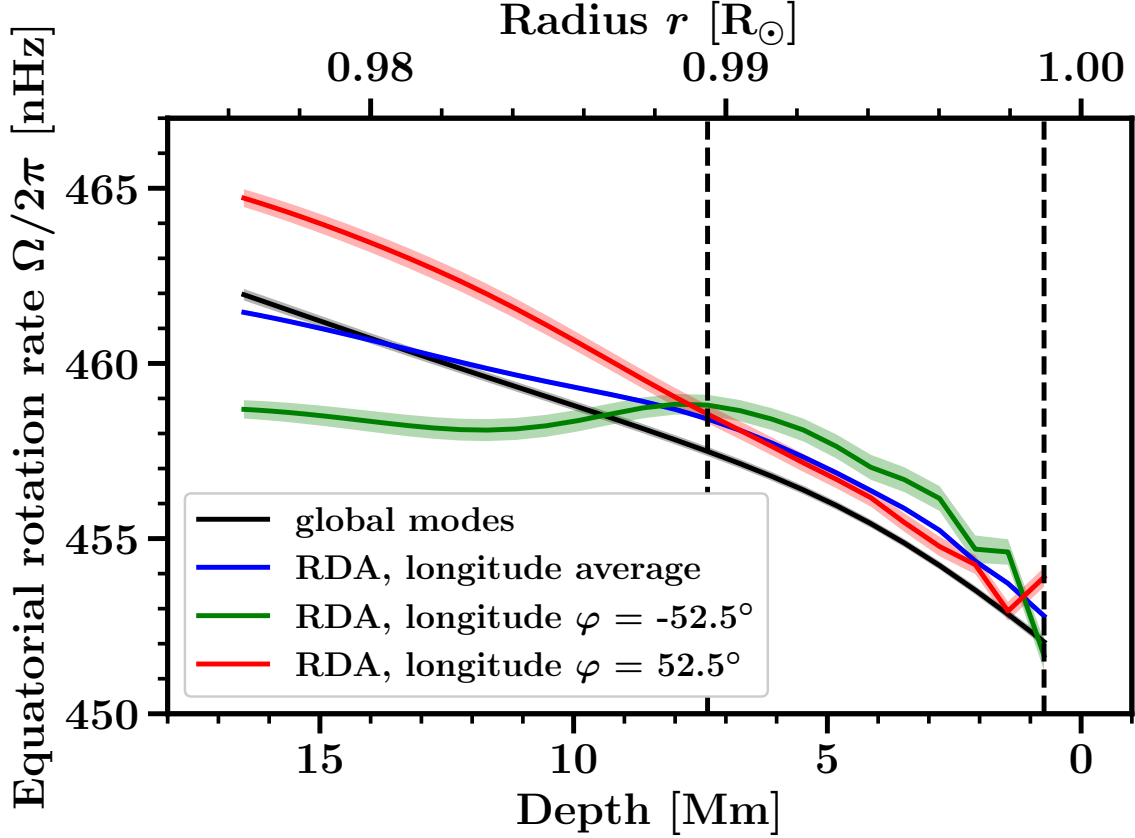
Figure 2.7: Solar equatorial rotation rate as a function of depth. The global-mode helioseismology result is given by the black curve. The blue curve is for RDA after averaging over all longitudes. The green and red curves show the ring-diagram results at Stonyhurst longitudes $\pm 52.5°$. The shaded areas give the 1σ error estimates. The observations cover more than seven years. The dashed black lines indicate the depth range within which the ring-diagram results are in best agreement with each other.

2.4.4.2 Determining the Rossby wave depth dependence

In this section, we discuss only the sectoral ($\ell = m$) component of the power spectrum of radial vorticity. The Rossby wave power $P_m(\nu, r)$ and phase $\Phi_m(\nu, r)$ thus depend on frequency, depth, and azimuthal order. Based on the assumption of damped oscillations and stochastic wave excitation, we perform a maximum-likelihood Lorentzian fit (Anderson et al. 1990) to the power spectra for the longer ring-diagram period, separately at each m. We use the functional form

$$P_{\text{fit}, m}(\nu, r) = \frac{A_m(r)}{4(\nu - \nu_{0, m})^2 / \gamma_m^2 + 1} + B_m(r). \tag{2.13}$$

We fit all the depths (except for the surface, i.e., $r = 0.0\,\text{Mm}$, where the ring-diagram data are unreliable) at once, with a common central frequency $\nu_{0, m}$ and linewidth γ_m, but with individual amplitudes $A_m(r)$ and backgrounds $B_m(r)$. The Lorentzian fit of the power spectra, in most cases, fits well to the observations. As seen in Fig. 2.3, the $\ell = m = 6$ and $\ell = m = 13$ modes have large linewidths and their power spectra show fine structure. The $\ell = m = 3$ mode has been fit by LGBD19, but not by LGBS18.

Table 2.3: Measured frequencies and linewidths of the Rossby waves from RDA sectoral power spectra with azimuthal orders in the range $3 \leq m \leq 15$. Previous measurements (with superscript 'ref') are also listed for comparison.

	This work		Previous work		
m	$\nu_{0,m}$	γ_m	$\nu^{\mathrm{ref}}_{0,m}$	γ^{ref}_m	Ref.
	[nHz]	[nHz]	[nHz]	[nHz]	
3	-230^{+5}_{-4}	40^{+13}_{-11}	-253 ± 2	7^{+4}_{-3}	LGBD19
4	-195 ± 3	16^{+7}_{-5}	-194^{+5}_{-4}	18^{+14}_{-7}	LGBS18
5	-159^{+3}_{-2}	12^{+6}_{-5}	-157 ± 4	11^{+14}_{-6}	LGBS18
6	-119 ± 6	84^{+22}_{-19}	-129 ± 8	47^{+28}_{-16}	LGBS18
7	-111 ± 3	20^{+7}_{-5}	-112 ± 4	17^{+10}_{-7}	LGBS18
8	-89 ± 3	19^{+7}_{-6}	-90 ± 3	12^{+7}_{-5}	LGBS18
9	-77 ± 4	40 ± 11	-86 ± 6	37^{+21}_{-11}	LGBS18
10	-77^{+4}_{-3}	29^{+10}_{-7}	-75 ± 5	28^{+12}_{-10}	LGBS18
11	-64^{+4}_{-5}	47^{+13}_{-12}	-75 ± 7	43^{+23}_{-13}	LGBS18
12	-59 ± 4	35^{+11}_{-9}	-59 ± 6	42^{+20}_{-12}	LGBS18
13	-45 ± 6	76^{+22}_{-20}	-40 ± 10	71^{+38}_{-22}	LGBS18
14	-47 ± 5	40^{+13}_{-11}	-56^{+6}_{-7}	36^{+20}_{-13}	LGBS18
15	-39^{+5}_{-4}	41^{+12}_{-11}	-47^{+7}_{-6}	40^{+21}_{-12}	LGBS18

To determine error bars for the amplitudes and backgrounds via chunked data (App. 2.6.3), we also perform the Lorentzian fit for each chunk separately, fitting again all depths together, but keeping the central frequency and linewidth fixed at the fit results of $\nu_{0,m}$ and γ_m from Eq. 2.13 for the full time period (to prevent unstable fits). Because we keep these parameters fixed for each chunk, we cannot derive their uncertainties based on the standard deviation over the chunks. We thus do a Monte Carlo simulation and generate 1000 realizations of synthetic power spectra according to Eq. 2.22 (App. 2.6.3) and perform the Lorentzian fit for each realization analogously to the fit for the observations. The median of the parameters over the Monte Carlo realizations is consistent with the fit parameters for the observations. While the error based on the Monte Carlo simulation contains realization noise, the model we use (Lorentzian and stochastic excitation) does not include all features of the observed power spectra. The chunk-based error likely describes the physical system more accurately, by also including other variance contributions, such as from temporal effects on the Rossby waves; we could imagine, for example, solar cycle effects. This may also explain the discrepancy between the two types of errors of order 30 % (App. 2.6.3). This disagreement is, however, small enough to not affect the significance of the results for the radial eigenfunctions. We thus use the uncertainties based on the Monte Carlo simulation for the central frequency and the linewidth.

Table 2.3 compares the fit parameters from this study with the results from LGBD19 and LGBS18. As in LGBD19 and LGBS18, the upper and lower errors give the difference between the quantiles comprising the central 68.3 % (the distributions are non-Gaussian) and the fit parameters for the observations. We also calculate the uncertainties on the cen-

tral frequency following Libbrecht (1992) and find that those (symmetric) errors typically underestimate the Monte Carlo quantile errors by roughly 1 nHz. A possible reason for this could be that we use a finite frequency fitting interval.

The fit parameters for the observations and those from LGBD19 and LGBS18 typically agree within 1σ or better. The central frequencies and the linewidths for the $\ell = m = 6$ mode differ by 10 and 37 nHz, but the fit is sensitive to the fitting range. The $\ell = m = 3$ fit parameters do not agree. In LGBD19, the authors, using 21 years of data, observed that the multi-peak structure of the $\ell = m = 3$ power spectrum (Fig. 2.3) seen in data with shorter periods collapses to a narrow single peak, which indicates that the discrepancy of the fit parameters is explained by stochastic excitation of the Rossby waves and vanishes when fitting data with a longer time period. Our errors are typically more symmetric and often smaller than those of LGBD19 and LGBS18. The lower errors for the linewidth often agree better than the upper errors, indicating a tail of high values (skewness) in the LGBD19 and LGBS18 estimate distributions. Reasons for the differences in the error estimates may lie in the simultaneous fitting of all depths at once or in the different observation periods of our datasets and those of LGBS18.

To determine the power depth dependence, we use the amplitude A derived from the Lorentzian fit (see Eq. 2.13) and we define the normalized power of the signal as

$$\mathcal{P}_{\text{signal},m}(r) = \frac{A_m(r)}{\langle A_m(r) \rangle_r}. \tag{2.14}$$

We thus normalize by the depth average of the amplitude of the Lorentzian. The normalized power is independent of temporal amplitude variations due to Rossby wave excitation.

2.4.4.3 Results for the radial eigenfunctions

Figure 2.8 shows the depth dependence of the $\ell = m = 8$ phase, but the behavior is similar for other m. For easier comparison, we remove phase jumps of $360°$ and move the depth average to zero. The phase at the frequency of maximum power is almost constant with depth, within roughly $\pm 3°$. The phase at the background, at the center of the background interval, varies much more strongly with depth, within roughly $\pm 100°$, although the phases at other background frequencies sometimes show much less variation. The background phase is not random in depth (see App. 2.6.3). In particular, phase changes are gradual and smooth; the depths are correlated. This could indicate a significant contribution from scattered signal power to the background. Nonetheless, peak and background display distinctly different depth dependences. We also find that phases at different frequencies across the peak and background are different. Frequency averages of phases are thus not useful. However, as seen, for single frequencies the phase at the peak is nearly constant with depth, while the background phase varies with depth.

Figure 2.8 also shows the main parameters of the ring-diagram averaging kernels for a few target depths, i.e., the first, second (median) and third quartiles and the width (interquartile range). The flow measurements are well-localized near the surface, but smeared out over a broad depth range at large depths. The ring-diagram depth covariance matrix (not shown) indicates a similar behavior and shows that different depths are mostly independent near the surface, while at the largest depths there is high correlation and they
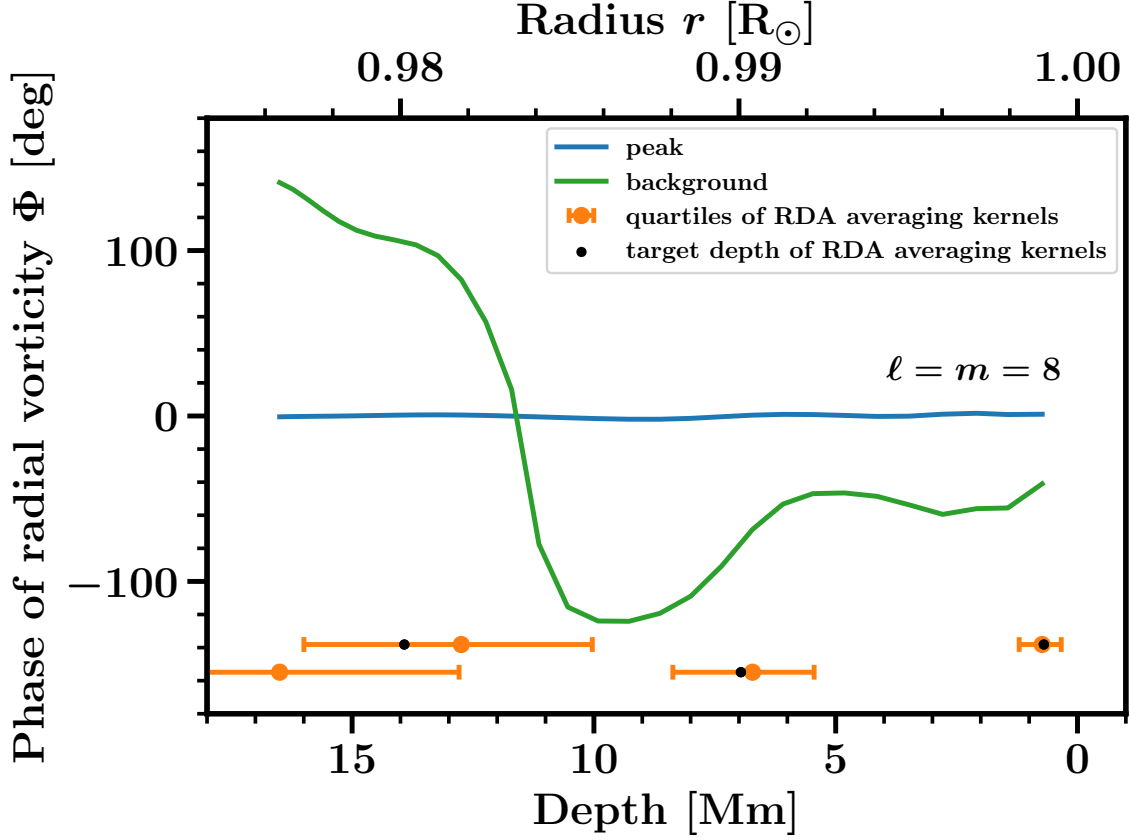
Figure 2.8: Phase at a frequency of roughly $-87.4\,\mathrm{nHz}$ corresponding to the peak of power for the Rossby mode $\ell = m = 8$, as a function of depth (blue curve). The green line shows the phase of the background at the center of the background interval (see Eq. 2.3). The depth refers to the median of the ring-diagram averaging kernels (orange dots), which corresponds to certain target depths (black dots).

thus do not give independent results. This could maybe also explain why the background phase is not random in depth. At large depths, the center of the averaging kernels (second quartile) moves away from the target depth, but the averaging kernels are relatively symmetric.

Figure 2.9 shows the signal power (Eq. 2.14). The quantity $\mathcal{P}_{\mathrm{signal}}$ typically decreases from the surface toward a depth of $8\,\mathrm{Mm}$, significantly as shown by the errors. Even further inside the Sun the power often increases again and reaches near-surface or even higher values. The 1σ errors shown in this plot give the standard deviation, but they do not indicate $68.3\,\%$ probability intervals, since the power distribution is non-Gaussian (power cannot be negative). More information about error estimation can be found in App. 2.6.3.

Provost et al. (1981) presented a theoretical argument that the Rossby wave eigenfunctions for the horizontal displacement are proportional to r^m under the assumption that the modes are incompressible. Thus, under this theory, the radial vorticity is expected to be proportional to r^{m-1}. To compare this to our observations, we perform a fit of the
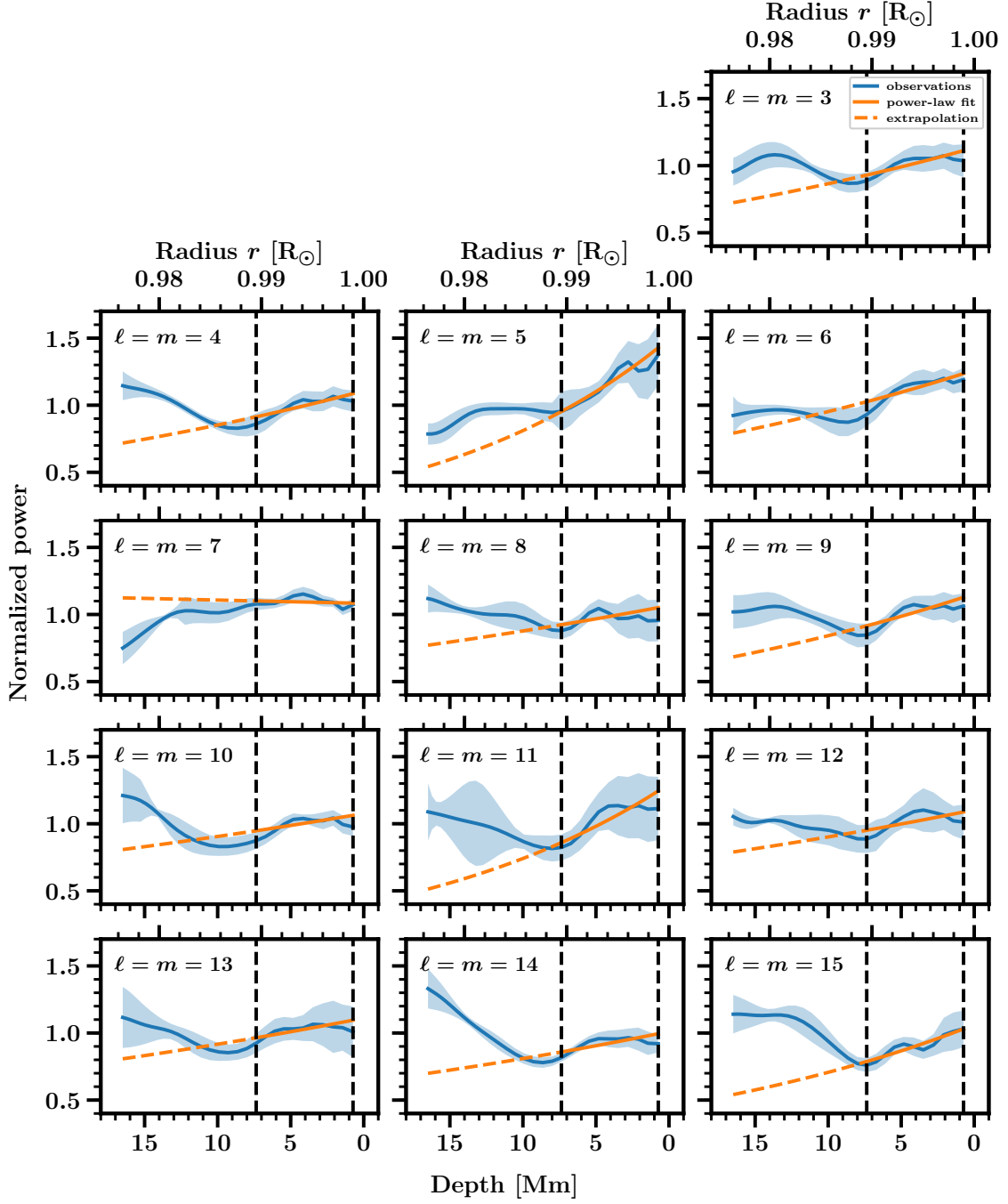
Figure 2.9: Blue lines show the Rossby wave power $\mathcal{P}_{\text{signal}}$ as a function of depth for different values of m. The blue shaded areas indicate the 1σ errors. The orange curves are fits of the form $const. \times r^{2\alpha}$ over depths between 0.7 and 7.4 Mm (between the vertical dashed lines). The orange dashed curves are extrapolations to larger depths.
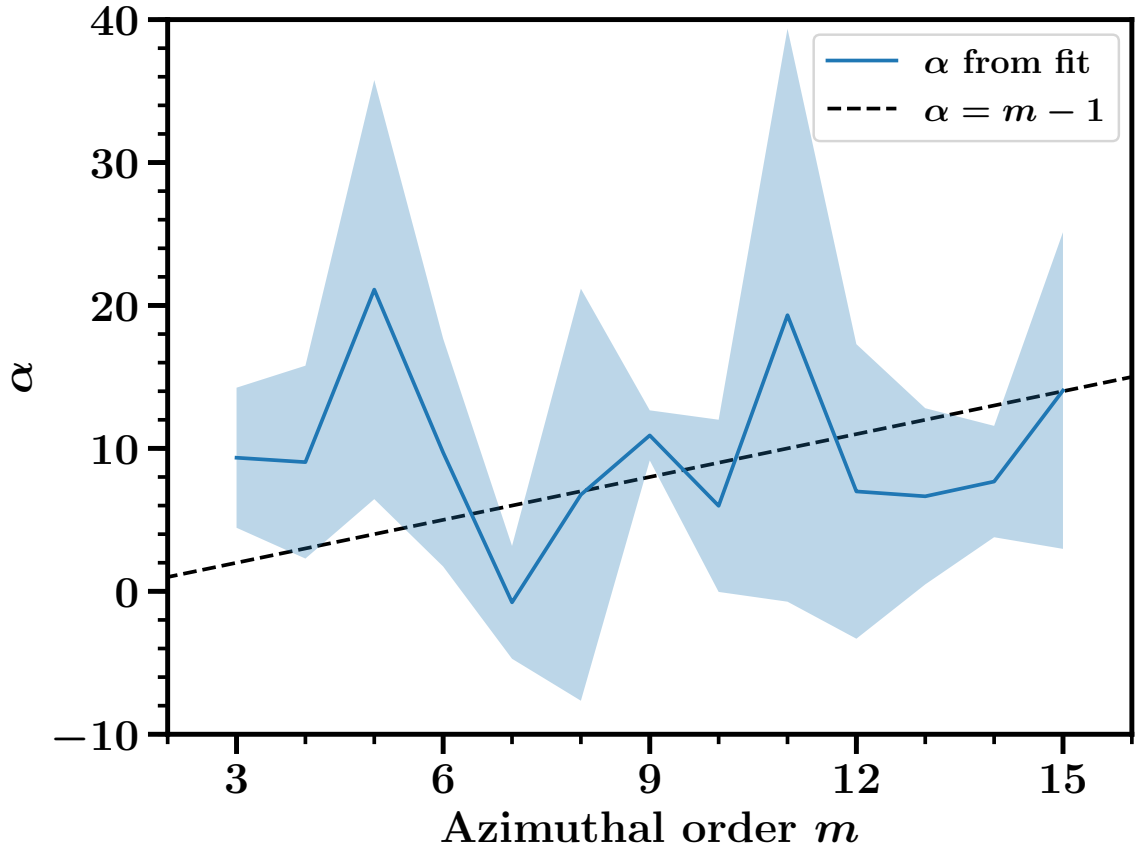
Figure 2.10: Exponent α as a function of m, measured in the top 7.4 Mm (blue line) and 1σ error (blue shaded area). The dashed black line corresponds to the model $\alpha = m - 1$, obtained under the assumption of non-divergent motions (Provost et al. 1981).

form $const. \times r^{2\alpha}$ to $\mathcal{P}_{\text{signal}}$ within the dashed black lines (0.7 to 7.4 Mm) where the RDA is more reliable (see Fig. 2.7). We assume that the data points are uncorrelated in depth. Obviously, the fit does not reproduce the increase of power at large depths.

Figure 2.10 compares the observed and theoretical exponent α. The fitted exponent has very large error bars. It is consistent with the theoretical model from Provost et al. (1981), but also with the absence of any trend with m. Although the exponent depends strongly on the fit range because of the kink at roughly 5 Mm in Fig. 2.9, we also do not find inconsistency with a flat dependence on m within other fit intervals. Thus the current error estimates do not allow a definitive statement on the radial dependence of Rossby waves.

2.5 Summary

We build on LGBS18, who investigated Rossby waves mostly using granulation tracking, by studying several Rossby wave properties via the analysis of radial vorticities computed from RDA at different depths and LCT at the surface. We obtained several new results: independently the latitudinal eigenfunctions with RDA (including a more complete, complex-valued description of the eigenfunctions), and the Rossby wave power and

phase depth dependence.

We calculated latitudinal eigenfunctions of Rossby waves from the radial vorticity maps via the covariance between the equator and different latitudes and from the singular vectors of an SVD. We confirmed the shape of the real part of the eigenfunction from LGBS18, who used the covariance method on symmetrized LCT data. We also saw consistency between covariance and SVD results, except for $m = 5$ and $m = 6$, where the SVD eigenfunctions had maxima around ± 10-$15°$ instead of at the equator. The shape of the real part of the latitudinal eigenfunctions seen for most m indicates that the Rossby waves have maximum amplitudes near the equator, as found by LGBS18. The imaginary part appears to be mostly positive for low m ($3 \leq m \leq 6$); this part varies around zero for intermediate m ($7 \leq m \leq 9$) and is mostly negative for high m ($10 \leq m \leq 15$). A nonzero imaginary part may be due to attenuation and to the interaction of the waves with large-scale flows. In particular, the interaction of viscous Rossby waves with latitudinal differential rotation leads to the formation of critical layers at intermediate latitudes (Gizon et al. 2020, submitted).

We defined and measured characteristic parameters for the real part of the eigenfunctions and we found that the width at an eigenfunction value of 0.5 (the HWHM) decreased with m, in contrast to the m-independent width at a value of 0 and the latitude and value of the eigenfunction minimum. We also decomposed the eigenfunctions into associated Legendre polynomials and saw that the real part is dominated by $\ell = m$ and $\ell = m + 2$ contributions, while the imaginary part consists mostly of $\ell = m + 4$ and $\ell = m + 2$ contributions for low and high m, respectively.

We compared rotation rates from ring-diagram data and global modes as functions of depth and saw a small offset at small depths and disagreement at large depths, but most importantly inconsistency of different ring-diagram longitudes. This indicated systematic effects in the ring-diagram pipeline (see also Komm et al. 2015).

We studied the Rossby wave power and phase depth dependence in detail for the first time. The phase at the peak is stable with depth, in contrast to the phase of the background. The background power almost monotonically increases with depth, while the signal power decreases toward a depth of 8-9 Mm and then increases again. The radial eigenfunctions of the Rossby waves are (at small depths) consistent with a power-law decrease, in particular both with the theoretical Provost et al. (1981) model (exponent $m - 1$) and an m-independent exponent. However, the Provost et al. (1981) model is based on assumptions that are not exactly correct for the Sun (e.g., uniform rotation). We can constrain the radial dependence of the eigenfunctions only very weakly owing to the high uncertainties on the observed exponents.

The analysis presented in this paper implicitly makes the assumption that the Rossby wave eigenfunctions are separable in depth and latitude. Our data show a similar latitude dependence for the different depths, separability thus appears to be a reasonable assumption. The results shown in this work motivate further research on Rossby wave eigenfunctions, which is a necessary condition for the interpretation of the measured mode frequencies.

2.6 Appendix

2.6.1 Issues of the ring-diagram inversions

In this appendix, we discuss two issues regarding the ring-diagram pipeline inversions. In order to obtain local velocities at a certain measurement depth r, the reported pipeline velocities must be multiplied by $r/R_\odot$. Additionally the pipeline inversion does not take the quantity $\beta_{n\ell}$ (see, e.g., Aerts et al. (2010), Eq. 3.357) into account and thus the reported inversion velocities u_x are slightly incorrect.

To see this, we study a simple case. For now, let us assume that the ring diagrams are not tracked. The frequency perturbation $\delta\omega_{n\ell m}$ of the mode indexed by radial order n, angular degree ℓ, and azimuthal order m due to a radial differential rotation rate $\Omega(r)$ is

$$\delta\omega_{n\ell m} = m\beta_{n\ell} \int_0^{R_\odot} K_{n\ell}(r)\Omega(r)dr, \qquad (2.15)$$

where $K_{n\ell}$ is the normalized rotation kernel for that mode, i.e., $\int_0^{R_\odot} K_{n\ell}(r)dr = 1$ (see, e.g., Aerts et al. (2010), Eq. 3.358). On the other hand, ring diagrams assume that the velocity mode fits $U_{x,n\ell}$ are equal to a radial integral over the true velocity flow field $u_x(r)$ weighted by flow sensitivity kernels. Based on inspection of the pipeline, we think that the used HMI kernels are normalized rotation kernels $K_{n\ell}$ from Eq. 2.15. Thus

$$U_{x,n\ell} = \int_0^{R_\odot} K_{n\ell}(r)u_x(r)dr. \qquad (2.16)$$

To connect the two equations in a simple case, consider the Doppler shift of a sectoral ($\ell = m$) mode as seen by a ring diagram at the equator, i.e.,

$$U_{x,n\ell}k_x = \delta\omega_{n\ell m} = m\beta_{n\ell} \int_0^{R_\odot} K_{n\ell}(r)\Omega(r)dr. \qquad (2.17)$$

In this equation, k_x is the wavenumber in the prograde direction, which is related to m via $k_x = m/R_\odot$. We conclude that

$$U_{x,n\ell} = \beta_{n\ell} \int_0^{R_\odot} K_{n\ell}(r)R_\odot\Omega(r)dr. \qquad (2.18)$$

This is not consistent with Eq. 2.16 since $\beta_{n\ell}$ is missing from Eq. 2.16. Additionally we see that $u_x(r)$ should be interpreted as $R_\odot\Omega(r)$ and not as the local linear velocity $r\Omega(r)$.

To see what happens if the tracking rate is not zero, we now suppose that we track at rotation rate Ω_T. Equation 2.18 then becomes

$$\tilde{U}_{x,n\ell} = \left[\beta_{n\ell} \int_0^{R_\odot} K_{n\ell}(r)R_\odot\Omega(r)dr\right] - R_\odot\Omega_T, \tag{2.19}$$

where $\tilde{U}_{x,n\ell}$ is the ring measurement in the rotating frame. We now define the local deviation from the tracking rate $\delta\Omega(r) = \Omega(r) - \Omega_T$. Then we obtain

$$\tilde{U}_{x,n\ell} = \left[\beta_{n\ell} \int_0^{R_\odot} K_{n\ell}(r)R_\odot\delta\Omega(r)dr\right] + (\beta_{n\ell} - 1)R_\odot\Omega_T. \tag{2.20}$$

The first term is the same form as in Eq. 2.18, while the second term is an offset that depends on n and ℓ.

The conversion factor $r/R_\odot$ is multiplied onto the data before any analysis is performed for this paper; see Sect. 2.3.2. The offset due to $\beta_{n\ell}$ depends on the set of mode ring fits, but it should be mostly time-independent, since the ring-diagram mode set does not vary much with time. Thus the time-dependent Rossby waves should not be sensitive to this effect and the only affected result in this paper should be the comparison of rotation rates in Fig. 2.7.

To estimate the effect of $\beta_{n\ell}$ on the inversion result, for a given input flow u_x we generate artificial ring fits $\tilde{U}_{x,n\ell}$ via Eq. 2.20, on which we run the ring-diagram inversion module to retrieve the output velocities. To compute $\tilde{U}_{x,n\ell}$, we assume a depth-independent flow equivalent to the tracking rate (sidereal Carrington rate), thus $\delta\Omega(r) = 0$. We thus check only the second term of Eq. 2.20 and neglect that $\beta_{n\ell}$ also appears in the first term as a scaling factor. However, the effect due to the second term should be much larger than that due to the first term, as Ω_T is much larger than $\delta\Omega(r)$ for the ring diagrams.

We use $\beta_{n\ell}$ values provided by V. Böning (priv. comm.). These were computed from eigenfunctions obtained from the Aarhus adiabatic oscillation package (ADIPLS; Christensen-Dalsgaard 2008, 2011). We lose roughly 25 % of the original ring-fit modes, as we only have $\beta_{n\ell}$ values up to frequencies of 5 mHz. However, this does not critically change the mode set used during the inversion. We replace the actual pipeline ring fits with the artificial data. We leave all other data, including uncertainties on mode-fit velocities, as is and perform the inversion. The aforementioned conversion factor of $r/R_\odot$ is multiplied onto the output velocities u_x.

We see that the effect of $\beta_{n\ell}$ does not depend much on depth and that the retrieved u_x are on the order of only $1.5\,\mathrm{m\,s^{-1}}$ (equivalent to roughly 0.1 % of the tracking rate). The reason for this is that the inversion gives much more weight to the high ℓ modes for which the uncertainties are comparatively small. These modes typically have $\beta_{n\ell}$ values around 0.999, thus $1 - \beta_{n\ell} \sim 0.1\,\%$. We performed this check exemplarily for a ring-diagram tile at the first time step in our dataset (May, 20, 2010) at the point ($\lambda = 0°, \varphi = 0°$). However, tests using different tiles show that this result does not depend much on time or disk position.

The effect of the pipeline inversion not accounting for $\beta_{n\ell}$ is thus an underestimation of the true velocity fields by roughly 1-2 $\mathrm{m\,s^{-1}}$, or equivalently approximately 0.4 nHz. This difference would be visible in Fig. 2.7, but does not change our main conclusions.

2.6.2 Interpolation and apodization of ring-diagram velocities

We interpolate the ring-diagram velocities separately in time and longitude (see Sect. 2.3) with different functions, depending on the number of available data points:

$-\geq 4$ data points: cubic splines

$- 3$ data points: quadratic splines

$- 2$ data points: linear splines

Before we interpolate the ring-diagram velocities to the surface equatorial rotation rate, we apodize these velocities with a raised cosine in angular great-circle distance ρ to the point ($\lambda = 0°, \varphi = 0°$), see Sect. 2.3), as follows:

$$H(\rho) = \begin{cases} 1 & \text{if } |\rho| \leq \frac{1-\beta}{2T}, \\ \frac{1}{2}\left\{1 + \cos\left[\frac{\pi T}{\beta}\left(|\rho| - \frac{1-\beta}{2T}\right)\right]\right\} & \text{if } \frac{1-\beta}{2T} < |\rho| \leq \frac{1+\beta}{2T}, \\ 0 & \text{else,} \end{cases} \qquad (2.21)$$

where β defines the steepness of the raised cosine flanks. We choose $\beta = 0.3$. The quantity T defines the central position of the flanks. We choose T such that zero is reached at $\rho = 67.5°$ (where there are no more valid pixels). Apodizing the ring-diagram velocities (with different β), or not, gives consistent results.

2.6.3 Error estimation and error validation

2.6.3.1 Error estimation via chunked data

The uncertainties on all results are derived by dividing the time series of vorticity maps (in total 2448 time steps, i.e., 102 rotations, for RDA) into equal-size chunks and calculating the scatter over the results for the chunks. We find that for chunks longer than a few months (roughly six rotations), the Rossby wave signature is visible in the power spectra. We make a compromise between noise level and chunk statistics and divide the dataset into five chunks that are 480 time steps long each (20 rotations).

For the latitudinal eigenfunctions, where we only study the shorter LCT period (i.e., 78 rotations), we first used four chunks of length 19 rotations (rotation-averaged maps) and 470 time steps (full time resolution, for RDA), but we obtained very large errors for the SVD method for different single m, where single chunks gave singular vectors different from the usual eigenfunction shape. We think that the noise in our filtered maps might have been detected as the dominant term in the decomposition. We thus use a chunking with three chunks of length 26 rotations and 625 time steps, where all chunks have the expected first singular vectors.

2.6.3.2 Error validation via Monte Carlo simulation

We validate the chunking approach for the depth dependence via a Monte Carlo simulation. As a plausible physical model for the Rossby wave power spectrum, we assume a Lorentzian profile and a background (constant in frequency), each with a χ^2-distributed

random variable (stochastic excitation). In analogy to Eq. 2.13 we generate 1000 realizations of synthetic data for the Fourier transform of the radial vorticity $\mathcal{F}_{\text{syn}}$ (not the power P), at each m, as

$$\mathcal{F}_{\text{syn},m}(\nu, r) = \sqrt{\frac{A_m(r)}{4(\nu - \nu_{0,m})^2/\gamma_m^2 + 1}}\mathcal{N}_{A,m}(\nu) + \sqrt{B_m(r)}\mathcal{N}_{B,m}(\nu, r). \qquad (2.22)$$

We fix the amplitude $A_m(r)$, background $B_m(r)$, central frequency $\nu_{0,m}$, and full width at half maximum γ_m via the fit parameters for the observations. Furthermore we assume that the random variable $\mathcal{N}_{A,m}(\nu)$ is constant with depth, i.e., the signal is fully correlated in depth, while for the background, we take a random variable $\mathcal{N}_{B,m}(\nu, r)$ that is uncorrelated in depth. The random variables are complex Gaussian variables (with independent real and imaginary parts) with zero mean and unit variance, independent for each frequency. We analyze the realizations in the same way as the observations.

We observe inconsistency between two Monte Carlo estimates (by roughly 30 %): one from chunking (like the observations), averaged over the realizations, and the other from the scatter of the power over the realizations. We find that the discrepancy is due to the temporal correlation of the different chunks; the temporal correlation matrix has values around 0.1 on the first off-diagonal. The two quantities agree when using a weighted average with weights based on the temporal covariance matrix.

Both Monte Carlo estimates disagree with the error for the observed data. This could be due to the depth correlation of the observations. We determine a (noisy) estimate of the depth covariance and correlation matrix of the observed background power from the different background frequencies and find strong correlations between different depths, even between the largest depth and the surface, with values above 0.25 in the off-diagonal corners. We use the observed depth covariance matrix for the Fourier transform (not the power) to correlate the Gaussian background random variable of our realizations, via a Cholesky decomposition.

Correlating the background in depth noticeably improves the agreement between Monte Carlo and observed errors. However, there is still a remaining discrepancy that can be attributed to our model, which is missing some features of the observed power spectrum. We do not account for the window function nor a background decreasing with frequency present in the observations. A detailed analysis goes beyond the scope of this paper.

2.6.4 Relation of covariance to linear fit

The covariance method (Sect. 2.4.3.1) is conceptually equivalent to a linear fit of the vorticity at each depth r and latitude λ, i.e.,

$$\tilde{\zeta}'_m(t, r, \lambda) = a_m(r, \lambda)f_m(t). \qquad (2.23)$$

Let us for simplicity assume that the vorticity $\tilde{\zeta}'_m(t, r, \lambda)$ is real. The latitude and depth dependence in this vorticity separation ansatz is contained in the fit parameter $a_m(r, \lambda)$. Let us assume that only $\tilde{\zeta}'$ is uncertain. For zero-mean quantities (such as our vorticity maps $\tilde{\zeta}'$), the slope of a linear fit without intercept, i.e., $a_m(r, \lambda)$, is given as

$$a_m(r, \lambda) = \frac{\langle \tilde{\zeta}'_m(t, r, \lambda)f_m^*(t) \rangle_t}{\langle |f_m(t)|^2 \rangle_t}. \qquad (2.24)$$

Assuming the time dependence is given by the surface equatorial vorticity time series, i.e., $f_m(t) = \tilde{\zeta}'_m(t, r = R, \lambda = 0°)$, in Eq. 2.8 we can identify $a_m(r, \lambda)$ with $C_m(r, \lambda)$. Equation 2.23 implies that $a_m(r = R, \lambda = 0°)$ is unity.

The main disadvantage of the covariance method is the assumption of a noise-free vorticity at the equator, $\tilde{\zeta}'_m(t, r = R, \lambda = 0°)$, required so that the time-dependence $f_m(t)$ is noise-free and the vorticity $\tilde{\zeta}'_m(t, r, \lambda)$ is the only uncertain quantity of the fit.

3 Revisiting helioseismic constraints on solar convection

3.1 Abstract

There is substantial disagreement between the helioseismic upper limits on the amplitude of east-west subsurface convective flows from Hanasoge et al. (2012) and the inferences of the strength of these flows by Greer et al. (2015). In addition, the upper limit obtained by Hanasoge et al. (2012) disagrees with simulations of solar convection (Miesch et al. 2008). Additional observational and theoretical work on the topic of solar subsurface convection is crucial. Motivated by the need to establish a clear baseline for future work, we describe and remedy several inconsistencies in the figures shown in Hanasoge et al. (2012), Gizon and Birch (2012), Greer et al. (2015), and Hanasoge et al. (2016). After these corrections, all of the previous disagreements remain. To provide a larger context for these measurements, we provide new estimates of the strength of surface convection from correlation tracking of SDO/HMI continuum images and of subsurface convection from the SDO/HMI ring-diagram pipeline. These new measurements are both above, but qualitatively similar to, the upper limit on convection from Hanasoge et al. (2012), but well below the inferences of Greer et al. (2015).

3.2 Introduction

Solar subsurface convection is a crucial ingredient in solar global-scale dynamics as it determines the Reynolds stresses that maintain differential rotation (e.g. Miesch 2005). Subsurface convection may also play a key role in the dynamics of the subsurface magnetic flux concentrations that emerge through the solar surface and form active regions (e.g. Cheung and Isobe 2014).

Hanasoge et al. (2012, hereafter HDS2012) used local helioseismology (see Gizon et al. 2010, for a review) to obtain an upper limit on the strength of horizontal convective flows in the depth range of 20-30 Mm below the photosphere. This result suggested that simulations of solar convection (e.g. Miesch et al. 2008, hereafter M2008) overestimate the strength of convective flows in this depth range by roughly two orders of magnitude

at large scales. Using three-dimensional inversions of helioseismic measurements Greer et al. (2015, hereafter GHFT2015), however, found that the amplitudes of the flows in this depth range are (order-of-magnitude) compatible with the simulations. The stark differences between HDS2012 and GHFT2015 measurements and also between the result of HDS2012 and simulations call for a detailed look at the current state of understanding of solar subsurface convection (see also Gizon and Birch 2012, Hanasoge et al. 2016).

Here, we revisit the existing comparisons of various estimates of, or limits on, flow amplitudes. In the course of this work we have found a number of "apples and oranges" comparisons in the literature (in particular HDS2012; Gizon and Birch 2012, hereafter GB2012; GHFT2015; and Hanasoge et al. 2016, hereafter HGS2016) as well as a few cases where the analysis that was performed was not correctly described in the publication. We build on these previous results and present consistent comparisons of inferences of the amplitudes of solar convection. In addition, we provide new measurements of the strength of convection at the surface from the correlation tracking of granulation (Löptien et al. 2017) and below the surface using ring-diagram analysis (Hill 1988) from the SDO/HMI ring-diagram pipeline (Bogart et al. 2011a,b). Our overarching goal is to a provide a clearly described baseline for further investigations.

3.3 Revisiting previous work

In this section we review the datasets and methods that led to the comparison figures of HDS2012, GB2012, and GHFT2015. In addition we describe a problem introduced by the journal in Fig. 5 of HGS2016. As described in the introduction, the goal of this work is to provide a baseline for future work. We emphasize that our current aim is *not* to test the assumptions that led to the conclusions of these studies.

3.3.1 HDS2012

Here we elaborate on the descriptions from HDS2012 for a few steps that were not clearly described in the original publication. The maps of east-west travel-time differences were generated using a phase-speed filter and deep-focusing geometry as described in HDS2012. The spherical harmonic power spectrum $\tilde{P}_{\ell,m}$ (the tilde is to show that the HDS2012 normalization of the SHT is used; see Eq. 3.11; ℓ is the angular degree and m is the azimuthal order) was computed from the Carrington map of east-west travel-time differences. The power spectrum was divided by 0.27162, with the aim of correcting for the effect of missing data in the Carrington map (latitudes above about $\pm 58.3°$ and the missing data in longitude ϕ[1] due to using only 17 days of data instead of a full rotation of about 27 days). This factor should have been

$$\alpha = \frac{1}{4\pi} \int_0^{2\pi} \int_0^{\pi} w(\theta, \phi) \sin\theta \, \mathrm{d}\theta \, \mathrm{d}\phi = 0.529 \,, \tag{3.1}$$

where θ is co-latitude, ϕ is longitude, and $w(\theta, \phi)$ is the window function ($w = 1$ where data is available and $w = 0$ otherwise). The factor of $\sin\theta$ was neglected in the original

---

[1]In contrast to Chap. 2, here we denote the longitude with ϕ instead of φ. In Chap. 4, both symbols are used. This ambiguity arises from different conventions in the papers forming the basis of these chapters.

calculation.

The rms travel time *per mode* was then estimated from the *m*-averaged power spectrum as $\delta\tau_\ell = \sqrt{\langle\tilde{P}_{\ell,m}\rangle_{m>0}/\alpha}$; the angle brackets $\langle\cdot\rangle$ denote the average. The $m = 0$ modes are not included in this calculation (this removes the contribution of the differential rotation and torsional oscillations). The rms travel time per mode is then converted to a rms flow per mode v_ℓ using:

$$v_\ell = \delta\tau_\ell / \left[c_\ell DN/S \right] \, , \qquad (3.2)$$

where c_ℓ denotes the calibration curve (see Fig. 3.5), D is the ratio of the assumed radial extent of the flow field to the radial extent of the test functions used to compute c_ℓ, and the factor N/S corrects for the contribution of noise to the $\delta\tau_\ell$ (see Sect. 3.6.3). For the target depth $r = 0.96\,R_\odot$, HDS2012 used $D = 9.64$ based on the assumption that the flows cover a radial extent given by the mixing length, assumed to be given by 1.8 pressure scale heights. For the target depth $r = 0.96\,R_\odot$, HDS2012 used $N/S = 2$. Section 3.6.3 shows that re-analysis of the data (using the original method) suggests that this factor should have been $N/S = 4.7$.

3.3.2 Figure 5 of HDS2012

Figure 5 of HDS2012 is not consistent as it compares the upper limit rms *per mode* from helioseismology with the rms *per multiplet* from M2008. In addition, as discussed in Sect. 3.3.1, the area correction and N/S correction factors are not as described in the text.

3.3.3 Figure 1 of GB2012

Figure 1 of GB2012 contains several errors: (1) The calculation of the E_ϕ (Sect. 3.6.1.2) for the helioseismology upper limit of HDS2012 was based on the misunderstanding that the upper limit was an rms *per multiplet* rather than an upper limit *per mode*. In addition a factor of $1/4\pi$ was missing due to different conventions for the spherical harmonics transform (see Sect. 3.6.1.2). (2) The calculation of the E_ϕ for the Roudier et al. (2012, hereafter R2012) correlation tracking is missing a factor of $1/2$.

3.3.4 Figure 5 of GHFT2015

Figure 5 of GHFT2015 is not consistent as it compares the rms *per multiplet* from the ASH simulations, with the rms *per bin* in horizontal wavenumber from the ring-diagram inversions. The bin size is about 9.2 in angular degree. Thus the helioseismic measurements should have been scaled down a factor of $\sqrt{9.2}$ for comparison with the simulations. In addition, the upper limit from HDS2012 is rms *per mode* and should have been converted to rms *per multiplet* for the sake of comparison.

3.3.5 Figure 5 of HGS2016

Figure 5 of HGS2016 is based on Fig. 1 of GB2012 and contains the same issues. In addition, the y-axis labels are not correct. The y-axis in the figure provided to the journal extends from 10^{-3} to 3×10^3.

3.3.6 Summary of the revisions

Figure 3.1 shows the original and revised versions of HDS2012, GHFT2015, and R2012. As discussed above, the corrections are multiplicative factors for GHFT2015 and R2012. The E_ϕ for GHFT2015 is reduced by a factor of the bin size in angular degree (about 9.2) and the R2012 curve is corrected downward by a factor of two. The situation is more complicated for the HDS2012 curve. The change in the slope of the curve comes from the correction from computing the m-averaged power to the m-summed power. This multiplies the original curve by a factor of $2\ell + 1$. The other corrections (new N/S correction and new area correction) are scalings.

3.4 New measurements

To establish a larger context for the flow amplitudes shown in the previous section, we here use two additional existing measurements of horizontal flows to estimate the spectrum of convective velocities. Löptien et al. (2017) measured horizontal flows at the solar surface by tracking the granulation pattern seen in the SDO/HMI continuum images. The SDO/HMI ring-diagram pipeline (Bogart et al. 2011a,b) applies ring-diagram analysis to Doppler images to infer horizontal flows in the depth range from just below the surface down to about 16 Mm.

3.4.1 Surface flows from granulation tracking

The correlation tracking described by Löptien et al. (2017) is based on applying the FLCT code (Welsch et al. 2004, Fisher and Welsch 2008) to pairs of SDO/HMI continuum images separated by 45 s. A flow map with a pixel size of 0.4° (about 4.8 Mm at disk center) was computed every 30 min. Working in Stonyhurst coordinates, large-scale systematic effects with periods of one day and one year (and harmonics) and steady flows were removed from a time-series of maps using an expansion in Zernike polynomials followed by Fourier filtering in time (see Löptien et al. 2017, for details). The resulting 30 min cadence flow maps were used by Löptien et al. (2017) to measure the inflows into active regions. These maps have also been used to study equatorial Rossby waves (Löptien et al. 2018, Proxauf et al. 2020).

There is a wide range of possible approaches to estimating the spectrum of east-west velocities from these maps. Here we explore three options:

- Construct Carrington maps of the east-west velocity by concatenating strips that cover 15.12° in longitude, each strip is a 27.5-hr average. This is essentially the approach of HDS2012 but with slightly wider strips and slightly longer averaging in time.

- Extract a 60° × 60° patch near disk center from a 27.5-hr time average of east-west velocities. This is the approach of GHFT2015 but with a slightly different time averaging (GHFT2015 used 25.6 hr).

- Extract a 650" × 650" patch near disk center ($\sim 40° \times 40°$) from a 2-hr average map. This is the approach of R2012.
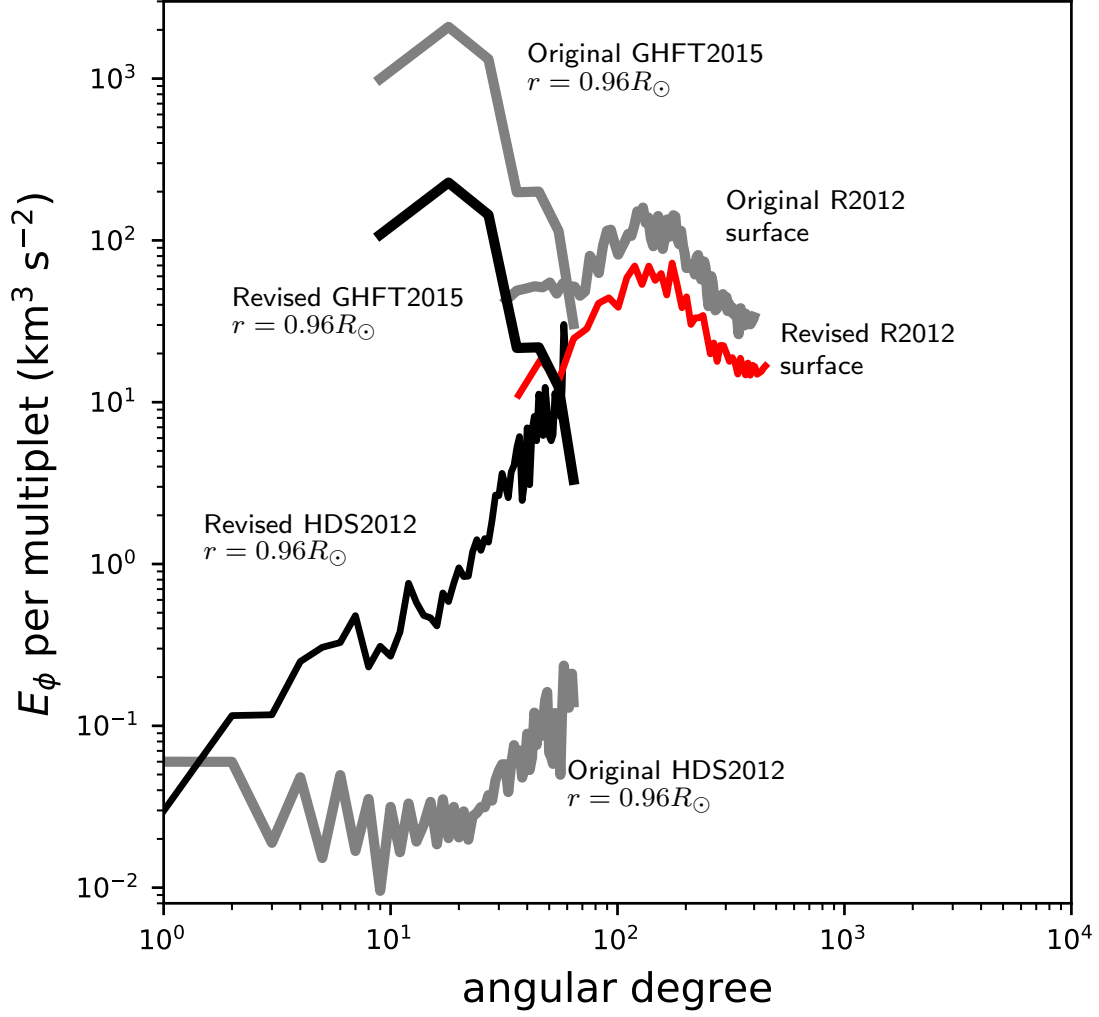
Figure 3.1: Revised (black or red) and original (grey) estimates of $E_\phi(\ell)$ for the HDS2012, GHFT2015, and R2012 results. In this work we have not found any issues with the original (GB2012) calculations for the stagger or ASH results and so no additional curves are plotted for these two cases. The discrepancy between the upper limit of HDS2012 and the simulations and the ring-diagram result (GHFT2015) remains for $\ell \lesssim 50$ but is reduced in amplitude. The small deviation from a pure scaling between the original and revised R2012 curve is due to a change in the spatial apodization.

For the ring diagrams, the patch widths refer to latitude or longitude ranges measured between the centers of the ring diagram tiles. For the local correlation tracking they are measured from pixel centers. The final step in all cases was to compute the SHT and then the m-summed power. In all cases, to reduce noise we averaged the resulting power spectra over the 25% of Carrington rotations with the smallest sunspot numbers.

Over the range of ℓ covered by all three methods, the HDS2012 and GHFT2015 averaging schemes give similar results for E_ϕ. The power measured by the R2012 averaging scheme is somewhat is higher because of the shorter averaging time (2 hr vs. about one day). From here on, we choose to only show the result from the HDS2012-like analysis as this averaging provides full Carrington maps (and thus full resolution in ℓ).

3.4.2   Subsurface flows from the SDO/HMI ring-diagram pipeline

The SDO/HMI ring-diagram pipeline produces maps of horizontal flows in the depth range from the surface down to about 16 Mm with an average cadence of about 27 hr. Each ring tile covers a patch of about 180 Mm × 180 Mm on the solar surface and this is expected to set the horizontal resolution of the inferred flows (Birch et al. 2007). The flow maps produced by the pipeline oversample this resolution by a factor of two. The depth dependence of the flow in each tile is obtained by a one-dimensional inversion of the ring-fit parameters for that tile (Basu et al. 1999, Basu and Antia 1999). This approach of tile-by-tile one-dimensional depth inversions is very different than the three-dimensional (horizontal and vertical) inversion of many highly-overlapped tiles used by GHFT2015.

The pipeline ring-diagram data undergo a sequence of post-processing steps. Proxauf et al. (2020) describe these steps in detail. Here we give only a brief summary. The inverted ring-diagram flows from the pipeline are first multiplied by a scaling factor $r/R_\odot$. This is used to convert the surface-equivalent velocities $\Omega(r)R_\odot$ to linear velocities $\Omega(r)r$. We then subtract fits of sinusoids with a period of one year and of time-independent flows (differential rotation) at each Stonyhurst coordinate in order to reduce the systematic effects related to the orbit of SDO. Next, we interpolate the data onto a regular longitude grid, since the ring-diagram data originally have different longitude grids at different latitudes. Finally, we apply either of the approaches indicated in Sect. 3.4.1 to extract regions or to compute maps. We subsequently compute the SHT coefficients for the extracted data and obtain the m-summed power.

We then use the east-west velocities obtained in this method to compute E_ϕ using the HDS2012 method of constructing Carrington maps described above, except with a strip width of 15° instead of 13° and 27.2753-hr instead of 1-day time-averaging. We then compute E_ϕ averaged over the 25% of the Carrington rotations with the lowest activity.

3.4.3   Summary of the new results

Figure 3.2 shows the E_ϕ of surface flows obtained from granulation tracking as described in Sect. 3.4.1. The formal error estimates (estimated from the scatter between Carrington rotations) are not shown as they are small compared to the differences between different methods.

At low ℓ the spectrum of surface flows is larger than the upper limit of HDS2012 for subsurface flows, but the shape of the curve is similar, although with a slightly lower
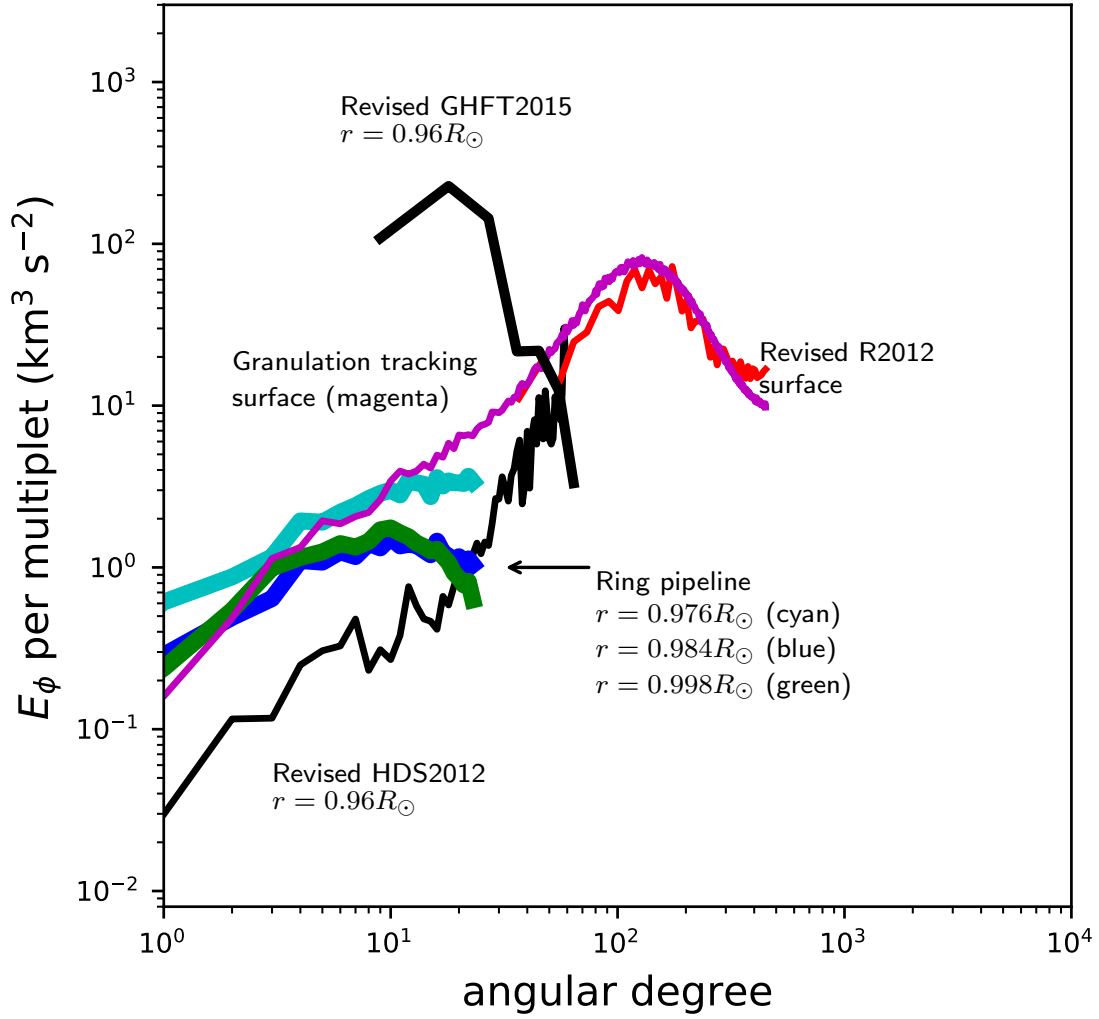
Figure 3.2: New measurements of $E_\phi(\ell)$ from granulation tracking (magenta) and from the SDO/HMI ring-diagram pipeline (1.1 Mm, green; 11.1 Mm, blue; 16.5 Mm depth, cyan) along with the revised estimates from Sect. 3.3 shown in Fig. 3.1.

slope. At the scale of supergranulation ($\ell \sim 120$), the spectrum of the surface flows measured here is similar to the spectrum from R2012.

Figure 3.2 also shows the average E_ϕ resulting from the SHT of the ring-pipeline Carrington maps (Sect. 3.4.2) for three different depths. The estimated errors (estimated from the scatter between Carrington rotations) are similar to the width of the line. The ring-diagram spectra E_ϕ extend up to $\ell = 23$, this is due to the spatial sampling of 7.5°. The tile size is 15°; the associated smoothing becomes more important with increasing ℓ. This may be the reason for the flattening and downturn of the curves above $\ell \approx 10$.
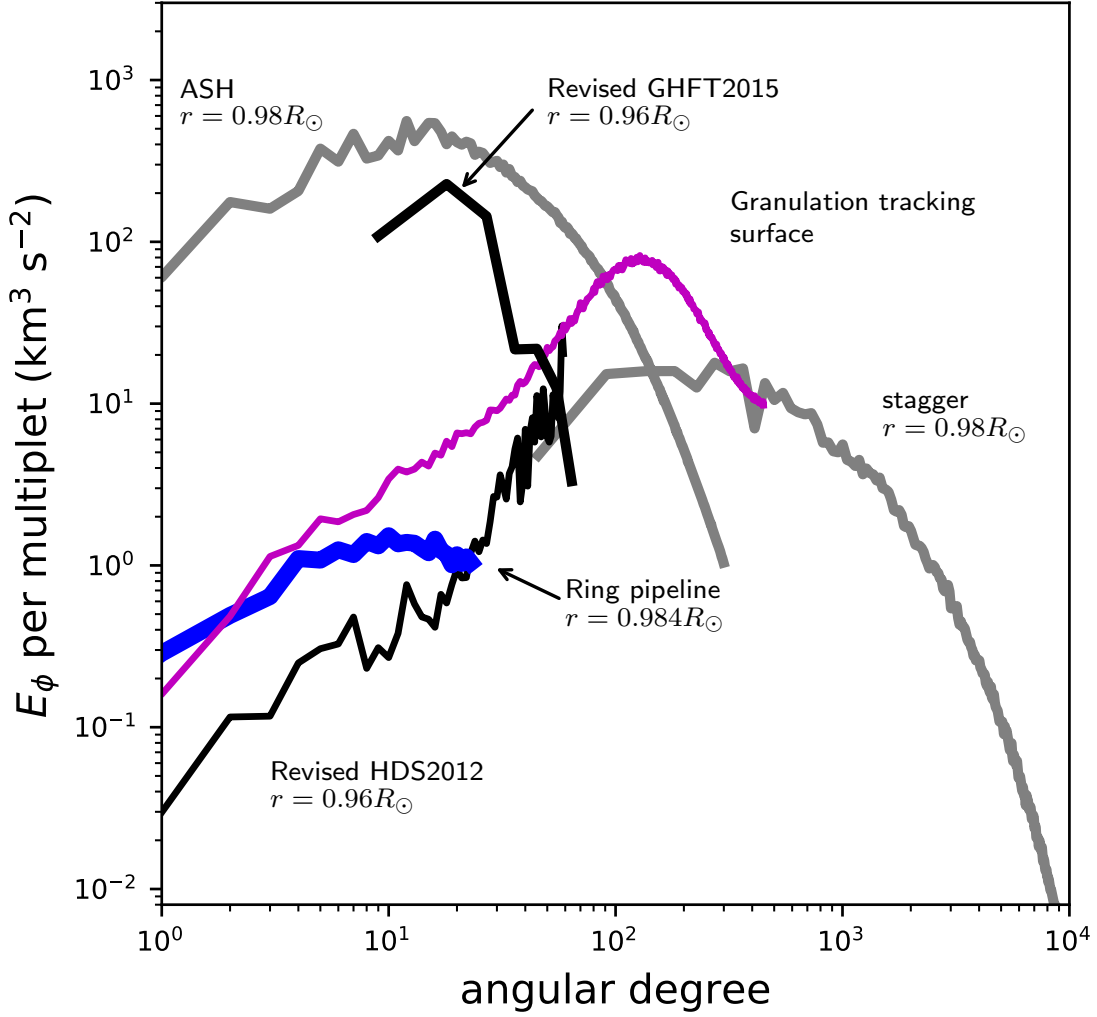
Figure 3.3: Summary of the estimates of E_ϕ. As in Fig. 3.2 the black curves show the revised estimates from HDS2012 and GHFT2015. The figure also shows the new granulation-tracking measurements (magenta) and new measurements from the ring-diagram pipeline (blue). The curves corresponding to the ASH and stagger simulations as described in GB2012 are shown in grey.

3.5 Conclusions and discussion

Figure 3.3 summarizes our current understanding of the spectrum of surface and subsurface east-west velocities from observations and simulations. We removed the curve for R2012 for the sake of simplicity; this curve is compatible (within a factor of two) with the new surface measurements.

The two ring-diagram estimates of E_ϕ shown in Fig. 3.3 are not compatible within the error estimates (see Fig. 5 from GHFT2015; the error estimate on the rms v_ϕ at $\ell = 10$ is less than 10%). Preliminary work (Nagashima et al. 2020) shows that the ring-fit parameter estimates from local power spectra by the ring-pipeline model `rdfitf` (Haber et al. 2000) and the multi-ridge fitting of GHFT2015 are not different enough to explain

the factor of roughly one hundred difference between the respective estimates of E_ϕ. We speculate the important difference between these two methods is the one-dimensional (depth only) tile-by-tile inversion employed by the pipeline and the three-dimensional (depth and horizontal directions) inversion used by GHFT2015. A comparison of the two approaches in a setting where the correct answer is known is needed to resolve this difference.

The new ring-diagram estimates shown here are roughly a factor of ten above the upper limit from HDS2012 at the lowest few angular degrees. We speculate that this may be due to the treatment of noise: the new ring-diagram estimates do not include any attempt to remove the contribution of noise to the measured E_ϕ; this is an important next step. In this sense, the ring-diagram measurements shown here are also upper limits.

The new ring-diagram estimates and the HDS2012 upper limits are both well below the spectrum of convection predicted by the simulations.

3.6 Appendix

3.6.1 SHT conventions

Here we use complex-valued spherical harmonic functions Y_ℓ^m that satisfy

$$\int_0^{2\pi}\int_0^\pi Y_\ell^{m*}(\theta,\phi)Y_{\ell'}^{m'}(\theta,\phi)\sin\theta\,\mathrm{d}\theta\,\mathrm{d}\phi = \delta_{\ell,\ell'}\delta_{m,m'}\,, \tag{3.3}$$

where θ is co-latitude and ϕ is longitude. The spherical harmonic transform of a function $f(\theta,\phi)$ is defined by:

$$f_{\ell,m} = \int_0^{2\pi}\int_0^\pi Y_\ell^{m*}(\theta,\phi)f(\theta,\phi)\sin\theta\,\mathrm{d}\theta\,\mathrm{d}\phi\,. \tag{3.4}$$

In this paper, we will only consider functions f that are real-valued. In this case, $f_{\ell,-m} = f_{\ell,m}^*$ and it is only necessary to compute the transform for $m \geq 0$. The inverse spherical harmonic transform is

$$f(\theta,\phi) = \sum_{\ell=0}^{\infty}\sum_{m=-\ell}^{\ell} f_{\ell,m}Y_{\ell,m}(\theta,\phi)\,. \tag{3.5}$$

The mean square value of a real-valued function f over a sphere is related to the spherical harmonic coefficients $f_{\ell,m}$ by

$$\langle f^2\rangle = \frac{1}{4\pi}\int_0^{2\pi}\int_0^\pi f^2(\theta,\phi)\sin\theta\,\mathrm{d}\theta\,\mathrm{d}\phi = \frac{1}{4\pi}\sum_{\ell=0}^{\infty}\sum_{m=-\ell}^{\ell}|f_{\ell,m}|^2\,. \tag{3.6}$$

In practical applications, the sum over ℓ is truncated at some sufficiently large value of ℓ. It is useful to define the power per multiplet:

$$P_\ell = \sum_{m=-\ell}^{\ell} |f_{\ell,m}|^2 = \sum_{m=0}^{\ell} w_m |f_{\ell,m}|^2 \, , \tag{3.7}$$

where the weights $w_m = 2 - \delta_{m,0}$ include the contributions from $m < 0$ and avoid double counting the contribution $m = 0$. This definition implies that

$$\langle f^2 \rangle = \frac{1}{4\pi} \sum_\ell P_\ell \, . \tag{3.8}$$

The limits on the summation over ℓ are not written for the sake of simplicity. Summation over ℓ is taken over the full range.

3.6.1.1 Connecting with GB2012

To connect with the notation of GB2012

$$\sum_\ell E_\phi(\ell) = \frac{r}{2} \langle v_\phi^2 \rangle = \frac{r}{8\pi} \sum_\ell P_\ell \, , \tag{3.9}$$

where r is the radius at which the flow v_ϕ is measured. We can then identify $E_\phi(\ell)$ from GB2012 with $rP_\ell/8\pi$, where P_ℓ is the power per multiplet of the v_ϕ component of a flow field.

3.6.1.2 Connecting with HDS2012

We denote the spherical harmonic transform of HDS2012 with a tilde to distinguish this transform from the SHT employed elsewhere in this work. This transform is related to the previously defined transform by

$$\tilde{f}_{\ell,m} = \frac{1}{\sqrt{2\pi}} f_{\ell,m} \, . \tag{3.10}$$

The power per mode is

$$\tilde{P}_{\ell,m} = |\tilde{f}_{\ell,m}|^2 = \frac{1}{2\pi} |f_{\ell,m}|^2 \, . \tag{3.11}$$

The average value of the square of f over the sphere is

$$\langle f^2 \rangle = \frac{1}{2} \sum_\ell \sum_{m=0}^{\ell} w_m \tilde{P}_{\ell,m} \, , \tag{3.12}$$

where the w are defined above (Eq. 3.7). For modes with $m > 0$, $w_m = 2$ and $\tilde{P}_{\ell,m}$ is the contribution of the mode (ℓ, m) to $\langle f^2 \rangle$. If we use δf to denote f after removing the longitude average of f (this corresponds to removing the contribution of the $m = 0$ modes) then we have

$$\langle [\delta f]^2 \rangle = \sum_\ell \sum_{m=1}^{\ell} \tilde{P}_{\ell,m} \, . \tag{3.13}$$

74

3.6.2 Fourier conventions

In order to connect the rms flows in spherical geometry with the Cartesian-domain simulations, it is important to define the power in a way that allows direct comparisons. We use here the Fourier convention

$$f(\mathbf{k}) = \sum_{\mathbf{x}} f(\mathbf{x}) e^{-i\mathbf{k}\cdot\mathbf{x}} , \qquad (3.14)$$

where $\mathbf{k}$ is a two-dimensional horizontal wavevector. The position vector $\mathbf{x}$ takes the values $(n,m)h_x$, where $h_x = h_y$ is the uniform grid spacing and (n,m) is a pair of integers, each in the range $-N/2$ to $N/2 - 1$, where the even integer N is the number of grid points. The wavevector, similarly, takes the values $(n,m)h_k$, where $h_k = 2\pi/(Nh_x) = 2\pi/(Nh_y)$ is the grid spacing in both k_x and k_y. The inverse transform is

$$f(\mathbf{x}) = \frac{1}{N^2} \sum_{\mathbf{k}} f(\mathbf{k}) e^{i\mathbf{k}\cdot\mathbf{x}} . \qquad (3.15)$$

We distinguish the function $f(\mathbf{x})$ and its Fourier transform $f(\mathbf{k})$ only by the argument. For a real-valued function $f(\mathbf{x})$ the horizontal average of $f^2(\mathbf{x})$ is

$$\langle f^2 \rangle = \frac{1}{N^2} \sum_{\mathbf{x}} f^2(\mathbf{x}) = \frac{1}{N^4} \sum_{\mathbf{k}} |f(\mathbf{k})|^2 . \qquad (3.16)$$

The Cartesian equivalent of Eq. 3.8 is

$$\langle f^2 \rangle = \sum_{k} P^{\text{fft}}(k) , \qquad (3.17)$$

where $P^{\text{fft}}(k)$ is the sum of $|f(\mathbf{k})|^2/N^4$ for all grid points with $k - h_k/2 \leq \|\mathbf{k}\| < k + h_k/2$. The sum runs over non-negative integer values of k/h_k. We would like to define power per multiplet $P(\ell)$ such that

$$\langle f^2 \rangle = \sum_{k} P^{\text{fft}}(k) = \sum_{\ell} P(\ell) . \qquad (3.18)$$

The contribution to $\langle f^2 \rangle$ per angular degree (i.e., for k in an interval of length $1/r$) is $P^{\text{fft}}(k)/(rh_k)$. This implies that

$$P(\ell) = \frac{1}{rh_k} P^{\text{fft}}(\ell/r) , \qquad (3.19)$$

where interpolation between values of k is implied in the evaluation of $P^{\text{fft}}(\ell/r)$.

To connect with the notation of GB2012

$$\sum_{\ell} E_\phi(\ell) = \frac{r}{2}\langle f^2 \rangle = \frac{1}{2h_k} \sum_{\ell} P^{\text{fft}}(\ell/r) , \qquad (3.20)$$

where r is the radius at which the flow field $f = v_\phi$ is measured. We can then identify $E_\phi(\ell)$ from GB2012 with $1/(2h_k)P^{\text{fft}}(\ell/r)$, where, as described above, P^{fft} is the angle-integrated power spectrum of the east-west component of the flow field.
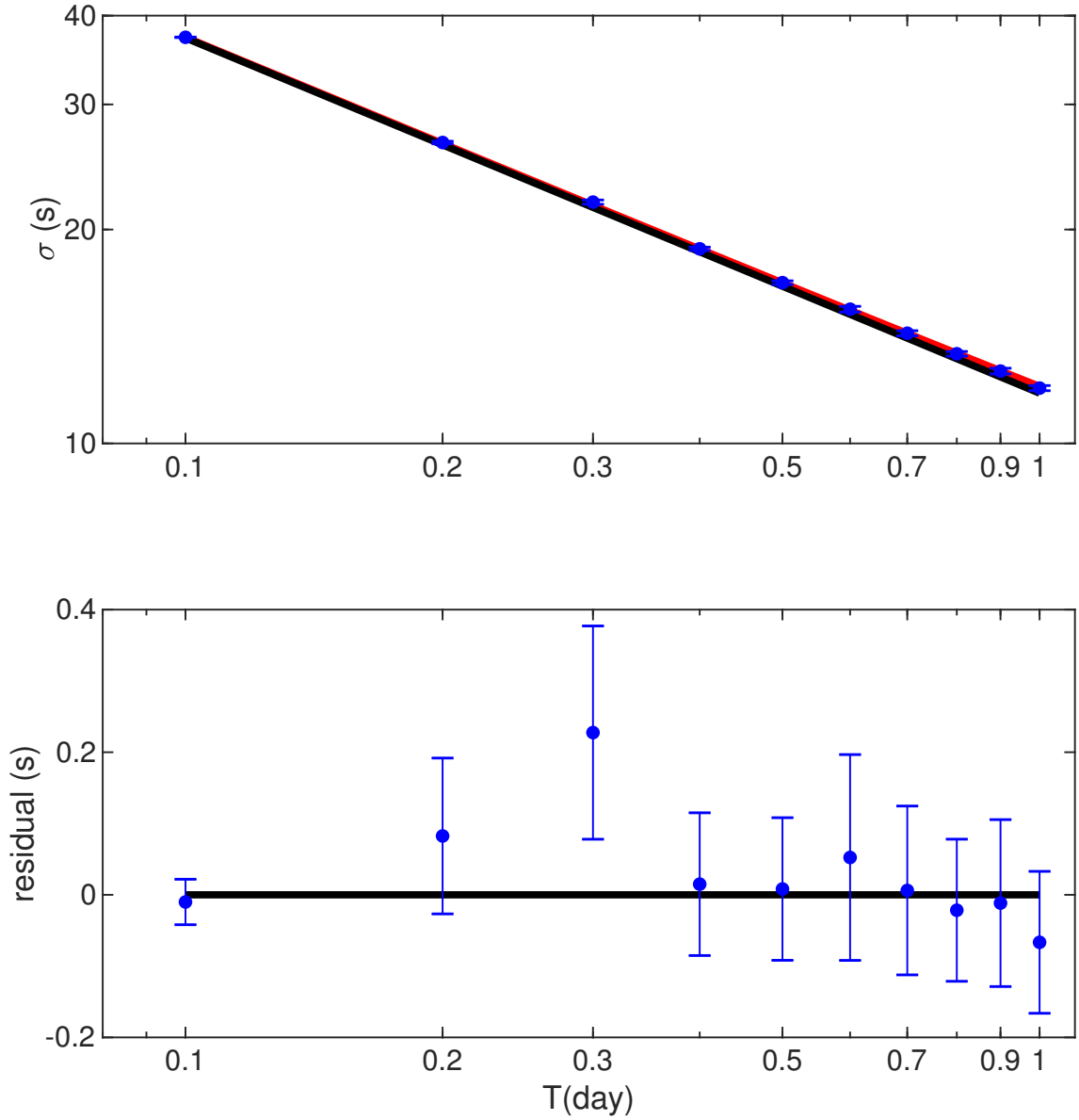
Figure 3.4: Standard deviation of travel-time maps (top panel) and residuals from the fit $\sigma^2 = S^2 + N^2/\left[T/(1\ \mathrm{day})\right]$ (bottom panel) as functions of the averaging time T. In the fit, the term S^2 is the contribution to the variance from a time-independent flow and N^2 is the contribution from realization noise at $T = 1$ day. In the top panel the noise contribution is shown in black and the model including the contribution from the signal is shown in red.

3.6.3 Reproducing the S/N fit from HDS2012

HDS2012 used time-distance helioseismology to compute maps of east-west travel-time differences for consecutive time intervals of 0.1 days. Let us denote these maps $\delta\tau_i(\theta, \phi)$. From these maps, travel-time maps corresponding to other time intervals were constructed by averaging these original maps. The variance $\sigma^2(T)$ of the resulting maps was then computed for $T = 0.1, 0.2, 0.3, 0.4, 0.5, 1$ days.

Figure 3.4 shows the variance in the travel-time maps as a function of the averaging
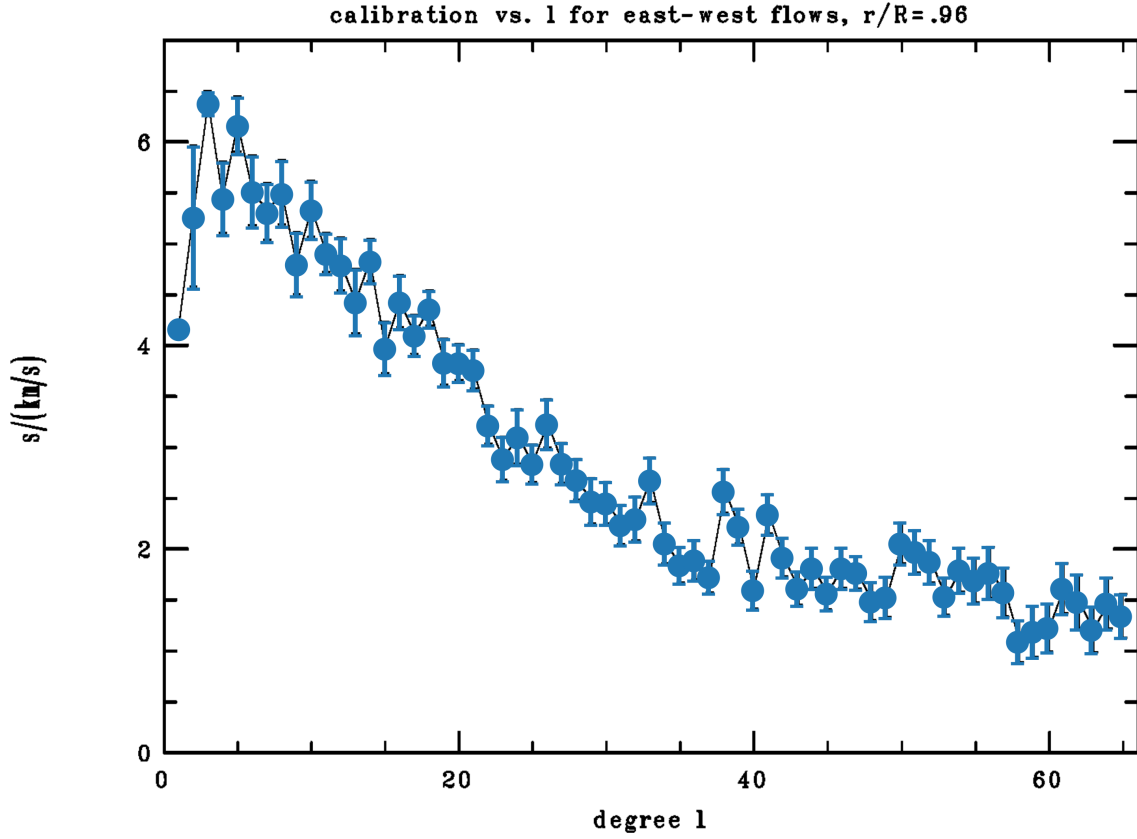
Figure 3.5: Calibration curve for converting time-distance travel times to flows. The gray-scale image in the background shows Fig. 2 from the Supplementary Material of HDS2012. The blue circles show the values used here.

time T. As expected for realization noise, the variance falls essentially as $1/T$. HDS2012 used the small deviation from a $1/T$ dependence to place an upper limit on the contribution of a time-independent signal to the variance. A least squares fit with the model $\sigma^2(T) = S^2 + N^2 / [T/(1 \text{ day})]$ yields $N = 11.77 \pm 0.02$ s and $S = 2.5 \pm 0.3$ s. This implies a noise-to-signal ratio of $N/S = 4.7 \pm 0.8$ at $T = 1$ day. This is in contrast with the value of 2 used in HDS2012.

3.6.4 Calibration of HDS2012 travel times

Figure 3.5 compares the original calibration curve with the calibration curve used in the current work. To obtain the values used here, we read values and error bars from the original figure from HDS2012.

4 Discussion and outlook

Here I extend the analysis of the previous chapters. I first briefly adress the horizontal Rossby wave eigenfunctions as seen on the Sun. Additionally, I generalize the Rossby wave study in the radial vorticity (Chap. 2) to other observables: I study power spectra of the prograde and northward velocities u_x and u_y, respectively, and of the horizontal divergence δ. Regarding the energy spectrum of horizontal flows (Chap. 3), I want to understand how these flows change in the presence of active regions. I thus study how the observed energy spectrum depends on solar activity. Finally, I outline possibilities for future research, both about solar Rossby waves and the energy spectrum of horizontal flows.

4.1 Horizontal Rossby wave eigenfunctions on the Sun

In order to obtain the horizontal eigenfunctions of solar Rossby waves, we can multiply the latitudinal eigenfunctions $C_m(\lambda)$ (Sect. 2.4.3), shown in Figs. 2.4 and 2.5, with the longitude dependence $e^{im\varphi}$ for each indiviual azimuthal order m. Here, however, I use eigenfunctions that were symmetrized in latitude.

Fig. 4.1 shows the resulting horizontal eigenfunctions from LCT at the surface for $m = 5, 9$ and 14. As can be seen, these eigenfunctions appear quite different from the sectoral spherical harmonics of early theoretical models (Fig. 1.5). The horizontal eigen-
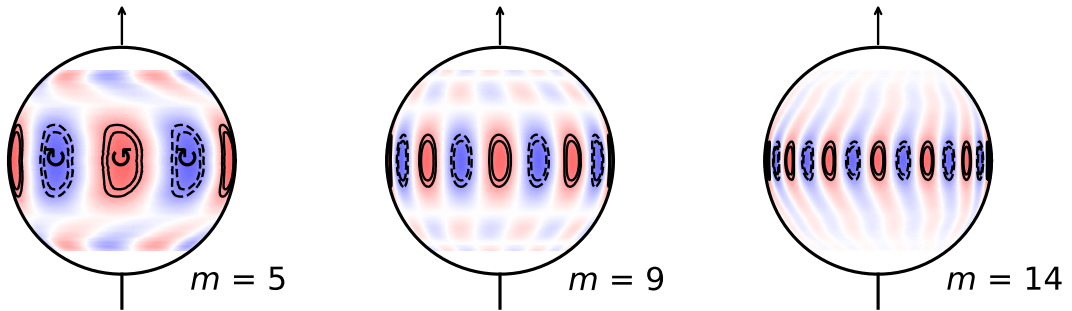
Figure 4.1: Horizontal eigenfunctions of solar Rossby waves for the azimuthal orders $m = 5, 9$ and 14 from LCT at the surface, as seen from the reference frame co-rotating at the equatorial rotation rate $\nu_{\rm eq} = \Omega_{\rm eq}/2\pi = 453.1$ nHz. The solid and dashed lines indicate contours of the horizontal eigenfunctions (at 0.65/0.80 and −0.65/−0.80, respectively). The counter-clockwise and clockwise arrows relate to the positive and negative radial vorticity of the horizontal eigenfunctions.

functions of solar Rossby waves are curved toward the retrograde direction for low m, they are nearly aligned in latitude and have a sign flip for intermediate m, and they are curved toward the prograde direction for high m. These different shapes are mainly due to the different sign of the imaginary part of the eigenfunctions for low and high m (see Fig. 2.5 and Sect. 2.4.3.3). The presence of an imaginary part and thus curved horizontal eigenfunctions is possibly related to the interaction of viscous Rossby waves and latitudinal differential rotation, as described in Gizon et al. (2020, submitted).

4.2   Rossby waves as observed in the horizontal velocities

I extend the HMI ring-diagram time series of u_x and u_y by roughly one and a half years to a total of more than nine years (May 19, 2010 to June 1, 2019). I process these flows as in Sect. 2.3.2 and compute the radial vorticity via Eq. 2.2. The horizontal divergence is

$$\delta(t, r, \lambda, \varphi) = \frac{1}{r \cos \lambda} \frac{\partial u_x(t, r, \lambda, \varphi)}{\partial \varphi} + \frac{1}{r \cos \lambda} \frac{\partial (u_y(t, r, \lambda, \varphi) \cos \lambda)}{\partial \lambda}. \qquad (4.1)$$

I then obtain power spectra for the horizontal velocities u_x and u_y (after the subtraction of the longitude average), the horizontal divergence δ, and the radial vorticity ζ (analogously to Chap. 2). The longer observation period implies a better frequency resolution.

Figure 4.2 shows the resulting power spectra for $\ell = m$ and $\ell = m + 1$, for RDA data near the surface. The $\ell = m$ power spectrum for ζ is very similar to Fig. 2.2. The $\ell = m$ power spectrum for u_y also contains Rossby waves (see Liang et al. (2019)). I do not observe $\ell = m = 2$ or $\ell = m = 1$ power near the frequencies predicted by the theoretical dispersion relation, neither in ζ nor in u_y, see Löptien et al. (2018) and Liang et al. (2019), respectively.

Rossby wave observations in u_x have not yet been discussed in the literature. The $\ell = m + 1$ power spectrum for u_x, however, shows a ridge, which coincides in frequency with the $\ell = m$ Rossby wave power for u_y and ζ. The north-south anti-symmetry around the equator in u_x is expected for sectoral Rossby waves, as is the north-south symmetry in u_y and ζ (Sect. 1.2.1). These symmetries are visible in schematic illustrations of the flow field, see Fig. 1.5, left panel.

I do not see north-south anti-symmetric Rossby waves in u_y or ζ (or north-south symmetric Rossby waves in u_x). This is consistent with Chap. 2 and the earlier observations by Löptien et al. (2018) and Liang et al. (2019). Löptien et al. (2018) hypothesize that non-sectoral Rossby waves dissipate on much shorter timescales than sectoral ones, which may be why those modes are not observed. I also do not observe Rossby waves in δ, similar to Löptien et al. (2018). This is consistent with the assumption of zero horizontal divergence used for the derivation of the theoretical Rossby wave dispersion relation (Sect. 1.2.1).

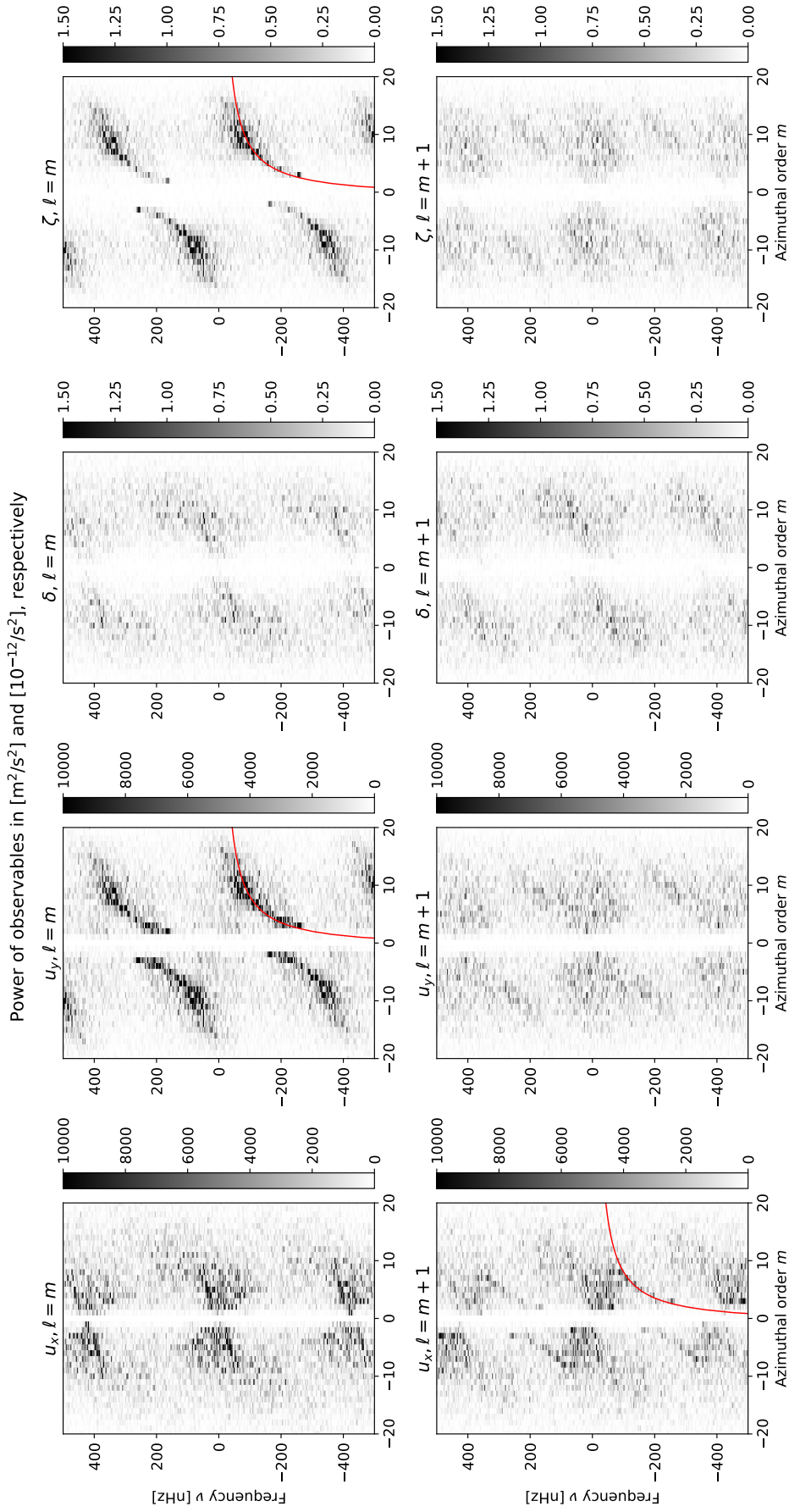Figure 4.2: Power spectra of the prograde velocity u_x, northward velocity u_y, horizontal divergence δ and radial vorticity ζ (columns) versus frequency ν and azimuthal order m, for $\ell = m$ (top row) and $\ell = m + 1$ (bottom row), from RDA at a depth of 0.7 Mm. The red line shows the textbook Rossby wave dispersion relation (Eq. 1.1) for the sectoral case ($\ell = m$).

4.3 Relation of energy spectra of horizontal flows to solar activity

4.3.1 Energy spectra of horizontal flows versus sunspot number

Here I use LCT u_x and u_y velocities that have been averaged over 24 hr in the Carrington reference frame, instead of the full time resolution of 30 min (for computational reasons). I compute the energy spectra $E_x(\ell)$[1] according to Eq. 3.9 for every time step and bin them in solar activity. For this I use the 13-month smoothed monthly total sunspot number (SSN) [2] from the World Data Center - Sunspot Index and Long-term Solar Observations (WDC-SILSO, Clette et al. 2014), and split the energy spectra into three equal-sized bins (terciles). I average $E_x(\ell)$ within the individual bins and also over all time steps at once.

The left panel of Fig. 4.3 shows that the energy spectrum for intermediate sunspot numbers is similar to that averaged over all time steps. At very large ℓ, the energy spectra do not depend strongly on the sunspot number. However, at small to intermediate ℓ ($4 \lesssim \ell \lesssim 60$, i.e spatial extents of $2\pi/\ell \sim 6\text{-}90°$), the energy increases with the sunspot number.

The energy ratio between high and low sunspot numbers is roughly 1.5 at $\ell \sim 5$ and decreases to unity around $\ell \sim 60$. The excess power could potentially be due to flows related to active regions (Sect. 1.2.3). The spatial scale of the largest excess, about $2\pi/\ell \sim 72°$, is much larger than flows up to 10 to 15° from the active region center (Löptien et al. 2017, Braun 2019). The size of groups of active regions might, however, affect the power spectrum of horizontal flows on spatial scales larger than this extent.

Around the supergranulation scale ($\ell \sim 120$), the power decreases with solar activity, with an energy ratio between high and low sunspot numbers of roughly 97 %. Given that the power should be proportional to the area, this might be caused by a smaller area on the solar surface covered by supergranules for high solar activity (due to suppression of convection by strong magnetic fields within active regions). Assuming suppressed supergranulation inside the active regions (Fig. 4.4, within the red contours), the fractional disk area covered by supergranules is (on average) ~ 97 %. This is in good agreement with the observed decrease of power.

4.3.2 Effect of active regions on energy spectra of horizontal flows

To check if flows around active regions indeed cause the observed excess power at high solar activity, I mask these flows. For this, I use HMI LOS magnetograms, tracked and averaged in time like the LCT velocity maps.

I apply a masking algorithm for active regions by P.-L. Poulier. For every time step it creates pixel masks for three different regions (Fig. 4.4). First, there are the active regions themselves, defined via thresholds for the line-of-sight component of the magnetic field B_{LOS} on the strength (≥ 20 G) and the flux ($\geq 10^{21}$ Mx). Second, there are rings around the active regions, which should contain the flows around the active regions. Third, there is the remaining solar disk, which should be the quiet Sun.

I distinguish between quiet-Sun maps (those without any active regions) and active

---

[1]In Chap. 3 the energy spectra of u_x and u_y flows are denoted as $E_\phi(\ell)$ and $E_\theta(\ell)$, respectively.
[2]http://sidc.be/silso/DATA/SN_ms_tot_V2.0.txt
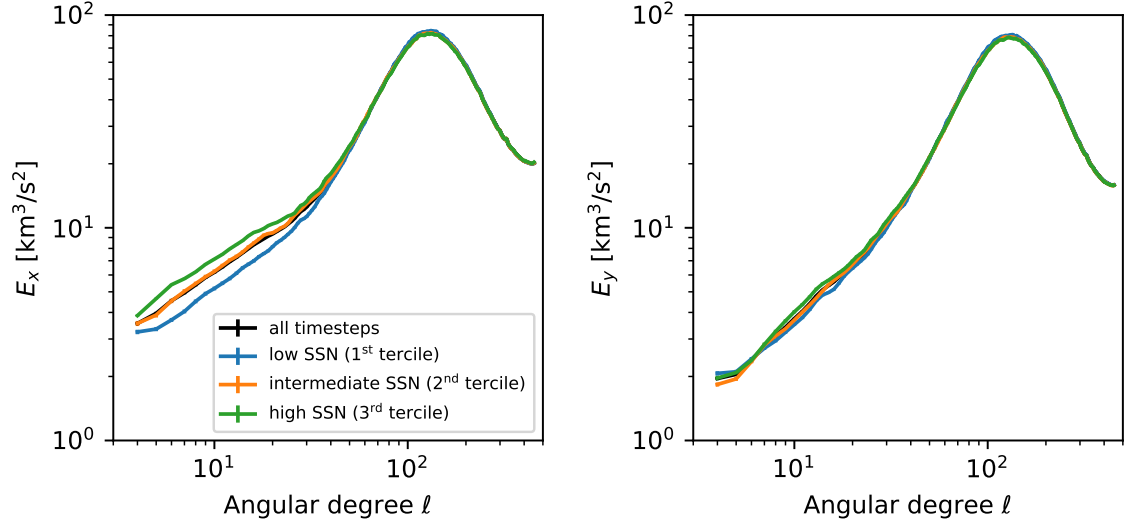
Figure 4.3: Left: Energy spectra $E_x(\ell)$ of u_x velocities from LCT for different levels of solar activity. The black, blue, orange and green curves indicate the energy spectra averaged over all time steps, the first, second and third tercile of the sunspot number, respectively (see text). Right: Analogous results for energy spectra $E_y(\ell)$ of u_y velocities from LCT. The error bars in both panels are comparable to the linewidths.
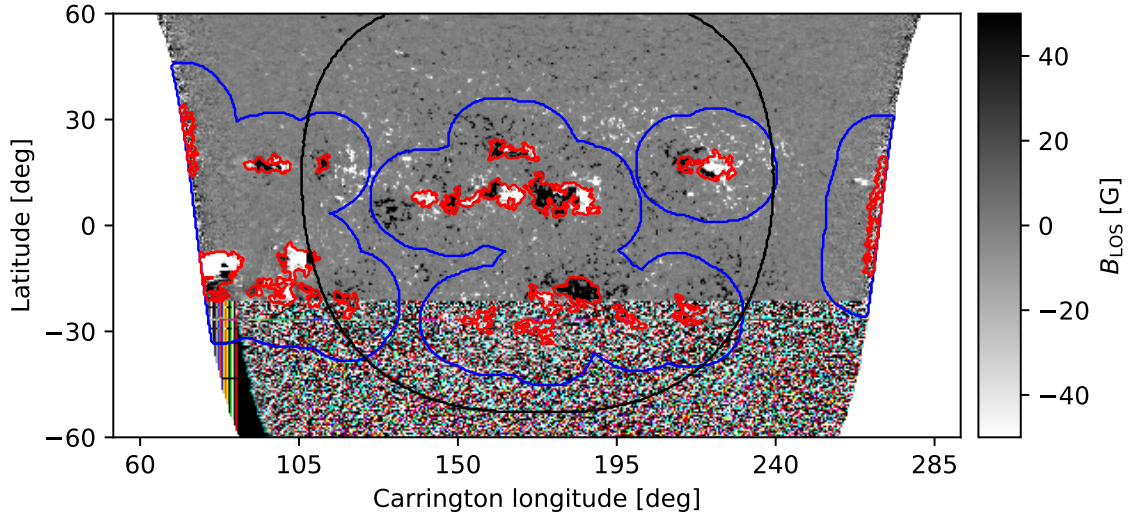
Figure 4.4: Active region masking example. The line-of-sight magnetic field B_{LOS} on September 24, 2012 is shown versus latitude and Carrington longitude. The contours indicate the border of the solar disk in the LCT velocity data for the same time step (black; it extends to 60° from disk center) and the outer borders of masked active regions (red) and their surroundings (blue).

region maps (with their pixel masks). Subsequently, I compute the energy spectra $E_x(\ell)$ according to Eq. 3.9 and average them, for both types of maps. The comparison of energy spectra for the active region maps to those for the quiet-Sun maps yields results that are qualitatively consistent with the previous sunspot number analysis: I observe a similar excess power at small to intermediate ℓ and a decrease of power at the supergranulation scale.

To study the origin of the excess power at intermediate spatial scales, I use quiet-Sun maps, where I replace pixels with those from active region maps, either within the interior or the surroundings of active regions (Fig. 4.4). I find that the increased power is mainly generated inside the active regions: Energy spectra for quiet-Sun maps with the interior of active regions replaced, are, between $\ell \sim 4$ and 20, roughly 1.1 to 1.3 times larger than those for quiet-Sun maps with the surroundings of active regions replaced. Flows around active regions thus do not have a large effect on the energy spectrum of horizontal flows. Instead, flows inside active regions, such as the moat flow around sunspots, could be responsible for the excess power.

I also repeat the above analysis for the northward velocity u_y. The right panel of Fig. 4.3 shows the energy spectra $E_y(\ell)$ for the binning in sunspot number. The energy spectra of u_y depend much less on solar activity than those of u_x. I note, however, that LCT velocity measurements at locations of high magnetic field strengths (beyond 500 G) are unreliable (Löptien et al. 2017).

4.4 Outlook

4.4.1 Rossby waves

Despite the new results presented in this thesis, both for solar Rossby waves and the energy spectrum of horizontal flows, many questions are still open. For example, the uncertainties on the depth dependence of Rossby waves from ring-diagram analysis are too large to constrain theories. Further research could be done with both theory (using models) and observations (using datasets that reach larger depths). For the latitude dependence of Rossby waves, improved modeling is needed to understand the observations. Theoretical research about Rossby waves is ongoing, but needs to take differential rotation, damping, and potentially the magnetic field into account. The dependence of the mode frequency on the differential rotation and the magnetic field is another topic for further Rossby wave studies. The excitation and damping of Rossby waves by convection should also be studied.

4.4.2 Convection

The discrepancy between energy spectra of horizontal flows from simulations/multi-ridge-fitting ring-diagrams and time-distance helioseismology remains mostly unaffected by the new, consistent results that I obtained from LCT and RDA. Synthetic data could help to resolve the disagreement between the observational results, via a comparison of the expected energy spectra to those obtained with different observational methods. A better understanding of solar convection on large scales may help to study the origin of the con-

vective conundrum. Apart from the prograde and northward velocities, energy spectra of the horizontal divergence and the radial vorticity could be studied. A similar analysis has been done by Hathaway et al. (2015).

Regarding supergranulation, it is still unclear why it appears as a distinct scale in the energy spectrum of horizontal flows. Current models attribute the origin of the supergranulation scale to supergranulation being the largest scale of convection that is either driven by buoyancy (Cossette and Rast 2016) or that is not strongly influenced by the solar rotation (Featherstone and Hindman 2016).

Bibliography

Aerts, C., Christensen-Dalsgaard, J., and Kurtz, D. W.: 2010, *Asteroseismology*, Springer Science+Business Media B.V.

Alshehhi, R., Hanson, C. S., Gizon, L., and Hanasoge, S.: 2019, *A&A* **622**, A124

Anderson, E. R., Duvall, Thomas L., J., and Jefferies, S. M.: 1990, *ApJ* **364**, 699

Backus, G. and Gilbert, F.: 1968, *Geophysical Journal* **16(2)**, 169

Baldner, C. S. and Schou, J.: 2012, *ApJ* **760(1)**, L1

Basu, S. and Antia, H. M.: 1999, *ApJ* **525(1)**, 517

Basu, S., Antia, H. M., and Tripathy, S. C.: 1999, *ApJ* **512(1)**, 458

Beck, J. G., Gizon, L., and Duvall, T. L., J.: 2002, *ApJ* **575(1)**, L47

Birch, A. C., Gizon, L., Hindman, B. W., and Haber, D. A.: 2007, *ApJ* **662(1)**, 730

Bogart, R. S., Baldner, C., Basu, S., Haber, D. A., and Rabello-Soares, M. C.: 2011a, in *GONG-SoHO 24: A New Era of Seismology of the Sun and Solar-Like Stars*, Vol. 271, p. 012008

Bogart, R. S., Baldner, C., Basu, S., Haber, D. A., and Rabello-Soares, M. C.: 2011b, in *GONG-SoHO 24: A New Era of Seismology of the Sun and Solar-Like Stars*, Vol. 271, p. 012009

Bogart, R. S., Baldner, C. S., and Basu, S.: 2015, *ApJ* **807(2)**, 125

Böhm-Vitense, E.: 1958, *ZAp* **46**, 108

Braun, D. C.: 2019, *ApJ* **873(1)**, 94

Brun, A. S., Miesch, M. S., and Toomre, J.: 2004, *ApJ* **614(2)**, 1073

Cameron, R. H. and Schüssler, M.: 2012, *A&A* **548**, A57

Charbonneau, P.: 2010, *Living Reviews in Solar Physics* **7(1)**, 3

Chelton, D. B. and Schlax, M. G.: 1996, *Science* **272(5259)**, 234

Cheung, M. C. M. and Isobe, H.: 2014, *Living Reviews in Solar Physics* **11(1)**, 3

Cheung, M. C. M., Rempel, M., Title, A. M., and Schüssler, M.: 2010, *ApJ* **720(1)**, 233

Christensen-Dalsgaard, J.: 2008, *Ap&SS* **316(1-4)**, 113

Christensen-Dalsgaard, J.: 2011, *ADIPLS: Aarhus Adiabatic Oscillation Package (ADI-PACK)*

Christensen-Dalsgaard, J., Dappen, W., Ajukov, S. V., Anderson, E. R., Antia, H. M., Basu, S., Baturin, V. A., Berthomieu, G., Chaboyer, B., Chitre, S. M., Cox, A. N., Demarque, P., Donatowicz, J., Dziembowski, W. A., Gabriel, M., Gough, D. O., Guenther, D. B., Guzik, J. A., Harvey, J. W., Hill, F., Houdek, G., Iglesias, C. A., Kosovichev, A. G., Leibacher, J. W., Morel, P., Proffitt, C. R., Provost, J., Reiter, J., Rhodes, E. J., J., Rogers, F. J., Roxburgh, I. W., Thompson, M. J., and Ulrich, R. K.: 1996, *Science* **272(5266)**, 1286

Christensen-Dalsgaard, J., Gough, D. O., and Thompson, M. J.: 1991, *ApJ* **378**, 413

Clette, F., Svalgaard, L., Vaquero, J. M., and Cliver, E. W.: 2014, *Space Sci. Rev.* **186(1-4)**, 35

Clune, T. L., Elliott, J. R., Miesch, M. S., Toomre, J., and Glatzmaier, G. A.: 1999, *Parallel Computing* **25**, 361

Cossette, J.-F. and Rast, M. P.: 2016, *ApJ* **829(1)**, L17

De Rosa, M. L. and Schrijver, C. J.: 2006, in *Proceedings of SOHO 18/GONG 2006/HELAS I, Beyond the spherical Sun*, Vol. 624 of *ESA Special Publication*, p. 12

Duvall, T. L., J., Jefferies, S. M., Harvey, J. W., and Pomerantz, M. A.: 1993, *Nature* **362(6419)**, 430

Featherstone, N. A. and Hindman, B. W.: 2016, *ApJ* **830(1)**, L15

Fisher, G. H. and Welsch, B. T.: 2008, in R. Howe, R. W. Komm, K. S. Balasubramaniam, and G. J. D. Petrie (eds.), *Subsurface and Atmospheric Influences on Solar Activity*, Vol. 383 of *Astronomical Society of the Pacific Conference Series*, p. 373

Gilman, P. A.: 1969, *Sol. Phys.* **8(2)**, 316

Gizon, L. and Birch, A. C.: 2005, *Living Reviews in Solar Physics* **2(1)**, 6

Gizon, L. and Birch, A. C.: 2012, *Proceedings of the National Academy of Science* **109(30)**, 11896

Gizon, L., Birch, A. C., and Spruit, H. C.: 2010, *ARA&A* **48**, 289

Gizon, L., Duvall, T. L., J., and Larsen, R. M.: 2001, in P. Brekke, B. Fleck, and J. B. Gurman (eds.), *Recent Insights into the Physics of the Sun and Heliosphere: Highlights from SOHO and Other Space Missions*, Vol. 203 of *IAU Symposium*, p. 189

Gizon, L., Duvall, T. L., and Schou, J.: 2003, *Nature* **421(6918)**, 43

Gizon, L., Fournier, D., and Albekioni, M.: 2020, *A&A* **642**, A178

Greer, B. J., Hindman, B. W., Featherstone, N. A., and Toomre, J.: 2015, *ApJ* **803(2)**, L17

Greer, B. J., Hindman, B. W., and Toomre, J.: 2014, *Sol. Phys.* **289(8)**, 2823

Haber, D. A., Hindman, B. W., Toomre, J., Bogart, R. S., Thompson, M. J., and Hill, F.: 2000, *Sol. Phys.* **192**, 335

Haber, D. A., Hindman, B. W., Toomre, J., and Thompson, M. J.: 2004, *Sol. Phys.* **220(2)**, 371

Hale, G. E.: 1908, *ApJ* **28**, 315

Hale, G. E., Ellerman, F., Nicholson, S. B., and Joy, A. H.: 1919, *ApJ* **49**, 153

Hanasoge, S., Gizon, L., and Sreenivasan, K. R.: 2016, *Annual Review of Fluid Mechanics* **48(1)**, 191

Hanasoge, S. and Mandal, K.: 2019, *ApJ* **871(2)**, L32

Hanasoge, S. M., Duvall, Thomas L., J., and DeRosa, M. L.: 2010, *ApJ* **712(1)**, L98

Hanasoge, S. M., Duvall, T. L., and Sreenivasan, K. R.: 2012, *Proceedings of the National Academy of Science* **109(30)**, 11928

Hanasoge, S. M., Woodard, M., Antia, H. M., Gizon, L., and Sreenivasan, K. R.: 2017, *MNRAS* **470(2)**, 1404

Hanson, C. S., Gizon, L., and Liang, Z.-C.: 2020, *A&A* **635**, A109

Hart, A. B.: 1954, *MNRAS* **114**, 17

Hathaway, D. H.: 1996, *ApJ* **460**, 1027

Hathaway, D. H.: 2015, *Living Reviews in Solar Physics* **12(1)**, 4

Hathaway, D. H., Beck, J. G., Bogart, R. S., Bachmann, K. T., Khatri, G., Petitto, J. M., Han, S., and Raymond, J.: 2000, *Sol. Phys.* **193**, 299

Hathaway, D. H., Teil, T., Norton, A. A., and Kitiashvili, I.: 2015, *ApJ* **811(2)**, 105

Hathaway, D. H., Upton, L., and Colegrove, O.: 2013, *Science* **342(6163)**, 1217

Herschel, W.: 1801, *Philosophical Transactions of the Royal Society of London Series I* **91**, 265

Hill, F.: 1988, *ApJ* **333**, 996

Hindman, B. W., Gizon, L., Duvall, Thomas L., J., Haber, D. A., and Toomre, J.: 2004, *ApJ* **613(2)**, 1253

Hindman, B. W., Haber, D. A., and Toomre, J.: 2009, *ApJ* **698(2)**, 1749

Holton, J. R.: 2004, *An Introduction to Dynamic Meteorology*, Vol. 88 of *International Geophysics*, Elsevier Academic Press

Howard, R. and Labonte, B. J.: 1980, *ApJ* **239**, L33

Howe, R.: 2009, *Living Reviews in Solar Physics* **6(1)**, 1

Howe, R., Christensen-Dalsgaard, J., Hill, F., Komm, R. W., Larsen, R. M., Schou, J., Thompson, M. J., and Toomre, J.: 2000, *Science* **287(5462)**, 2456

Hunter, J. D.: 2007, *Computing in Science & Engineering* **9(3)**, 90

Jouve, L. and Brun, A. S.: 2007, *A&A* **474(1)**, 239

Komm, R., González Hernández, I., Howe, R., and Hill, F.: 2015, *Sol. Phys.* **290(4)**, 1081

Komm, R., Howe, R., and Hill, F.: 2018, *Sol. Phys.* **293(10)**, 145

Kosovichev, A. G.: 2012, *Sol. Phys.* **279(2)**, 323

Kuhn, J. R., Armstrong, J. D., Bush, R. I., and Scherrer, P.: 2000, *Nature* **405(6786)**, 544

Lachlan-Cope, T. and Connolley, W.: 2006, *Journal of Geophysical Research (Atmospheres)* **111(D23)**, D23101

Langfellner, J., Birch, A. C., and Gizon, L.: 2018, *A&A* **617**, A97

Larson, T. P. and Schou, J.: 2018, *Sol. Phys.* **293(2)**, 29

Lee, U. and Saio, H.: 1997, *ApJ* **491(2)**, 839

Leighton, R. B., Noyes, R. W., and Simon, G. W.: 1962, *ApJ* **135**, 474

Liang, Z.-C., Gizon, L., Birch, A. C., and Duvall, T. L.: 2019, *A&A* **626**, A3

Libbrecht, K. G.: 1992, *ApJ* **387**, 712

Lisle, J. P., Rast, M. P., and Toomre, J.: 2004, *ApJ* **608(2)**, 1167

Liu, J. and Schneider, T.: 2011, *Journal of Atmospheric Sciences* **68(11)**, 2742

Löptien, B., Birch, A. C., Duvall, T. L., Gizon, L., Proxauf, B., and Schou, J.: 2017, *A&A* **606**, A28

Löptien, B., Birch, A. C., Duvall, T. L., Gizon, L., and Schou, J.: 2016, *A&A* **590**, A130

Löptien, B., Gizon, L., Birch, A. C., Schou, J., Proxauf, B., Duvall, T. L., Bogart, R. S., and Christensen, U. R.: 2018, *Nature Astronomy* **2**, 568

Mandal, K. and Hanasoge, S.: 2020, *ApJ* **891(2)**, 125

Martin-Belda, D. and Cameron, R. H.: 2016, *A&A* **586**, A73

McIntosh, S. W., Cramer, W. J., Pichardo Marcano, M., and Leamon, R. J.: 2017, *Nature Astronomy* **1**, 0086

Miesch, M. S.: 2005, *Living Reviews in Solar Physics* **2(1)**, 1

Miesch, M. S., Brun, A. S., DeRosa, M. L., and Toomre, J.: 2008, *ApJ* **673(1)**, 557

Miesch, M. S., Featherstone, N. A., Rempel, M., and Trampedach, R.: 2012, *ApJ* **757(2)**, 128

Nagashima, K., Birch, A. C., Schou, J., Hindman, B. W., and Gizon, L.: 2020, *A&A* **633**, A109

Nordlund, Å., Stein, R. F., and Asplund, M.: 2009, *Living Reviews in Solar Physics* **6(1)**, 2

November, L. J. and Simon, G. W.: 1988, *ApJ* **333**, 427

Oba, T., Riethmüller, T. L., Solanki, S. K., Iida, Y., Quintero Noda, C., and Shimizu, T.: 2017, *ApJ* **849(1)**, 7

Oliphant, T. E.: 2006, *A guide to NumPy*, Vol. 1, Trelgol Publishing USA

Papaloizou, J. and Pringle, J. E.: 1978, *MNRAS* **182**, 423

Parker, E. N.: 1955, *ApJ* **121**, 491

Pesnell, W. D., Thompson, B. J., and Chamberlin, P. C.: 2012, *Sol. Phys.* **275(1-2)**, 3

Pijpers, F. P. and Thompson, M. J.: 1992, *A&A* **262(2)**, L33

Prandtl, L.: 1925, *Zeitschrift Angewandte Mathematik und Mechanik* **5(2)**, 136

Provost, J., Berthomieu, G., and Rocca, A.: 1981, *A&A* **94**, 126

Proxauf, B., Gizon, L., Löptien, B., Schou, J., Birch, A. C., and Bogart, R. S.: 2020, *A&A* **634**, A44

Rieutord, M., Roudier, T., Rincon, F., Malherbe, J. M., Meunier, N., Berger, T., and Frank, Z.: 2010, *A&A* **512**, A4

Rieutord, M., Roudier, T., Roques, S., and Ducottet, C.: 2007, *A&A* **471(2)**, 687

Rincon, F. and Rieutord, M.: 2018, *Living Reviews in Solar Physics* **15(1)**, 6

Rossby, C.-G.: 1939, *Journal of Marine Research* **2**, 38

Rossby, C.-G.: 1940, *Quart. J. Roy. Meteorol. Soc.* **66**, 68

Roudier, T., Rieutord, M., Malherbe, J. M., Renon, N., Berger, T., Frank, Z., Prat, V., Gizon, L., and Švanda, M.: 2012, *A&A* **540**, A88

Saio, H.: 1982, *ApJ* **256**, 717

Schaeffer, N.: 2013, *Geochemistry, Geophysics, Geosystems* **14(3)**, 751

Scherrer, P. H., Schou, J., Bush, R. I., Kosovichev, A. G., Bogart, R. S., Hoeksema, J. T., Liu, Y., Duvall, T. L., Zhao, J., Title, A. M., Schrijver, C. J., Tarbell, T. D., and Tomczyk, S.: 2012, *Sol. Phys.* **275(1-2)**, 207

Schou, J.: 2003, *ApJ* **596(2)**, L259

Schou, J., Scherrer, P. H., Bush, R. I., Wachter, R., Couvidat, S., Rabello-Soares, M. C., Bogart, R. S., Hoeksema, J. T., Liu, Y., Duvall, T. L., Akin, D. J., Allard, B. A., Miles, J. W., Rairden, R., Shine, R. A., Tarbell, T. D., Title, A. M., Wolfson, C. J., Elmore, D. F., Norton, A. A., and Tomczyk, S.: 2012, *Sol. Phys.* **275(1-2)**, 229

Schwabe, H.: 1844, *Astronomische Nachrichten* **21(15)**, 233

Simon, G. W. and Weiss, N. O.: 1968, *ZAp* **69**, 435

Smeyers, P., Craeynest, D., and Martens, L.: 1981, *Ap&SS* **78(2)**, 483

Snodgrass, H. B. and Dailey, S. B.: 1996, *Sol. Phys.* **163(1)**, 21

Stein, R. F. and Nordlund, Å.: 1998, *ApJ* **499(2)**, 914

Stein, R. F. and Nordlund, Å.: 2006, *ApJ* **642(2)**, 1246

Sturrock, P. A., Bush, R., Gough, D. O., and Scargle, J. D.: 2015, *ApJ* **804(1)**, 47

Thompson, M. J., Christensen-Dalsgaard, J., Miesch, M. S., and Toomre, J.: 2003, *ARA&A* **41**, 599

Townsend, R. H. D.: 2003, *MNRAS* **340(3)**, 1020

Tremblay, B., Roudier, T., Rieutord, M., and Vincent, A.: 2018, *Sol. Phys.* **293(4)**, 57

Vallis, G. K. and Maltrud, M. E.: 1993, *Journal of Physical Oceanography* **23(7)**, 1346

Ward, F.: 1965, *ApJ* **141**, 534

Welsch, B. T., Fisher, G. H., Abbett, W. P., and Regnier, S.: 2004, *ApJ* **610(2)**, 1148

Williams, P. E., Hathaway, D. H., and Cuntz, M.: 2007, *ApJ* **662(2)**, L135

Wolff, C. L. and Blizard, J. B.: 1986, *Sol. Phys.* **105(1)**, 1

Wolff, C. L. and Hickey, J. R.: 1987, *Science* **235(4796)**, 1631

Woodard, M. F.: 1989, *ApJ* **347**, 1176

Zhao, J., Nagashima, K., Bogart, R. S., Kosovichev, A. G., and Duvall, T. L., J.: 2012, *ApJ* **749(1)**, L5

Scientific contributions

Refereed publications

- B. Löptien, A. C. Birch, T. L. Duvall, L. Gizon, **B. Proxauf**, and J. Schou: *Measuring solar active region inflows with local correlation tracking of granulation*, Astronomy and Astrophysics, 606, A28 (2017)

- B. Löptien, L. Gizon, A. C. Birch, J. Schou, **B. Proxauf**, T. L. Duvall, R. S. Bogart, and U. R. Christensen: *Global-scale equatorial Rossby waves as an essential component of solar internal dynamics*, Nature Astronomy, 2, 568-573 (2018)

- **B. Proxauf**, L. Gizon, B. Löptien, J. Schou, A. C. Birch, and R. S. Bogart: *Exploring the latitude and depth dependence of solar Rossby waves using ring-diagram analysis*, Astronomy and Astrophysics, 634, A44 (2020)

Paper in preparation

- A. C. Birch, T. L. Duvall, L. Gizon, S. Hanasoge, B. W. Hindman, **B. Proxauf**, and K. R. Sreenivasan: *Revisiting helioseismic constraints on solar convection*

Conference contributions

- Rocks & Stars II, Göttingen, Germany, 13 – 16 September 2017
  Oral presentation: *Depth dependence of solar horizontal flows from SDO ring-diagram analysis*

- Annual Meeting of the German Astronomical Society, Göttingen, Germany, 18 – 22 September 2017
  Poster: *Solar near-surface flows from ring-diagram helioseismology*

- XXXth General Assembly of the International Astronomical Union, Vienna, Austria, 20 – 31 August 2018
  Poster: *On the depth dependence of solar equatorial Rossby waves*

- 2018 Solar Dynamics Observatory Workshop *Catalyzing Solar Connections*, Ghent, Belgium, 29 October – 2 November 2018
  Poster and e-poster: *On the depth dependence of solar equatorial Rossby waves*

- 2nd Max Planck Partner Group Workshop on Solar Physics, Mumbai, India, 17 – 21 March 2019
Oral presentation: *Exploring the latitude and depth dependence of solar Rossby waves*

- 234th Meeting of the American Astronomical Society, St. Louis, USA, 9 – 13 June 2019
Oral presentation: *On the latitude dependence of Rossby waves in the Sun*

Acknowledgements

First, I wish to thank Laurent Gizon, who firmly and patiently guided me through my doctorate, always encouraging me to think differently about particular questions and to increase my knowledge on various subjects. Furthermore I wish to express my sincere gratitude to Björn Löptien, whose kind and thorough supervision helped me whenever I had questions. Without their patience and tireless support, this thesis would not have been possible.

I am also deeply indebted to Aaron Birch, for his creativity in thinking about problems, his never-ending helpfulness, and particularly his contributions and support for Chap. 3. Jesper Schou is thanked for sharing his knowledge on a variety of subjects and countless interesting discussions. Rick Bogart's help and expertise on all matters related to ring-diagram analysis supported me during the initial phase of my studies and contributed to a significant part of the data analysis in this thesis.

I want to express my gratitude to Andreas Tilgner for being in my thesis advisory committee, evaluating and assuring the progress of my studies, and for being the second referee of this thesis. I also would like to thank Ulrich Christensen, Stefan Dreizler, Wolfram Kollatschny and Olga Shishkina for their membership in my thesis defense committee.

Many thanks go to Zhi-Chao Liang for an independent confirmation of the results in Chap. 2. My deep thankfulness is also directed at Nils Gottschling and Paul-Louis Poulier for numerous, detailed discussions about local correlation tracking and active regions, and at Yuto Bekki for several discussions about Rossby waves and large-scale convection. I deeply owe Vincent Böning and Chris Goddard for several new, interesting insights and their overall support on a variety of matters. I also greatly appreciate a number of chats and useful discussions I had with Cilia Damiani, Robert Cameron, Hannah Schunker, Tom Duvall, Christian Baumgartner, Dan Yang, Felix Mackebrandt, and Jan Langfellner. Ray Burston is thanked in his role as the administrator of the data record management system DRMS.

I also thank the International Max Planck Research School for Solar System Science for enabling me to pursue my doctoral studies in this wonderful program. My thankfulness goes in particular to Sonja Schuh as the program coordinator, whose door was always open for everything related to the smooth progression of my PhD studies.

At the end, I want to say thanks to my family and friends, without whom my PhD studies would not have been possible. Their help and interest in my studies was invaluable and boosted my motivation. Finally, my deepest gratitude is dedicated to my personal sun, Erika Avendaño-Guzmán, who was always there for me, even when the skies where cloudy in Göttingen. Her endless love and support, which could be seen without any telescope, brightened any dark days I had and made the sunny ones unforgettable.

Curriculum vitae

Personal data

Full name	Bastian Severin Niklas Proxauf
Date of Birth	13 May 1993
Place of Birth	Freistadt, Austria
Nationality	Austrian

Education

PhD student

Oct. 2016 – Apr. 2020	at the International Max Planck Research School for Solar System Science and the University of Göttingen
Thesis	*Observations of large-scale solar flows*
Advisors	Prof. Dr. Laurent Gizon, Dr. Björn Löptien, Prof. Dr. Andreas Tilgner

M.Sc. in Astrophysics

Oct. 2014 – Sep. 2016	AstroMundus – Erasmus Mundus Joint Master Program in Astrophysics at the University of Innsbruck, the University of Rome Tor Vergata, and the University of Göttingen
Thesis	*Homogeneous Metallicity Scale for Galactic Classical Cepheids*
Advisor	Prof. Dr. Giuseppe Bono (University of Rome Tor Vergata)

B.Sc. in Physics

Oct. 2010 – June 2013	at the University of Innsbruck
Thesis	*Upgrading diagnostic diagrams of forbidden line emission: The influence of modern atomic data*
Advisor	Prof. Dr. Stefan Kimeswenger